Topi Uusitalo

Single- and Dual-Frequency Laser Diodes based on Surface Gratings

Tampere 2018

Topi Uusitalo

Single- and Dual-Frequency Laser Diodes based on Surface Gratings

Thesis for the degree of Doctor of Science in Technology to be presented with due permission for public examination and criticism in Sähkötalo Building, Auditorium SA203, at Tampere University of Technology, on the 3rd of August 2018, at 12 noon.

Doctoral candidate: Topi Uusitalo, M.Sc.
                         Laboratory of Photonics / ORC
                         Faculty of Natural Sciences
                         Tampere University of Technology
                         Finland

Supervisor: Mihail Dumitrescu, Doc.
                         Laboratory of Photonics / ORC
                         Faculty of Natural Sciences
                         Tampere University of Technology
                         Finland

Instructors: Mircea Guina, Prof.
                         Laboratory of Photonics / ORC
                         Faculty of Natural Sciences
                         Tampere University of Technology
                         Finland

                         Jukka Viheriälä, Doc.
                         Laboratory of Photonics / ORC
                         Faculty of Natural Sciences
                         Tampere University of Technology
                         Finland

Pre-examiners: Trevor Hall, Prof.
                         School of Electrical Engineering & Computer Science
                         Faculty of Engineering
                         University of Ottawa
                         Canada

                         Jari Turunen, Prof.
                         Institute of Photonics
                         Department of Physics and Mathematics
                         University of Eastern Finland
                         Finland

Opponent: Martijn Heck, Prof.
                         Department of Engineering
                         Aarhus University
                         Denmark

ABSTRACT

The thesis covers the development of single and dual longitudinal mode distributed feedback (DFB) lasers with surface gratings. These gratings were studied since they enable regrowth-free fabrication and easy implementation of arbitrary longitudinal effective refractive index variations. Advanced transverse and longitudinal surface grating structures were modeled, simulated, and experimentally tested. Procedures for optimizing the laser structures across a wide range of parameter variations were developed. The main targets were narrow linewidth emission for optical pumping of Rubidium atomic clocks, increased direct amplitude modulation for optical communications, and photonic generation of widely tunable electrical signals in the millimeter wave band for the next generation of wireless communications.

Laterally-coupled ridge-waveguide (LC-RWG) surface gratings with alternating lateral protrusions were developed to circumvent the etching aspect ratio limitation that prevents the fabrication of low-order short-wavelength surface gratings. The single longitudinal mode DFB lasers with alternating LC-RWG gratings emitting around 780 nm demonstrated improved performances, particularly important for the space borne target applications.

The dual longitudinal mode emission was achieved by periodically placing phase shifts along the grating. The experiments showed that the direct amplitude modulation bandwidth is extended when the photon-photon resonance associated with dual-mode emission is properly placed with respect to the carrier-photon resonance and when both resonances are adequately damped. Difference frequency range controlled by structural variations and 40 GHz difference frequency tuning by bias were demonstrated, as well as high speed difference frequency modulation. Linearly apodized LC-RWG surface gratings enabled a lower threshold current, a higher output power, and a broader range of difference frequency tunability by bias. Also the apodization and the complex-coupling of the surface gratings enabled the use of higher facet reflectivities, leading to narrower intrinsic short time-scale linewidths. The achieved performance improvements indicate that the studied laser types are promising solutions for their target applications.

ii

PREFACE

I would like to express my sincere gratitude to my supervisor Doc. Mihail Dumitrescu, whose support and guidance have been invaluable for this thesis' work and for many other projects. I would also like to thank my colleague Dr. Heikki Virtanen for all the support, especially with device processing and with other tasks we have carrier out together: without his work ethic and attention to detail many of the results in this thesis would not have been published. Prof. Mircea Guina has been the driving force behind the whole ORC for a long time and I wish to extend my gratitude for giving me the chance to carry out the research presented in this work. Doc. Jukka Viheriälä has been invaluable in coordinating the laser diode processing workflow, M.Sc. Antti Aho in drawing the nanoimprint masters, and M.Sc. Maija Karjalainen in processing the devices: thank you all. I also wish to thank Dr. Sanna Ranta for growing the epitaxial structures used in this thesis. My thanks also go to Prof. Paolo Bardella for assistance in simulations of laser dynamics.

Additionally I wish to thank Dr. Antti Laakso for his assistance in the beginning of my career, and later, especially with various modeling problems. I would also like to thank all the colleagues I have had the pleasure of knowing and working together along the years, having shared ideas and coffee, and sometimes perhaps coming up with bright ideas. Without the extensive and professional support staff of ORC this thesis would not be complete: thank you all. With the bureaucratic and other matters Mrs. Anne Viherkoski has been invaluable to myself and most likely almost everybody having worked at ORC: thank you for your patience, understanding and never-ending positivity during the time I have had the honor of working at ORC. Special

thanks go to my student comrades who have made studying at Tampere University of Technology more memorable and enjoyable.

Last I want to thank my family for all the support and understanding along the rocky road of higher education over the years. And Essi, whose love, support and voice of reason remind me that there indeed is life even after laser diodes inevitably die.

Tampere 8.5.2018

Topi Uusitalo

CONTENTS

GLOSSARY

A_m	Fourier coefficient for m^{th} order grating
G	modal gain
I_{th}	threshold current
I	bias current
K	Petermann K factor
M	number of grating periods between phase shifts
N_p	photon density
P_0	power contained in the fundamental mode
P	number of phase shifts in the grating
S	stopband width fitting parameter
V	volume of gain material
$\Delta\nu_{\text{Bragg}}$	frequency separation between the Bragg resonances of two stopbands
$\Delta\nu_{\text{FWHM}}$	spectral linewidth full width at half maximum
$\Delta\nu_{\text{modes}}$	frequency separation between two grating modes
$\Delta\nu_{\text{sb}}$	node-to-node width of a stop band
$\Delta\nu$	difference frequency
Δn	refractive index contrast
Γ^+	under-the-ridge confinement factor
Γ^-	not-under-the-ridge confinement factor
Γ_g	optical confinement factor in the grating area
Γ	optical confinement factor in the gain material
Λ_1	grating protrusion width
Λ	grating period
Ω_+	region of gain material under the ridge
Ω_-	region of gain material not under the ridge
Ω	integration domain
α_{eff}	effective linewidth enhancement factor
α_{int}	optical internal losses
α_{m}	mirror losses

β_0	propagation constant of the fundamental quasi-TE mode
η_i	internal quantum efficiency
γ	grating fill factor
κL	coupling strength of a DFB or DBR grating
κ_r	real coupling coefficient between forward and backward traveling waves
κ	coupling coefficient between forward and backward traveling waves
λ	wavelength
ν_{Bragg}	Bragg frequency
ν	laser frequency
ω_r	relaxation resonance frequency
ψ	quasi-TE mode amplitude
ρ	modal loss
τ_p	photon lifetime inside laser cavity
θ	angle of lateral current spreading
c	speed of light in vacuum
dg/dN	differential gain
dn/dN	change in refractive index with carrier density
g^+	constant gain approximation
g^-	constant loss approximation
g_{th}	threshold gain
h	Planck constant
k_0	free space wave number
m	grating order
n_0	longitudinally averaged refractive index
n_1	refractive index in the etched part of a grating
n_2	refractive index in the unetched part of a grating
n_{sp}	spontaneous emission factor
n_g	group index
n_{eff}	effective refractive index

n refractive index

q elementary charge

5G 5th generation wireless communication systems

x

ACRONYMS

AM	amplitude modulation
AR	anti-reflection (coating)
CB	conduction band
CMT	coupled mode theory
COD	catastrophic optical (mirror) damage
CPR	carrier–photon resonance
CW	continuous wave
DBR	distributed Bragg reflector
DC	direct current
DFB	distributed feedback
DFL	dual frequency laser
ECL	external cavity laser
ESA	electrical spectrum analyzer
ET	etched through (ridge)
FCA	free carrier absorption
FD	finite differences
FEM	finite element method
FF	far-field
FM	frequency modulation
FP	Fabry–Pérot (resonator)
FSR	free spectral range
FWHM	full width at half maximum
FWM	four-wave mixing
hh	heavy hole
HR	high reflection (coating)
IR	infrared
LC	laterally coupled
LD	laser diode
lh	light hole
LIV	light-current-voltage
LO	local oscillator

MMW	millimeter wave
MOPA	master oscillator power amplifier
MZM	Mach-Zehnder modulator
NIL	nanoimprint lithography
OPO	optical parametric oscillator
PCE	power conversion efficiency
PD	photodiode
PIC	photonic integrated circuit
PLL	phase locked loop
PPR	photon–photon resonance
PPS-DFB	periodic phase-shifted distributed feedback
PSD	power spectral density
QAM	quadrature amplitude modulation
QPSK	quadrature phase shift keying
QW	quantum well
QWS	quarter wave shifted
Rb	Rubidium
RF	radio frequency
RoF	radio over fiber
RWG	ridge waveguide
SCH	separate confinement heterostructure
SEM	scanning electron microscope
SFL	single frequency laser
SG	sampled grating
SHB	spatial hole burning
SLM	single longitudinal mode
SMSR	side mode suppression ratio
STM	single transverse mode
TDTW	time domain travelling wave
TE	transverse electric
TM	transverse magnetic
TMM	transfer matrix method

UV	ultraviolet
VB	valence band
WDM	wavelength division multiplexing
WG	waveguide

LIST OF PUBLICATIONS

I Uusitalo, T., Virtanen, H., Karjalainen, M., Ranta, S., Viheriälä, J., Dumitrescu, M., Distributed Feedback Lasers with Alternating Laterally-Coupled Ridge-Waveguide Surface Gratings, Optics Letters, vol. 42, no. 16, pp. 3141–3144 2017.

II Uusitalo, T., Virtanen, H., Dumitrescu, M., Transverse Structure Optimization of Distributed Feedback and Distributed Bragg Reflector Lasers with Surface Gratings, Optical and Quantum Electronics, vol. 49, no. 6, pp. 206 Jun. 2017.

III Uusitalo, T., Virtanen, H., Bardella, P., Dumitrescu, M., Analysis of the Photon-Photon Resonance Influence on the Direct Modulation Bandwidth of Dual-Longitudinal-Mode Distributed Feedback Lasers, Optical and Quantum Electronics, vol. 49, no. 1, pp. 46 Jan. 2017.

IV Uusitalo, T., Virtanen, H., Viheriälä, J., Dumitrescu, M., Dual-Mode DFB Laser Diodes with Apodized Surface Gratings, accepted for publication in Optics Express, 2018.

AUTHOR'S CONTRIBUTION

The thesis includes three publications in peer-reviewed literature and one submitted article. The contributions of the authors are described below.

The thesis author is the first author of publication I, which was also included in the PhD thesis of Heikki Virtanen. The thesis author conducted the modeling, simulation, and design of the transverse structure of the laser and did most of the characterization, while the manuscript was written together with Heikki Virtanen. Maija Karjalainen carried out device processing, Sanna Ranta grew the epiwafers, Jukka Viheriälä coordinated the device processing, and Mihail Dumitrescu envisioned the alternating grating scheme, coordinated the simulation and design of the total laser structure and the writing process of the manuscript.

Publication II was a simulation study done by the thesis author and coordinated by Mihail Dumitrescu. Heikki Virtanen did a part of the analytic derivations presented in the publication.

The work in publication III is a combination of characterization and simulation results. The thesis author carried out most of the measurements and the simulations confirming the time domain behavior of the modulated laser, as well as developed the time domain signal analysis procedure. Heikki Virtanen processed the lasers for the modulation measurements. Paolo Bardella carried out the time domain simulations which presented the small signal modulation bandwidth extension and eye diagrams in the large signal modulation case and assisted in manuscript preparation. Mihail Dumitrescu coordinated the theoretical part of the publication and manuscript writing.

Publication IV contains analytic and simulation results done in cooperation by the thesis author and Mihail Dumitrescu, measurement results and their analysis done by the author, and longitudinal simulations done by Heikki Virtanen. The devices were processed by Heikki Virtanen and Jukka Viheriälä coordinated the effort. The manuscript was written mostly by the thesis author with support from all the co-authors.

1. INTRODUCTION

Since its first demonstration in the 1960's [1], light amplification by stimu-
lated emission of radiation, laser, has penetrated into most fields of science
and technology. The light from a laser has properties such as coherence,
polarization, and spectral purity, which can be controlled by designing the
laser appropriately [2]. The chosen design depends on the application needs:
in laser welding, for instance, high power levels can dominate in the design
requirements [3] whereas for spectroscopic applications the coherence prop-
erties are usually much more important than the total power [4], [5]. Another
factor in the laser design is the overall size. In many applications the size is
not limited, and very complex laser systems with building-size footprints are
employed *e.g.* to reach extreme power levels[1]. Highly stable lasers can also
have a considerable footprint, although their footprint could only be consid-
ered moderate [6]. Even the moderate footprints can be too much for some
applications, however: for instance in space and other hostile environments
the complexity of a laser system can be a detrimental factor, because even
though complex designs can be made robust enough [7], it can be beneficial
to decrease the weight and footprint of the laser as much as possible [8].
Another case where extremely small footprint and complexity are beneficial
is when the laser emitter density needs to be high. Nowadays the prime
example of this is the optical telecommunications industry, where individual
packaged laser sizes can be in the cubic centimeter ranges [9]. Chip-level op-
tical communications require even smaller footprints and power consumption
levels, which are important in keeping up with the demand for bandwidth
while keeping the power consumption under control [10].

One type of lasers especially suited for the requirements of simple construc-

---

[1]`https://lasers.llnl.gov/about/what-is-nif`

tion, robustness, and small size are laser diodes (LDs) [11]. They are compact, low cost, power efficient, employ user safe voltages, and have an increased presence in everyday infrastructure. The compactness of a LD is the result of monolithically integrating all the laser elements into a single semiconductor component. The small size and the fact that multiple laser chips are fabricated in parallel from a semiconductor wafer lead to a relatively low cost per a LD, especially if similar devices are mass-produced. When the required power levels from LDs are relatively low, it is possible to design the device without the need for active cooling. This can be advantageous for the overall energy efficiency of the packaged device, since active cooling can take a large portion of the overall power budget of a device [12]. The advantages and maturity of LDs are also beneficial when laser light is used in demanding applications such as space bound experiments, where robustness, reliability, small footprint and small weight are of high importance [13].
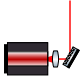
A particular type of LDs are single frequency lasers (SFLs), which are required in telecommunications and in scientific applications, such as spectroscopy, frequency referencing, and atomic clocks. There are several ways to achieve high spectral purity for the LD. External cavity lasers (ECLs) employ an external feedback element, which is used to control the spectral output of the LD. This design leads to good output powers and wavelength tunability, but, on the other hand, the design is not compact and robust, has moving parts, and is not as cost efficient as monolithic solutions [14].

A common way to achieve a SFL with a monolithic design is to use distributed feedback (DFB) structures with buried gratings, which are frequency selective elements embedded inside the LD, typically close to the active region of the laser [15]. In the fabrication of buried gratings, a part of the semiconductor epilayer structure is grown first, then it is patterned to produce the grating, and subsequently the top epilayers are overgrown over the grating structure. These types of LDs have shown high power efficiencies [16], but the intermediate processing of the grating structure and the overgrowth step complicate the fabrication, as compared with the case when the fabrication comprises a single epitaxial growth followed by device processing. The buried grating structures can also lead to defects in the grating area [17], placed relatively close to the laser active region, where the cur-

rent density, temperature and optical field can be high. Due to the usually applied conventional lithography methods the buried gratings are typically uniform. When longitudinally non-uniform multi-section structures are employed, it is extremely challenging to accurately align the LD top structure elements, such as distinct contacts, with specific parts of the buried structure after the over-growth. Buried gratings with multiple phase shifts have been realized in spite of these challenges [18].

Surface gratings circumvent the need for the regrowth step and they can easily be aligned with the contacts both laterally and longitudinally [19]. These aspects, combined with using nanoimprint lithography for defining the surface grating etch masks, lead to simplified fabrication and open the possibility to have arbitrary grating profiles or complex non-uniform or multi-segment LD structures or a combination of those. Moreover, in the case of surface gratings, the defect-prone processed interfaces are kept away from the main current flow path and away from regions with high optical field intensities and high temperature, which can reduce device degradation and increase the reliability. Table 1.1 gives a qualitative comparison between the main three types of single-frequency semiconductor LDs.

Table 1.1 *Qualitative comparison between the main types of single-frequency semi-conductor LDs.*

Type	Characteristic			
	Device complexity	Fabrication cost	Wavelength tunability	Output power
ECL	−	− −	++	++
Buried grating DFB	+	−	+	+
Surface grating DFB	++	++	+	+

In telecommunications high modulation speeds are used to leverage the huge available bandwidth of the optical fibers [20]. The laser light modulation format [21] is achieved either by directly modulating the laser emitters [22] or by using external modulation [23]. The modulation types place different requirements on the single mode purity of the LDs, but these requirements are typically not as strict as they can be in other applications, such as atomic clocks. Atomic clocks are based on the well defined frequency differences between atomic energy levels in certain elements, such as Rubidium (Rb) [24]. To exploit the accuracy of these frequency differences, the spectral purity of the lasers employed in atomic clocks should be very high [25], [26].

The emergence of 5G networking and the ever-increasing need for higher bandwidths are imposing high requirements on the electronic components of the radio frequency networks. Electrical generation of high frequency signals is typically based on multiplying a lower frequency [27] and when the needed number of these multiplication steps increases, the power requirements and the noise of the signal also increase [28]. Laser and photonic based solutions can provide a scalable way for high frequency radio signal generation [29]. It should be noted that in this thesis the terms (extremely/ultra) high frequency and millimeter wave (MMW), related to the difference frequency radio frequency (RF) signal generated by photodetection, are interchangable and typically mean frequencies between 10–100 GHz. In addition, the extremely high frequency carrier signals, which have high atmospheric attenuation [29], can be distributed with low losses over optical fibers when they are carried with the help of laser light [20]. The benefit of this is that the base stations of future wireless networks [30], which transmit the extremely high frequency signals to and from the end user, can have a simpler architecture, and thus a lower overall cost. Because the signal attenuation typically increases for higher frequencies, the benefit obtained from this simplification grows when higher frequency bands are used, because the density of the base stations increases [29]. The laser light can also be modulated, either directly or externally, in order to transmit data signals with or in addition to the high frequency carriers. Direct modulation of LDs make the signal encoding simpler, but it is dependent on how well the output of the LD can follow the modulating signal [31], which is usually limited by the carrier–photon resonance (CPR) in the lasers.

1.1   Approach and motivation

The work reported in the thesis concerns laterally coupled (LC)-ridge wave-guide (RWG) DFB and etched through (ridge) (ET)-RWG distributed Bragg reflector (DBR) surface gratings, their design [II] and use in LDs targeting applications in telecommunications [III], [IV], spectroscopy, and frequency standards [I]. DFB lasers with surface gratings [19] were studied because of their low complexity and simple fabrication when compared to ECL or buried grating DFB LDs, the two typical approaches in making frequency selective edge emitting LDs.

The narrow linewidth emission around 780 nm [32] was targeted by using long laser cavities with low grating strengths, whose efficiencies were improved by employing the alternating grating scheme [I].

The extension of the direct amplitude modulation response beyond the limit imposed by the CPR was studied by exploiting the photon–photon resonance (PPR) effect, resulting from the emission of two longitudinal laser modes from the same cavity in this case. The dual-longitudinal mode emission was achieved by using gratings with two (or more) phase shifts placed periodically along the LC-RWG surface gratings [III].

In addition to the modulation bandwidth extension, the emission of two longitudinal modes was used to generate extremely high frequency RF signals which could be used in the next generation wireless communication standards. The direct modulation of the difference frequency between the emitted modes was examined with frequency and time domain characterization methods [III]. Lasers with apodized LC-RWG surface gratings were also designed to have extended tuning ranges of the difference frequency, enabling the generation of RF signals for several next generation wireless communication frequency bands from the same laser [IV].

In summary the main targets of the thesis are:

- **exploit surface structures that enable cost effective and simplified fabrication of gratings with arbitrary configurations**

- **develop simulation procedures and define figures of merit that enable a fast and effective optimization over a broad range of variation for multiple structural parameters**

- **demonstrate SFLs at 780 nm with characteristics suitable for Rb atomic clocks**

- **demonstrate dual frequency lasers (DFLs) with increased amplitude modulation bandwidth and with the capability for extremely high frequency electrical signal generation**

1.2   Theoretical background

LDs are popular in many fields of science, technology, and industry, and are gaining increasing adoption. They are often used in applications such as telecommunications [33], atomic clocks [24], and spectroscopy [34], which require good stability and narrow emission linewidth. There are also other laser types that offer better stability [6] but, due to their miniature size and power consumption, the LDs are the preferred choice in most applications. This preference is emphasized further due to the increased use of laser sources in mobile applications and photonic integrated circuits (PICs) [10].

The simplest LD is a Fabry–Pérot (resonator) (FP) laser [31], whose output is mainly determined by the material gain, cavity length, and diode facet reflectivities: the mode losses are not affected by the longitudinal structure of the cavity if the facets and material is assumed dispersionless, see Figure 1.1, and the powers of the emitted modes is determined by the spectral shape of the gain. The output behavior can be modified by introducing different elements in or outside the cavity and by changing the cavity facet reflectivities. These elements include DBR [35] and DFB [36] gratings, active or passive waveguides [37], and bent and tapered waveguides [38], to name a few. By designing and combining these elements, the output characteristics of a LD can be engineered with great flexibility. For instance, the output power, beam divergence and brightness, linewidth, and modulation response can be affected by the design choices [39].

This thesis covers mainly DFB LDs, which modify the mirror losses of the
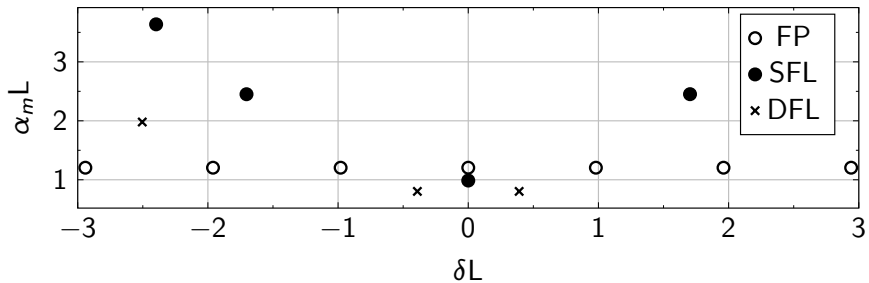
Figure 1.1 *Normalized mirror losses with normalized detuning factor for FP and single and dual frequency DFB Bragg gratings.*

typical FP LDs by changing the feedback between the longitudinal edges of the resonator. The number of dominant longitudinal modes in the output of the LDs can be thus chosen with the DFB structure, as illustrated in Figure 1.1. There are different implementation types of DFBs. Buried DFB gratings are very popular due to their ability to produce high power, injection efficiency, coupling coefficients, and good beam qualities. They have also been used with new types of grating structures, such as sampled, chirped and phase shifted DFB gratings [40], [41] and sampled grating (SG) DBRs [42], [43]. In spite of the good performance of buried gratings, they require a complicated regrowth step in the fabrication, which affects the yield and cost of each device [44], and can also cause degradation effects which reduce the device lifetime [17].

Using surface gratings is one way to overcome the need for regrowth, and the devices reported in this thesis use the technology exclusively. With this method the processing of a LD is done in a single step and no further epitaxial steps and overgrowth are needed. Schematic and scanning electron microscope (SEM) pictures of LC-RWG and ET-RWG surface grating are illustrated in Figure 1.2. The use of surface gratings also places the defects inherently induced by the processed interfaces away from the areas with high optical field intensity, high temperature and intense carrier flow, which can improve the reliability and yield. The fabrication of all devices studied in this thesis employed soft stamp ultraviolet (UV)-nanoimprint lithography (NIL) [19], which enables high resolution and volume-scalable fabrication

of surface patterns with arbitrary shapes and configurations. The soft and
flexible stamp facilitate the imprinting even for non-flat brittle epiwafers
or in the presence of residual particles on the surface or both, because the
stamp conforms to non-flat surfaces and locally to residual particles so that
the pattern is only compromised in the vicinity of the particle while the rest
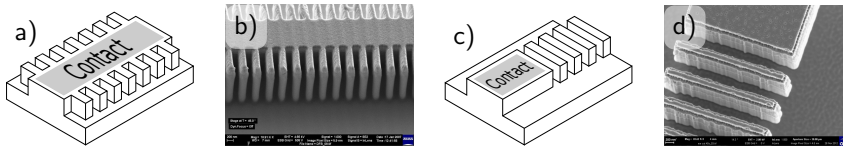of the patterned area is unaffected.

Figure 1.2 *Schematics and SEM pictures of LC-RWG (a–b) and ET-RWG (c–d) gratings. Adapted from [II].*

Surface gratings have been applied recently also by several other groups to
address different wavelength ranges and grating configurations [44]–[46]. The
downside to the LC-RWG surface gratings is the poor injection efficiency [47],
which is due to the fact that the electrical pumping leads to lateral current
leakage to the areas below the lateral protrusions of the gratings, which do
not contribute to the stimulated emission significantly. The current leak-
age can be restricted by ion implantation [48], recessed gratings [49], [50],
and oxidization, which has been used for injection current control in surface
emitting laser diodes [51], all of which unfortunately complicate the fabrica-
tion process. A way to overcome the lateral current leakage issue is to use
DBR-like schemes, where the grating region is not pumped and thus does
not decrease the injection efficiency. This kind of approach has been suc-
cessfully used to achieve good performances in amplified configurations [52].
Other, surface type feedback schemes are also possible, such as the slotted
ridge waveguide lasers [53].

Surface grating configurations frequently exhibit lower output powers than
the buried gratings, which is mainly due to the lower injection efficiency and
to the corresponding added thermal load. This has been addressed by us-
ing monolithically integrated amplifiers in master oscillator power amplifier
(MOPA) schemes. The amplifiers can be either straight [54] or tapered to
increase in the mode area, decrease the optical power density and diffraction

out of the laser [55] and increase the power saturation level [54].

The surface gratings bring many benefits to device fabrication, mainly related to the removal of regrowth from the fabrication process of the lasers. With small adjustments to the surface grating structures, their performances can approach and exceed those of buried grating structures. There is still a lot of room for improvement, however, especially in the efficiency of surface grating structures.

1.2.1 Single frequency laser diodes

SFLs have been the requirement for many applications, such as wavelength division multiplexing (WDM) optical interconnects, spectroscopy, and optical pumping. The requirements for phase noise and linewidth of the SFLs vary with different applications. The linewidth requirement in optical communications depends on the modulation speed [56], and off-the-shelf components can be used directly for simple modulation formats. However, with higher order formats, such as (M-ary) quadrature phase shift keying (QPSK) and quadrature amplitude modulation (QAM), the linewidth requirements can be in the order of kHz [57]. This usually means using ECLs [58] or frequency stabilized DFB-LDs [59], [60]. On the other hand, for the most demanding applications, in addition to narrow linewidth also the phase noise has to be very low over a broad frequency range in order to enable low intensity signal detection.

Narrow linewidth emission in the 780 nm range is useful in *e.g.* optical parametric oscillators (OPOs), because it can be exploited to achieve large tuning ranges in mid-infrared (IR) [61]. It is also important in Rb pumping and in Rb-based atomic clocks [24]. Laser radiation is advantageous for these applications due to its narrow spectrum [24] and narrow linewidth has been a target for a large body of research in LDs at various wavelengths.

There are several ways to achieve single frequency operation in LDs. Single frequency in the context of this thesis refers to the laser operating in single transverse and single longitudinal mode. The different approaches for achieving single longitudinal mode operation include anti-reflection (coat-

ing) (AR)/high reflection (coating) (HR) applied to the LD facets, DFB
and DBR grating configurations, and notches in the LD RWG [62]. DBR
LD selects the emitted mode from the FP mode comb, given by the total
effective cavity length and group indexes therein [31], by having a narrow
high reflection band near the gain maximum. In a DFB LD the selection is
determined mainly by the feedback of the grating. Instead of the distributed
reflections of the DFB and DBR approaches, the mode selectivity in slotted
LDs is achieved via discrete reflections. When they are properly designed
they will decrease the threshold gain of only the mode that is designed to
lase [62]. In addition to these intrinsic methods, the spectrum of the single
mode can further be narrowed by external stabilization, such as locking to
a stable optical cavity slope by self injection [59] or a slope of an atomic
transition with a phase locked loop (PLL) style configuration [63].

1.2.2   Dual frequency laser diodes

Besides generating high frequency RF signals (MMWs) from the beating of
two laser lines from a DFL, it is also possible to encode the RF signal with a
data pattern, but usually this is achieved with external Mach-Zehnder mod-
ulators (MZMs) [64]. Data encoding is important especially in radio over
fiber (RoF) or 5G schemes [30], [65], [66]. It should be noted that the trans-
mission of data in *e.g.* MMWs is not the only technological problem with
5G, and the final implementation will be a vast multidisciplinary effort [67],
[68].

In addition to being used for carrier signal distribution, the laser light can
be modulated, either directly or externally, in order to transmit data signals
with the high frequency carriers. This can further help in designing power
and cost efficient base stations and other components of the network. The
direct modulation bandwidth of laser diodes is typically limited by the CPR.
However, when the cavity supports two modes, their interaction induces
photon density pulsations at a frequency that is the frequency difference
between the two modes [69]. When the cavity is properly designed, this PPR
can extend the direct modulation bandwidth of the DFLs considerably.

The approach presented in this thesis for achieving dual-longitudinal mode

operation, a dual quarter wave shifted (QWS) DFB grating, has been previously used for diode pumped fiber lasers with [70], [71] and without chirp [72], and with unequal phase shifts [73].

Other approaches are also possible, *e.g.* using non-phase shifted chirped gratings [74], different transverse modes [75], thermal tuning of two monolithically coupled DFB lasers [76], strongly gain-coupled multi-section DFB lasers [77], monolithically integrated dual-DBR lasers [78], [79], two lasers in a PIC [80] or in a laser system [64], integrated Y-branched DFB [81] or DBR [82], [83] lasers.

2. DESIGN AND SIMULATION

This chapter presents the design process and discusses the background theory
and its developments. The design procedure consists of 3 stages: epitaxial,
transverse, and longitudinal structure design. In the first stage the epitax-
ial structure is designed, including band structure, doping profile, refractive
index profile and their effects on optical gain, vertical optical field distribu-
tion, and current-voltage characteristics. The second stage is the transverse
structure design, and how it affects the single transverse mode (STM) op-
eration of the diode and the grating coupling coefficient. In the final stage
the longitudinal structure, including phase-shifts, longitudinal variations of
the grating, grating length and facet treatments, is designed using input
from the previous stages, having goals such as high side-mode suppression
ratio, reduced spatial hole burning, high output power, narrow linewidth for
SFLs, difference frequency range, difference frequency tunability and domi-
nant mode balance for DFLs.

2.1 Epilayer structure

The layer structure in the epitaxial growth direction, epilayer, determines
a large portion of the semiconductor laser operation and properties. These
include carrier transport, optical gain and loss, vertical optical guiding, and
thermal behavior.

The behavior of charge carriers (electrons and holes) in a semiconductor
material can largely be understood taking into account their drift and dif-
fusion: drift due to an external force from an electric field and the carrier
mobility, and diffusion due to a charge carrier concentration gradient within
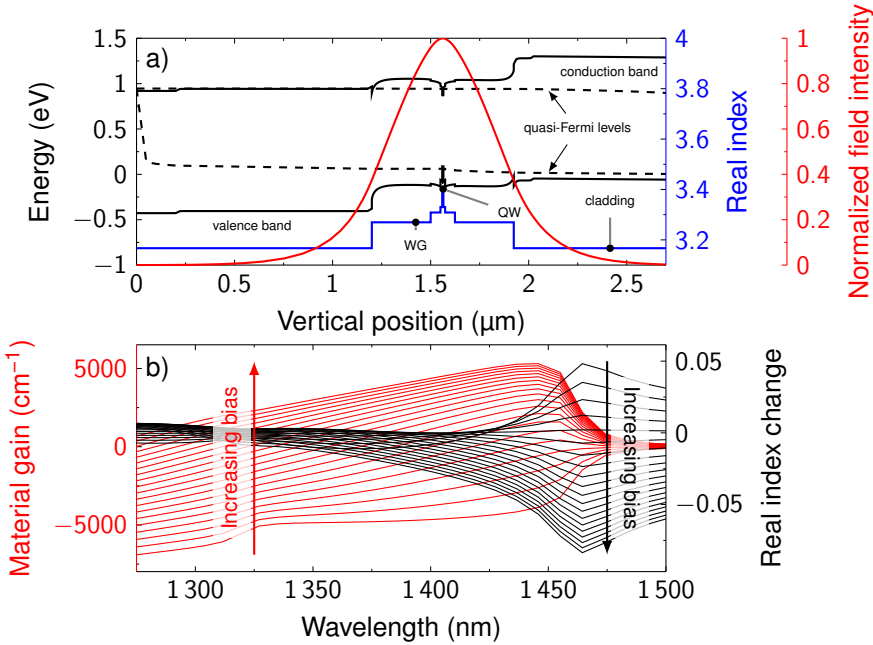the semiconductor and the diffusion coefficients of the carriers. These can

Figure 2.1 *a) Band diagram at around threshold bias, refractive index profile, and optical field intensity. b) Example of gain and the corresponding change in the real part of the refractive index for different carrier densities.*

be modeled using the drift-diffusion model [84], which can be derived from the more general Boltzmann transport equation [85], [86]. Drift-diffusion is widely used and for instance PICS3D from Crosslight Inc. [87] applies it to LD modeling. A band structure modeled with the drift-diffusion model is shown in Figure 2.1 a. Electrons are injected from the left and holes from the right and they recombine in the depletion region where the quantum well (QW) is. The refractive index and the resulting optical field intensity distributions in the vertical direction are also shown.

Stimulated radiative carrier recombination in the gain region, which is typically QW or bulk semiconductor, leads to photon generation and optical gain under the population inversion condition. In order to enable efficient light generation and amplification without requiring interaction with phonons, the gain region needs to be a direct bandgap semiconductor operating under

population inversion condition. The active region (*e.g.* QWs and barrier layers) is surrounded by waveguide (WG) layers which in turn are surrounded by cladding layers, typically n-type on the bottom and p-type on the top. WG layers are typically undoped, which induces only a small penalty to the diode voltage but can be beneficial for optical losses because *e.g.* free carrier absorption (FCA) is smaller. The vertical profile of the energy levels should provide a smooth carrier flow from the contact layers to the gain region as well as a good confinement in the gain region for both types of carriers. Therefore, the bandgap of the epilayers typically decreases gradually from the cladding layers towards the gain region and graded or intermediary composition barrier-reduction layers are inserted to reduce the notches in the energy levels at heterointerfaces with high bandgap variations.

The gain from the transitions between QW conduction and valence subbands can be modeled with a varying degree of sophistication, from *e.g.* simple parabolic band approximation [88] to more sophisticated methods based on the $\mathbf{k} \cdot \mathbf{p}$ perturbation theory [89]. Large hamiltonians (*e.g.* 16×16) in the $\mathbf{k} \cdot \mathbf{p}$ methods are essential for accurate gain calculations in highly strained dilute materials at low transition energies [90]. An example of LD gain as a function of carrier density obtained with the parabolic band approximation is shown in Figure 2.1 b. Heavy hole (hh) transitions induce transverse electric (TE)-polarized whereas light hole (lh) transitions induce predominantly transverse magnetic (TM)-polarized light emission, due to the symmetry of the associated orbitals [91]. By applying compressive or tensile strain to the semiconductor QW, the lh-hh degeneracy of the valence band (VB) can be lifted: the compressive strain makes the bandgap smaller for the conduction band (CB)-hh while the tensile strain decreases the CB-lh transition bandgap. Consequently, compressively strained QWs emit strongly predominantly TE-polarized and tensile strained QWs predominantly TM-polarized light [92]. In addition to changing the energy level separation and peak gain wavelength, the strain also reduces the valence band density of states [93], decreasing the threshold gain, and increasing the gain at a given carrier density [94].

Another aspect of epilayer design is the behavior of optical waves which get their energy from the stimulated and spontaneous emission events due

to radiative carrier recombination. Optical waves are electromagnetic fields and are governed by Maxwell equations [95]. Typically the analytical solutions are restricted to the most simple cases, and more realistic waveguiding structures need to be modeled by discretizing schemes, such as finite element method (FEM) [96] or finite differences (FD) [97]. For quasi-TE modes, under certain approximations, the Maxwell equations reduce to a scalar Helmholtz equation [97, pp. 132–133]

$$\nabla^2\psi + k^2\psi = \beta_0^2\psi, \tag{2.1}$$

where ∇ is over the transverse plane, ψ is the quasi-TE mode amplitude, and β_0 its propagation constant. In the epilayer design several issues need to be considered, including:

(1) what should the QW optical confinement factor Γ be;

(2) how much should the mode(s) extend outside the waveguide layers;

(3) how large should the transverse field distribution be.

The optical confinement factor in the QW area Γ of point (1) is defined in one dimension as

$$\Gamma = \frac{\int\limits_{QW}\psi^2\,dy}{\int\limits_{\Omega}\psi^2\,dy}, \tag{2.2}$$

where Ω is the whole calculation domain. This influences what is the modal gain and, possibly even more importantly, what is the modal gain difference between the fundamental (or desired) mode and all the other modes. Point (2) is important when considering what the grating coupling coefficient value κ can be, but also, especially for high power LDs, how much the field causes losses due to *e.g.* overlapping with areas having high FCA cross section and low carrier mobility [98]. Point (3) is important when considering the reliability and far-field properties of the LD. A broad ψ leads to a smaller power density for a given output power, which reduces the risk of catastrophic optical (mirror) damage (COD) [99]. The other benefit of a more spread out

ψ is the narrower far-field, which simplifies optical laser beam manipulation and coupling into *e.g.* optical fibers [99].

Separate confinement heterostructure (SCH) QW LDs have become the main type of LD epilayer structures due to their high efficiency. SCH implies the use of light confining WG in the epitaxial direction in addition to the carrier confining in the QW (or bulk) gain layer, so a SCH combines the properties of the carrier confinement and light guiding.

It should also be noted that the semiconductor properties depend on the temperature of its crystal lattice. As an example, the output power of a LD is typically limited by self heating if heat dissipation is not good enough. This results mainly from a decreased injection efficiency largely due to thermionic current leakage, leading to population inversion condition not being satisfied any longer. A good thermal conductivity over a small distance between the active region and the heat sink [12] reduces the effects of self-heating. To this end it is helpful to consider the layer thicknesses and compositions of the semiconductor carefully. Simple compositions and small thicknesses should be targeted as much as possible. Binary semiconductors have the best thermal conductivities out of semiconductor alloys, but the limited range of their properties usually lead to the need for using ternary or quaternary alloys instead. Unfortunately the ternary and quaternary crystal structure leads to a higher probability of scattering events and the thermal conductivity reduces roughly by an order of magnitude with increasing the compositional complexity of the semiconductor from binary to ternary and from ternary to quaternary. Possible heat sources are Joule heat, carrier recombination heat, Thomson heat, and optical absorption heat [84].

2.2 Transverse and grating structure

The 1D simulations described in the previous section are used in conjunction with the simulations of the transverse field distributions for designing complex transverse structures, such as RWGs, LC-RWG and ET-RWG surface gratings. For the basic case of RWG the wave propagating in the WG does not experience any feedback in the direction of propagation, apart from facet reflections.

Longitudinal reflections can be induced by perturbing the RWG. These reflections can be made frequency selective in order to favor certain longitudinal modes. LC-RWG and ET-RWG surface gratings, illustrated in Figure 1.2, are such perturbations. In a DFB (Figure 1.2 a-b) the frequency selection is done by periodically varying the effective refractive index along the whole length of the cavity, which causes reflections to the forward and backward traveling waves. Two longitudinal modes, placed at the first nodes on both sides of the grating reflectivity stopband, are lasing when the structure is longitudinally symmetrical and the gain spectrum is aligned with the grating reflectivity such that each mode experiences equal gain. This mode degeneracy can be lifted and a single mode is emitted when asymmetric AR-HR facet coatings are applied or when a phase-shift is introduced in the longitudinal structure of the grating. In contrast in a DBR (Figure 1.2 c-d) the perturbation is typically along a passive longitudinal section of the laser cavity, separate from the gain section, and the distributed reflection stopband selects the lasing mode from the FP mode spectrum by reducing its mirror losses. Thus, when the gain is aligned with the DBR grating reflectivity spectrum, the lasing mode has the smallest mirror losses. The FP spectrum is determined by the total cavity, including the DBR and all other cavity elements.

The frequency tuning of the DBR lasers is limited by the free spectral range (FSR) of the laser, as successive FP modes become periodically best aligned with the DBR reflectivity and material gain maxima. DFB lasers have a wider frequency tuning range since the stopband is typically wider than the FSR and since the FP modes, the reflectivity stopband, and the gain spectrum are all shifting in the same direction with temperature, albeit at different rates. The characteristics of the DFB laser, such as their wider wavelength tuning range, are strongly influenced by the phase of the facet reflections. Because the positions of the facets cannot be controlled accurately in the processing, the phases of the facet reflections affect the yield [100]. The influence of the facet reflections on the characteristics of DFB lasers can be reduced by applying AR coatings to the facets. A schematic of the transverse cross section of a DFB LC-RWG is shown in Figure 2.2. In the schematic the p-side cladding is etched away creating a RWG with a periodic lateral corrugation, which induces a periodic variation in the longitudinal profile of
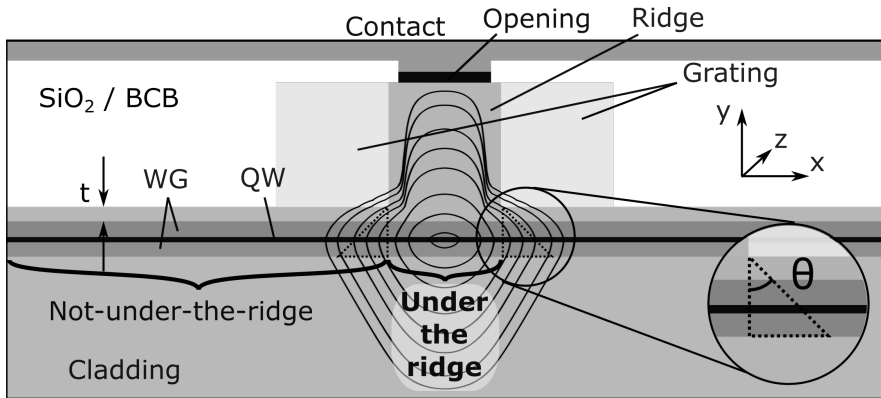
Figure 2.2 *Schematic of the transverse structure of a LC-RWG grating. The transverse distribution of the fundamental mode is overlaid on the structure. Adapted from [II].*

the effective refractive index.

The optical field ψ for a 3-dimensional laser structure is a vectorial field with a 3-dimensional distribution. However, because the gain in compressively strained QWs, the grating feedback, and the facet reflections favor the TE polarized light and because the transverse distribution of the optical field intensity is typically uniform along the longitudinal direction, a scalar quasi-TE variant of Equation (2.1) can be used to obtain ψ without large errors. The scalar equation assumes that the field is continuous in each point of the transverse plane. However, in reality the quasi-TE field has discontinuities where there are vertical (perpendicular to the field) discontinuities in the dielectric constant of the waveguide. Further errors arise from discontinuities in the z direction, because the structure is assumed longitudinally uniform. In the case of surface gratings the magnitude of the perturbation and the interaction between the guided mode and the grating is small. For such a situation it is possible to use a refractive index distribution that is averaged in z direction [101] and end up with usable results [102]. The benefit of applying the scalar wave equation to a longitudinally-averaged transverse refractive index distribution is the computational time saving and consequently the ability to scan large structural parameter ranges quickly in order to obtain qualitative trends in the structural-dependent performances. In the remain-

der of this section the scalar wave equation is applied to the study of STM operation and to the calculation of the coupling coefficient of LC-RWG and ET-RWG gratings.

2.2.1 Transverse mode discrimination

The transverse mode discrimination is an important quality of a RWG LD and is affected by the coupling between refractive index, carrier density, gain, and temperature transverse distributions [103]. In order to accurately determine the STM operation of a RWG LD, the optical distributions, carrier diffusion, gain, and thermal problems have to be solved self-consistently. This is computationally expensive and time consuming, and makes the device optimization slow. The approach presented in [104] is based on the optical cold cavity simulation alone and reduces the needed computation effort for each structural variant of a device. The method is extended to consider the effects of areas where the injected carrier density is reduced and the QW regions can be absorbing in [II].

In the calculation procedure the gain area in the transverse plane is divided into two parts, Ω_+ and Ω_-, which are the gain regions under and not under the ridge, respectively. For deeply etched RWG structures, the injected current flows mainly through the material placed under the ridge, creating gain in the active material under the ridge, while the rest of the active material is left largely unpumped and absorbing. Thus, such an approximation is justified especially for RWGs that are deeply etched and have a limited lateral diffusion of the injected current. The lateral current diffusion can be taken into account in this model by extending the reach of Ω_+ beyond the under-the-ridge area. A further approximation is that the gain is constant within the gain region under the ridge. Using these approximations, the modal gain for the mth mode can be written as

$$G_m = g^+ \frac{\iint\limits_{\Omega_+} \psi_m^2 \, dx \, dy}{\iint\limits_{\Omega} \psi_m^2 \, dx \, dy} = g^+ \Gamma_m^+, \qquad (2.3)$$

where g^+ $(g^+ > 0)$ is the approximated constant material gain in the pumped

active region under the ridge, ψ_m is the mth mode amplitude, Ω is the integration domain in the (x, y)-plane containing the transverse structure, and Γ_m^+ is the under-the-ridge confinement factor for the mode. A similar approximation can be done for the modal loss for the mth mode due to absorption in the active region belonging to the Ω_- domain:

$$\rho_m = -g^- \Gamma_m^-, \tag{2.4}$$

where g^- ($g^- > 0$) is the material absorption loss, which is approximated to be constant in the unpumped active material, and Γ^- is the not-under-the-ridge confinement factor for the mth optical mode.

Considering the step gain approximation that assumes g^+ constant material gain in the pumped active material and zero gain elsewhere, the STM operation is ensured when the modal gain of the fundamental mode is maximized with respect to all the other modes, *i.e.* when for every m

$$\Gamma_{1m}^+ = \frac{G_1 - G_m}{G_1} = \frac{\Gamma_1^+ - \Gamma_m^+}{\Gamma_1^+}. \tag{2.5}$$

When the transverse modes are ordered by their propagation constants, the lowest order modes are typically most confined under the RWG. Thus, it is enough to consider $m = \{2, 3\}$ for ensuring STM operation. Under these approximation, the following STM figure of merit can be derived:

$$\Gamma_{123}^+ = \Gamma_{12}^+ \cdot \Gamma_{13}^+. \tag{2.6}$$

$\left|\Gamma_{123}^+\right| \in [0, 1]$ and relatively high Γ_{123}^+ values (*e.g.* $\Gamma_{123}^+ > 0.6$) while $\Gamma_1^+ \geq \Gamma_i^+ \, \forall i \in \{2, 3\}$, indicate a high likelihood of stable STM operation. In order to extend the usefulness of this figure of merit to cases where the loss discrimination is important for mode selection, the absorption loss approximated by Equation (2.4) can be added to Equation (2.3) and the net modal gain becomes

$$G_m^{\text{net}} = G_m + \rho_m = g^+ \Gamma_m^+ - g^- \Gamma_m^-. \tag{2.7}$$

Assuming that the constant material gain in the active region under the ridge is equal to the absolute value of the constant material absorption loss

in the active region not under the ridge, the net gain difference between the fundamental and the mth mode can be re-arranged to

$$G_1^{\text{net}} - G_m^{\text{net}} = g \cdot \left(\Gamma_1^+ - \Gamma_m^+ \right) + g \cdot \left(\Gamma_m^- - \Gamma_1^- \right), \qquad (2.8)$$

where $g = g^+ = |g^-|$, from which a normalization similar to Equation (2.5) can be carried out:

$$\Gamma_{1m}^{\pm} = \frac{\Gamma_1^+ - \Gamma_m^+}{\Gamma_1^+} + \frac{\Gamma_m^- - \Gamma_1^-}{\Gamma_m^-}. \qquad (2.9)$$

An improved STM figure of merit can be derived by considering only the product of the net gain differences between the fundamental mode and the 2nd and 3rd modes, since they are typically more confined under the ridge and overlapping less with the absorbing regions than higher order modes. By then applying a normalization that takes into account that the absolute values of the net gain differences are in the $[0, 2]$ range, this figure of merit becomes:

$$\Gamma_{123}^{\pm} = \left(\Gamma_{12}^{\pm} \cdot \Gamma_{13}^{\pm} \right) / 4. \qquad (2.10)$$

The improved figure of merit, which takes values in the interval $[0,1]$ when both $\Gamma_{12}^{\pm}$ and $\Gamma_{13}^{\pm}$ are positive, indicates a high likelihood of STM operation when it has a relatively high (*e.g.* > 0.6) value with $(\Gamma_{12}^{\pm}, \Gamma_{13}^{\pm} > 0)$. Equations (2.6, 2.10) have been validated experimentally by stable STM operation achieved for RWG laser structures with different epilayer structures and operating at different wavelengths. The same figures of merit can be applied to LC-RWG structures by using the transverse optical field distribution calculated for the longitudinally averaged transverse refractive index distribution. Figure 2.3 shows the STM figures of merit calculated with Equations (2.6, 2.10) for 780 nm DFB lasers having an epilayer consisting of one 8 nm thick QW embedded between 120 nm thick undoped WG layers and surrounded by thick cladding layers ensuring that the optical field intensity is negligible at the neighboring layers. The simulated LC-RWG surface gratings had a variable thickness of the remaining un-etched p-side cladding, a variable width of the central ridge, a variable angle of the lateral current diffusion, and a constant 2.5 µm lateral extension of the grating protrusions.

The results in Figure 2.3 illustrate that by including the additional absorption term into the figure of merit, the optimal structural parameter range is narrowed, leading to a better indication of the optimum structural variant for achieving STM. The inclusion of different lateral diffusion angles for the injection current has little effect on the optimal design parameters. For (2.10) the structural range leading to a high STM figure of merit is slightly extended when θ is increased.
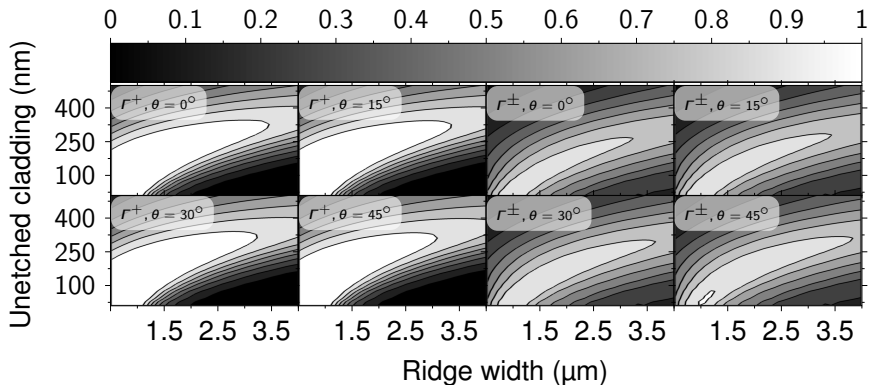

Figure 2.3 *LC-RWG DFB single transverse mode figures of merit Γ_{123}^{+} and $\Gamma_{123}^{\pm}$ as a function of ridge width and unetched cladding thickness with varying lateral current spreading angle θ. Adapted from [II].*

2.2.2 Coupling coefficient

The transverse simulation of the coupling coefficient uses the Fourier coefficients to approximate the longitudinal variation of the effective refractive index in straight rectangular gratings. The real part of the coupling coefficient is given by

$$\kappa_r = \frac{k_0{}^2}{2\beta_0 P_0} \iint\limits_{\text{Grating}} A_m(x,y)\psi_0^2(x,y)\,dx\,dy, \qquad (2.11)$$

where k_0 is the free space wave number, β_0 is the propagation constant of the fundamental mode in the WG, P_0 is the power of the fundamental transverse mode, A_m is the Fourier term of the mth order grating, ψ_0 is

the transverse distribution of the fundamental mode amplitude, and the integration is done over the transverse plane corresponding to the grating, *i.e.* where n is variable in the longitudinal z-direction. The propagation constant is defined by the effective refractive index of the corresponding mode, n_{eff0}, as

$$\beta_0 = n_{\text{eff0}} \frac{2\pi}{\lambda}, \tag{2.12}$$

where n_{eff0} can be obtained from the eigenvalue associated with the fundamental mode solution to the Helmholtz equation applied to the transverse distribution of the longitudinally averaged refractive index.

The general Fourier terms for m^{th} order gratings are [105]

$$A_m(x,y) = \frac{1}{\Lambda} \int\limits_{-\Lambda/2}^{\Lambda/2} n^2(x,y,z) \exp(-j2\pi mz/\Lambda)\, dz, \tag{2.13}$$

where Λ is the grating period, n is the refractive index, m is the grating order, and x, y and z are the spatial coordinates as shown in Figure 2.2. For rectangular gratings the mth order grating Fourier term simplifies to [II]

$$A_m = \left(n_2^2 - n_1^2\right) \cdot \frac{\sin(\pi m\gamma)}{\pi m}, \tag{2.14}$$

where n_2 and n_1 are the refractive indices of the longitudinally alternating unetched and etched grating regions, respectively, and γ is the fill factor of the grating. The fill factor and the longitudinally averaged transverse refractive index distribution $n_0(x,y)$ are linked by the longitudinally averaging formula:

$$n_0^2(x,y) = \gamma \cdot n_2^2(x,y) + (1-\gamma) \cdot n_1^2(x,y). \tag{2.15}$$

In general the Fourier coefficient can vary in the (x,y)-plane, and the real part of the coupling coefficient for the fundamental mode in an ideal rectan-

gular grating becomes [II]

$$
\kappa_r = \frac{k_0^2}{2\beta_0 P_0} \cdot \left(\iint\limits_\Omega n_2^2(x,y)\psi_0^2(x,y)\,dx\,dy - \right.
$$

$$
\left. \iint\limits_\Omega n_1^2(x,y)\psi_0^2(x,y)\,dx\,dy \right) \cdot \frac{\sin(\pi m\gamma)}{\pi m}. \tag{2.16}
$$

When the refractive index in the grating area is constant in each of the successive grating slices, the coupling coefficient can be calculated with [II]

$$
\kappa_r = \frac{k_0^2}{2\beta_0} \cdot \left(n_2^2 - n_1^2 \right) \cdot \Gamma_g \cdot \frac{\sin(\pi m\gamma)}{\pi m}, \tag{2.17}
$$

where Γ_g is the confinement factor of the respective mode in the grating area. For buried gratings, where the refractive index contrast between n_2 and n_1, both of which typically correspond to semiconductor materials, is small and the above expression simplifies to [II]

$$
\kappa_r \approx \frac{2\left(n_2 - n_1 \right)}{\lambda_0} \cdot \Gamma_g \cdot \frac{\sin(\pi m\gamma)}{m}, \tag{2.18}
$$

which is generally not valid for surface gratings, because there the refractive index contrast between n_2 and n_1 can be large and $n_2 + n_1 < 2 \cdot n_{\text{eff0}}$.

The above equations, including Γ_g, cannot be applied when the refractive index varies within the grating area in the grating slices. In such cases the coupling coefficient can be expressed with the help of effective refractive indices as [II]

$$
\kappa_r = \frac{k_0^2}{2\beta_0} \cdot \left(n_{\text{eff2}}^2 - n_{\text{eff1}}^2 \right) \cdot \frac{\sin(\pi m\gamma)}{\pi m}, \tag{2.19}
$$

where n_{eff2} and n_{eff1} are the effective refractive indices in the unetched and etched grating slices, respectively. Effective refractive indices cannot be obtained by applying a Mode Solver to refractive index distributions n_2 and n_1 directly, because that would lead to boundary condition violations in the longitudinal direction. The violations can be circumvented by applying

the Mode Solver to a longitudinally averaged transverse refractive index profile, given by (2.15), and using the convolution between the obtained transverse optical field and refractive index distributions in the grating slices, for calculating the effective refractive index values in the grating slices as [II]:

$$n_{\text{eff}i}^2 = \frac{\iint n_i^2 \psi_{0,\text{avg}}\, dx\, dy}{\iint \psi_{0,\text{avg}}\, dx\, dy} - \frac{\iint (\nabla\psi_{0,\text{avg}})^2\, dx\, dy}{k_0 \cdot \iint \psi_{0,\text{avg}}\, dx\, dy}, \qquad (2.20)$$

where $\psi_{0,\text{avg}}$ is the transverse optical field profile for the longitudinally averaged transverse refractive index distribution and n_i is the transverse refractive index distribution in the ith grating slice. It is enough to evaluate the first term in (2.20), because the second terms cancel each other in (2.19).
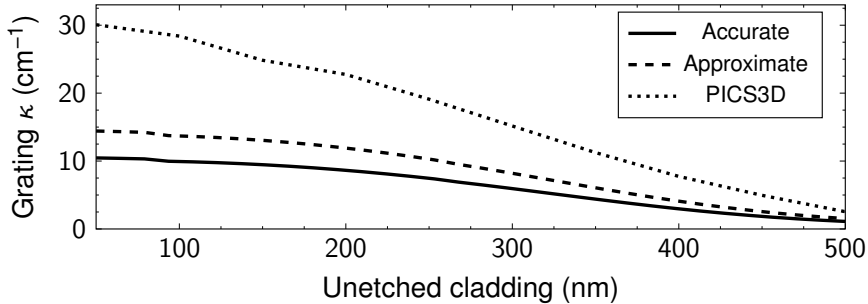
Figure 2.4 LC-RWG grating coupling coefficient variation with unetched p-side cladding thickness, calculated with PICS3D 7.3 (version 2006.11.01) and determined using the accurate Equation (2.19) and the approximate Equation (2.18). Adapted from [II].

Figure 2.4 illustrates the coupling coefficient variation of a LC-RWG surface grating with the thickness of the un-etched cladding layer, calculated by the commercial software PICS3D (version 2006.11.01), by using the exact Equation (2.19) and the approximate Equation (2.18).

From Equation (2.16) it is clear that κ_r varies strongly with γ. On the other hand, when the fill factor also has a strong influence on Γ_g, the effect of the Fourier coefficient is deformed as given by Equation (2.16) and illustrated in Figure 2.5. An important observation illustrated by the figure is that similar trench widths, which are the limiting factor in the fabrication of the surface gratings, give similar coupling coefficients for gratings of different
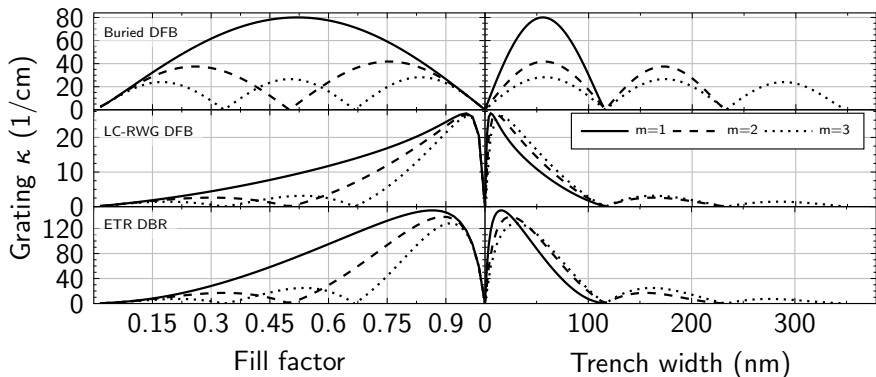
Figure 2.5 *Grating coupling coefficient variations with the filling factor and with the grating trench width for 1st, 2nd and 3rd order buried DFB, LC-RWG DFB, and ETR DBR gratings. Adapted from [II].*

orders. This relates to the higher order gratings having a smaller longitudinally averaged transverse refractive index contrast when compared with lower order gratings with the same trench widths, and thus having a higher confinement in the grating regions [I].

Similar results have been obtained also with *e.g.* CAMFR software [106], which indicates that the approximation that the electric field is continuous everywhere in the calculation domain (which is induced by using the scalar Helmholtz equation) does not cause qualitative errors.

An important aspect of the coupling coefficient is related to the radiating modes, associated with the imaginary part of the coupling coefficient. In spite of the associated extra losses, the radiating waves can be beneficial to the yield of the fabricated devices [100]. In general κ is a complex variable, and from coupled mode theory it can be derived [31, pp. 349] that the amplitude reflectivity at zero detuning (at the Bragg resonance wavelength) is

$$r = \frac{i\kappa^{\star}}{|\kappa|} \tanh(|\kappa|L), \qquad (2.21)$$

where $\kappa^{\star}$ is the complex conjugate of the complex coupling coefficient and

L is the grating length. The intensity reflectivity in this condition is then

$$R = \tanh^2(|\kappa|L). \tag{2.22}$$

Using Equations (2.21–2.22) the coupling coefficient of a grating can be approximated from the reflectivity spectrum, which can be modeled with *e.g.* CAMFR [107][1], which takes radiative modes into account [106]. For surface gratings this evaluation yields large imaginary parts of the coupling coefficient over a large range of the grating fill factor. The use of CAMFR is straighforward for structures that can be described with rectangular geometry and that span quasi-indefinitely in one dimension, *i.e.* for wide DBR gratings. The coupling coefficient dependence on the grating filling factor and on grating trench width for 1$^{\text{st}}$, 2$^{\text{nd}}$ and 3$^{\text{rd}}$ order ET-RWG gratings calculated using CAMFR and Equations (2.21–2.22) and taking the absolute value (denoted as CAMFR (method 1)), CAMFR and the method described in [108] (denoted as CAMFR (method 2)), and (2.16) and a scalar field Mode Solver (denoted as MS) are compared in Figure 2.6. The κ from CAMFR depends strongly on the length of the cavity, especially for short cavities, and accordingly the value chosen is for a length for which the variation in the evaluated κ as a function of grating length is small.

The differences in the evaluated κ derive from taking or not taking radiating modes into account and from the mode mistmatch between the injecting straight RWG and the ET-RWG DBR grating. By using long enough grating in the simulation, this longitudinal boundary effect can be minimized. When evaluating κ according to [108], the difference to the result obtained by mode solver approach is small, but in the regions where the fill factor leads to a vanishing Fourier coefficient for the rectangular grating and the mode solver calculated κ is zero, the CAMFR based approaches indicate a relatively smooth variation of κ, without reaching a zero value. The difference between the coupling coefficient values calculated with MS and with CAMFR, especially in the grating filling factor regions where the Fourier coefficients vanish, indicate that radiative the waves have a significant impact on the grating strength when the grating Fourier coefficients are small. This also suggests that surface grating strength can be tolerant against grating

---

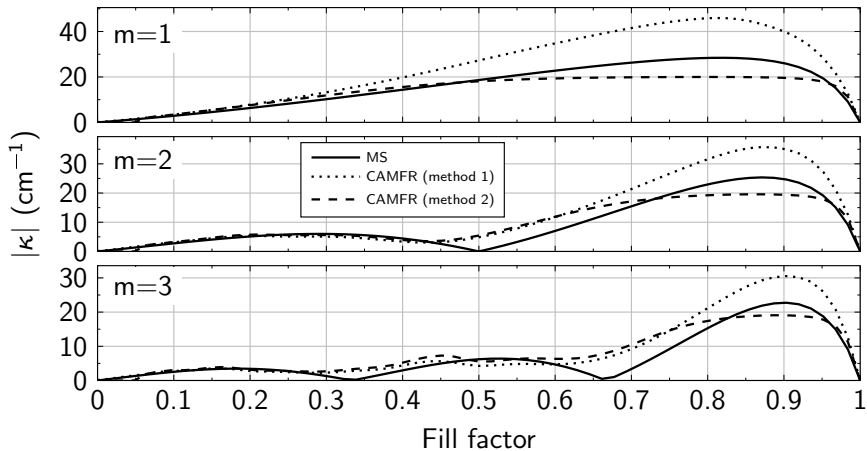[1]CAvity Modelling FRamework, available from `http://camfr.sourceforge.net/`

Figure 2.6 *Absolute value of κ simulated for a wide (W ≫ λ) ET-RWG grating as a function of grating filling factor for an example structure operating at $\lambda_{Bragg} \approx 1550$ nm, and having 800 nm thick WG layers on both sides of the active region, and t=50 nm remaining unetched cladding thickness. The variations labeled MS were calculated with Equations (2.1) and (2.16); the variations labeled CAMFR (method 1) were calculated with CAMFR and Equations (2.21–2.22); and the variations labeled CAMFR (method 2) were calculated according to the method described in [108]; the results using CAMFR [107] calculated reflectivities were obtained for a 500 μm long cavity.*

filling factor variations, which can result from *e.g.* the etching process.

2.2.3 Wider LC-RWG grating trenches by alternating placement of the lateral grating protrusions

Typically the best diffraction efficiency and lowest radiative losses come from gratings with the lowest order, but on the other hand radiative losses may also benefit mode selectivity [109]. Especially for short Bragg resonance wavelengths the surface gratings with first order patterns lead to very narrow trenches. Typically, due to the epitaxial design, the etching depth is usually over a micron, which means that the aspect ratios of the etched gratings can become high. The aspect ratio is the ratio between the grating trench depth and width. The technologically achievable etching aspect ratio is typically not higher than 10, which restricts the possibility to fabricate 1st order

surface gratings for short wavelengths in the ranges below 1000–1300 nm, for instance. Higher order gratings alleviate this problem, but they can reduce the coupling coefficient and increase the losses.

A low order LC-RWG grating with alternating lateral protrusions can be employed to circumvent the etching aspect ratio limitation. The alternating lateral protrusions are obtained by removing the grating protrusion alternately from one side and from the other side of the central ridge. In such a LC-RWG grating structure the trench width can be enlarged to a value beyond the grating period, as illustrated in Figure 2.7. It should be noted that the longitudinal effective refractive index profile remains similar after alternately removing the lateral protrusions. This removal reduces the longitudinal refractive index contrast, while keeping the same grating order and period with the effective refractive index discontinuities at the same longitudinal positions.
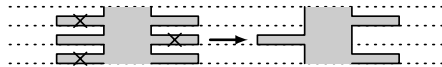
Figure 2.7 *Schematic illustration of increasing the trench width by removing the LC-RWG grating protrusions alternately from one and from the other side of the central ridge.*

The alternating placement of the lateral protrusions increases the trench width from $(1-\gamma)\cdot\Lambda$ to $(2-\gamma)\cdot\Lambda$ where γ is the grating fill factor before the process of alternately removing the grating protrusions, $\gamma=\Lambda_1/\Lambda$, where Λ and Λ_1 are the grating period and the protrusion width in the longitudinal direction, respectively. Since $\gamma<1$ the trench width for the alternating placement of the lateral protrusions is larger than the grating period. The alternating protrusion placement has a two-fold effect on the grating coupling coefficient. On one hand, at each grating interface the optical field confinement in the grating area is essentially halved when compared to the initial grating, which leads to a reduction to the coupling coefficient. On the other hand, when the grating trenches are of similar widths, the alternating LC-RWG gratings have a lower transverse contrast, resulting in a higher optical confinement factor in the grating regions, which compensates for interacting with the optical field only on one side of the ridge at a time.

It was noted in [I] that the MS-calculated coupling coefficient variation as a function of grating fill factor for a first order alternating and a second order symmetrical lateral gratings are similar. The radiative losses of the first order alternating grating were not analyzed, but it can be assumed that they are smaller than the radiative losses of the second order symmetrical gratings.

As a consequence of the particularities of the gratings with alternating lateral protrusions, these gratings enable achieving a similar or higher coupling coefficient for the same technological limitation imposed to the grating trench width by the achievable etching aspect ratio between trench depth and width.

The alignment accuracy of a photolitography mask is in the order of a few micron which sets a prerequisite that the contact opening on top of the grating structure is more than the central ridge width, say 4 micron openings for 2 micron central ridge width, for example. Depending on the width and the placement of the contact opening, it can overlap with the protrusions considerably. The current injected through the grating protrusions contributes little to the laser gain, undergoes losses at the interfaces between the grating and the planarization material, creates heat, and can pump unwanted lateral side modes and thus does not contribute positively to the lasing [110]. The lateral current leakage through the lateral protrusions of the gratings is reduced for the alternating gratings and can be suppressed by lateral oxidization that closes the current paths through the protrusions or by using recessed lateral gratings with a height below the central ridge height.

2.3 Optimization of single frequency gratings

The phase condition and the losses associated with the longitudinal structure of the LD determine the selection of the longitudinal modes lasing in the cavity. For simpler structures, such as FP or uniform DFB grating LDs, these mode losses can be solved analytically, but if the grating consists of multiple sections separated by arbitrary phase shifts, a numerical approach is better suited. The two typical numerical approaches to solving these longitudinal mode structures are the transfer matrix method (TMM) [111] and the coupled mode theory (CMT) [112], [113]. These methods are based

on similar approximations [114]. In TMM the structure is split into thin longitudinal slices with constant refractive index and the 1D propagation of a plane wave through the successive slices is described by transmission and reflection matrices. The total structure can then be described as the product of these matrices, and the resulted overall matrix for the whole succession of grating slices can be used to determine the resonance condition, transmission, and reflection. CMT in its numerical implementation form works much the same way but typically considers transmission and reflection matrices for longitudinal sections that have uniform properties (*e.g.* κ), although they may not be structurally longitudinally uniform: a section may be for example a uniform grating section, a phase-shift, a uniform amplifier, or an attenuator section. Both methods can be used to describe structures with almost any arbitrary longitudinal structures. However, CMT requires that the length of each uniform block is $\gg \lambda$, which somewhat restricts the use of the method from being applied to structures with non-uniformly and closely placed sharp longitudinal variations.

2.3.1 Linewidth

There are several steps that can be taken in order to minimize the laser linewidth, *e.g.* blue-shifting the Bragg resonance wavelength with respect to the gain maximum wavelength or having a low κ in a long DFB cavity with AR coated facets [115]. There are also effects such as gain saturation [116], [117], spatial hole burning (SHB) and parasitic losses [116] that need to be taken into account when choosing κL. Relatively low κL values and long gratings have been used when aiming for a narrow intrinsic linewidth [118]. A low κL means that the longitudinal field intensity profile inside the cavity will be relatively flat, which enables high powers without the SHB penalty and, because the linewidth is inversely proportional to the output power (neglecting SHB), this leads to a narrower achievable linewidth. Low κ requires long cavities to reach high enough κL, which leads to a longer photon lifetime [119], which decreases the linewidth. The linewidth can be evaluated from [118]

$$\Delta\nu_{\text{FWHM}} = \frac{c^2 h\nu K n_{\text{sp}} g_{\text{th}} \left(g_{\text{th}} - \alpha_{\text{int}} \right)}{4\pi n_g^2 P_0} \left(1 + \alpha_{\text{eff}}^2 \right), \qquad (2.23)$$

where c is the speed of light in vacuum, h is the Planck constant, ν is the laser frequency, K is the Petermann's K-factor, n_{sp} is the spontaneous emission rate, g_{th} is the threshold gain, α_{int} is the internal optical losses, n_g is the group index, and α_{eff} is the the effective linewidth enhancement factor. K, which is related to the coupling of the spontaneous emission noise into the lasing mode [120], has a direct impact on the linewidth and is typically evaluated separately for the transverse [120] and longitudinal [121] modes [122]. In the longitudinal evaluation it is assumed that diffractive losses in the laser cavity are negligible [121], which may not always be a valid approximation for surface gratings. For the longitudinal structure K can be written as [122]

$$K = \left| \frac{\int |\psi(z)|^2 \, dz}{\int \psi(z)^2 \, dz} \right|^2 . \tag{2.24}$$

and has a reduced value when the longitudinal distribution of the optical field is relatively flat.

The linewidth enhancement factor α_{eff} is defined as the ratio between the change in the refractive index and the change in the gain as a function of carrier density [31]

$$\alpha_{\mathrm{eff}} = -\frac{4\pi}{\lambda} \frac{dn/dN}{dg/dN}, \tag{2.25}$$

where the sign is conventionally chosen for obtaining a positive linewidth enhancement factor from a negative variation of the refractive index with increasing carrier density and a positive variation of the gain with increasing carrier density. The photon lifetime inside the laser cavity τ_p is related to the total optical cavity losses and modal threshold gain by [31]

$$\alpha_{\mathrm{int}} + \alpha_{\mathrm{m}} = \Gamma g_{\mathrm{th}} = \frac{c}{n_g \tau_p}, \tag{2.26}$$

where α_{m} are the mirror losses. Thus the optimization of the material gain, low internal and mirror losses, a high differential gain dg/dN, and a low effective refractive index variation with carrier density (dn/dN) are important when targeting narrow linewidths. A high optical confinement confinement of the optical field in the active region should also be targeted.

There are many structural ways of decreasing the linewidth of DFB or DBR lasers besides reducing the mirror loss. Distributed phase shifts [123], gaps in the grating [124], and longitudinally varying κ and period [125]–[133] have been used in order to modify the longitudinal photon distributions inside the cavity and consequently the strength of SHB. Effective longitudinal variation in several parameters can also be realized by using multi-electrode structures [127], but care has to be taken how those kind of structures are biased. Due to fabrication inaccuracies, it may be that calibration is required for nominally identical devices.

2.3.2 Modulation frequency

The carrier-photon relaxation resonance frequency of a laser diode, which can be used to roughly estimate its modulation bandwidth, is given by [31]

$$\omega_r^2 \sim \frac{cdg/dN N_p}{\tau_p n_g} = \frac{c\Gamma dg/dN}{qV}\eta_i\left(I - I_{\mathrm{th}}\right), \qquad (2.27)$$

where dg/dN is the differential gain, N_p is the photon density, q is the elementary charge, V is the active region volume, η_i is the internal quantum efficiency, I is the applied bias current, and I_{th} is the threshold current. Comparing Equations (2.23, 2.26, 2.27), it is evident that the linewidth reduction and the increase in the CPR frequency benefit from a high emission power. It is also revealed that low internal and mirror losses are associated with a high photon lifetime in the cavity, resulting in a narrow emission linewidth. On the other hand, the long τ_p, required for a narrow linewidth, leads to a poor ω_r. Also for high ω_r the active region volume should typically be minimized, which requires a high Γ and a short cavity. This also means that κ should be high in the case of DFB LDs. There are other factors that also need to be taken into account such as SHB, power densities at laser facets, which may lead to COD, and gain compression, which may limit the maximum power and mode volumes.

Narrow linewidth and fast modulation speed of a laser diode are thus contradictory design targets, and need different approaches.

2.3.3   Single longitudinal mode and yield

The single longitudinal mode (SLM) yield is also another factor affecting the design decisions related to the longitudinal structure of the lasers. It has been analyzed for gain- and index-coupled DFBs [100], [134] and it was found that in addition to the uncontrollable phases of the reflections from the facets, the SHB effect plays an important role in determining the yield. Because for the lasers studied in this thesis the output characteristics were usually governed by the grating structure, AR coatings were typically applied. Also the employed surface gratings are at least partly complex-coupled and have a relatively high κL [105] which means that the effects of facet phases are reduced even for moderate facet reflectivity values [100]. This means that the yield for our lasers may be more determined by the SHB effects than by the random facet positions. It should also be noted that the randomness in the fabricated lasers' material properties and structural dimensions plays a role in determining the actual yield. Research purpose growth chambers for the epilayers are relatively small, which can lead to variation in the growth quality within a wafer [135]. In addition, there may be random effects in the processing, resulting for example from impurities in the atmosphere or from variations in the processing chemicals. These fabrication imperfections create many sources of incontrollable randomness.

2.4   Dual frequency gratings

A typical DFB grating modifies the modal spectrum of a LD with single longitudinal mode operation as the main target. By modifying the grating structure the target can be changed to favoring the emission of two (or more) modes. Our approach is to use periodic phase-shifted distributed feedback (PPS-DFB) gratings: the uniform Bragg grating is perturbed by two or more ($P{\geq}2$) phase shifts of an odd multiple of $\lambda/4$. When the $P{\geq}2$ phase shifts are placed periodically along the grating, with M grating periods between phase shifts, the reflection spectrum has two maxima (stopbands) with Bragg resonances separated by [IV]

$$\Delta\nu_{\mathrm{Bragg}} = \nu_{\mathrm{Bragg}}/(m \cdot M), \tag{2.28}$$

where ν_{Bragg} is the Bragg frequency of the initial grating before being perturbed by the introduction of the periodic phase shifts. ν_{Bragg} falls between the two resulted reflectivity maxima (stopbands). As explained in [IV], the introduction of periodic phase shifts separated by M grating periods is equivalent with superposing two gratings of different periods, resulting in a grating modulated with a $2 \cdot M$ period; with the two resulted maxima/stopbands corresponding to the superposed gratings. M and κ are the main parameters for the structural control of the difference frequency, because their values can be finely varied. M takes integer values, but when κ is relatively low, a larger M value is needed for ensuring a reasonably high κL and a proper dual-mode operation. For example, an M value of 100 leads to a minimum resolution of the designable difference frequency of around $1\,\%$ relative to (2.28). The number of grating sections, $P+1$, can also be incremented to increase the mode spacing, but the difference frequency varies in much larger discrete steps, especially for small values of $P \geq 2$. Another difficulty in using P for changing the difference frequency is that its variation influences the total device length in much larger steps than M does.

The modal and reflection spectrum of a PPS-DFB grating can be modeled by TMM or CMT. Both methods require information about the n_{eff0} and κ or n_{eff2} and n_{eff1}, which can be obtained as outlined in section 2.2.2. The reflectivity spectrum variation with the number of phase-shifts and the positions of the dominant modes (for gratings having the same number of periods between phase-shifts) is illustrated in Figure 2.8. κL is kept constant while the grating length increases with increasing P. Constant κL leads to approximately constant maximum values of the grating reflectivity, but to changing mode positions and spectrum shape. The P nodes between the stopband maxima are visible, and it is clear that the mode separation increases with P. Another important aspect illustrated by the figure is that the lowest α_{m} are obtained at the reflectivity nodes closest to the inner edges of the two stopbands. When the maximum gain is placed properly and the gain dispersion is suitable, the two modes with wavelengths close to the reflectivity nodes next to the inner edges of the two stopbands are lasing. Thus the mode separation can be roughly designed by changing the stopband distance found from Equation (2.28) and the stopband width. The modes are not exactly at stopband half-width away from the reflection maxima nor are
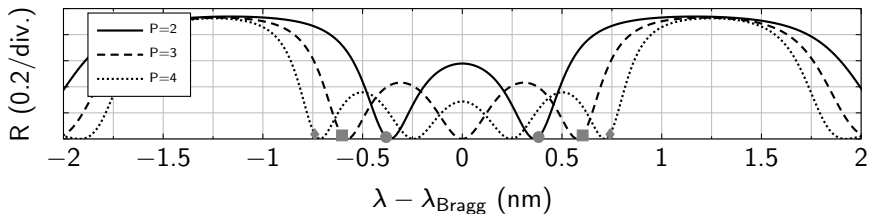
Figure 2.8 *Grating reflectivity and dominant mode positions for gratings with 2 (●), 3 (■), and 4 (♦) phase shifts. $M = 200$, $m = 3$, $\gamma = 0.5$, and $\kappa L = 3$. Adapted from [IV].*

they exactly placed at the reflection nodes. However, their exact positions, determined by the needed round-trip gain and phase conditions, correspond to a difference frequency that can be approximated with a reasonable accuracy from the stopbands' width and Bragg resonances' separation. For an arbitrary cavity the exact mode positions have no general and simple analytical expression. A reasonably good analytic approximation formula for the difference frequency can be obtained by subtracting the approximate stopband width from the difference between the two Bragg resonances [IV]

$$\Delta\nu_{\mathrm{modes}} \approx \Delta\nu_{\mathrm{Bragg}} - \Delta\nu_{\mathrm{sb}}, \tag{2.29}$$

with the node-to-node width of a single stopband $\Delta\nu_{\mathrm{sb}}$ approximated by

$$\Delta\nu_{\mathrm{sb}} \approx S \cdot \sqrt{\left(\frac{\Delta n}{2n_{\mathrm{eff0}}}\right)^2 + \left(\frac{1}{M \cdot (P+1)}\right)^2}, \tag{2.30}$$

where S is a fitting parameter depending on cavity parameters and Δn is the effective refractive index contrast between alternating grating slices. It was found that $S \approx 1.8/m \cdot (1 - 0.1\kappa L)$ gives a reasonably good fit for a large range of grating configurations with errors in the 10% range when compared to TMM results.

2.4.1 Difference frequency generation

Generating a MMW (or another high frequency RF) signal from the dual-mode emission requires photodetection, which is a nonlinear process where

the electric field in a fast semiconductor is modulated by the varying optical field intensity resulted from the beating of the two emitted modes. Overlapping and parallel beams with the same or similar polarization states are beneficial for the photodetection efficiency, which is also typically higher the lower the beat frequency is in the MMW and sub-MMW bands [136]. The mutual coherence between the two photodetected laser modes is relevant when considering the linewidth of the generated electric signal, and it has also been demonstrated that perfect coherence leads to higher generated electrical signal intensities, possibly larger than the sum of the intensities of the two optical modes [137]. The difference frequency ranges of the fabricated dual-mode lasers were designed to fit within the bandwidth of a typical high-speed InGaAs photodiode with $50\,\mathrm{GHz}$ $3\,\mathrm{dB}$ bandwidth[2]. The photodiode is fiber-coupled and due to the perfectly overlapping transverse distribution of the two modes at the laser output there are little extra losses apart from the losses resulting from fiber coupling.

An important aspect of the generated MMW is its phase stability and linewidth. When the laser modes partaking in the photodetection process have identical spectral densities and are thus perfectly coherent, the generated beat-signal linewidth can be substantially narrower than the linewidths of the beating modes [137]. The fact that the optical dual frequency signal is generated within the same cavity, from the same gain medium and interacting with the same grating, indicates the possibility of a high degree of correlation and coherence between the two modes, which can reduce the linewidth of the generated MMW signal. The possible linewidth reduction is derived from sharing most of the random noise sources, which can lead to a higher degree of mutual coherence between them [137] and to the common noise rejection effect [138], [139]. Nonlinear cavity effects, such as four-wave mixing (FWM), can also be used to reduce the linewidth of the generated beat signal below to the linewidths of the laser modes [140]. There are other effects, however, which degrade the difference frequency signal quality, such as mode competition: based on Lamb's theory, a bulk or QW LDs cannot emit in stable dual frequency regime if the modes are interacting with each other too much [141]. This is counteracting the correlation resulted from sharing the cavity, grating interaction and gain medium, and it can lead to

---

[2]`https://www.finisar.com/communication-components/xpdv2320r`

relatively broad MMW signal linewidths, with full width at half maximum (FWHM) in the range of MHz. The surface gratings can compensate the linewidth enlargement effects due to the fact that they reduce the detrimental effects of the uncontrollable facet reflection phase. This enables the use of higher reflecting facets, which can decrease the linewidth of the emitted modes by an order of magnitude when compared to employing AR-coated facets [IV].

3.   EXPERIMENTAL RESULTS AND DISCUSSION

This chapter presents the characterization procedures and discusses the results obtained for the studied single and dual frequency LDs. The results are compared with the design goals and the sources of the differences are analyzed.

3.1   Single frequency lasers
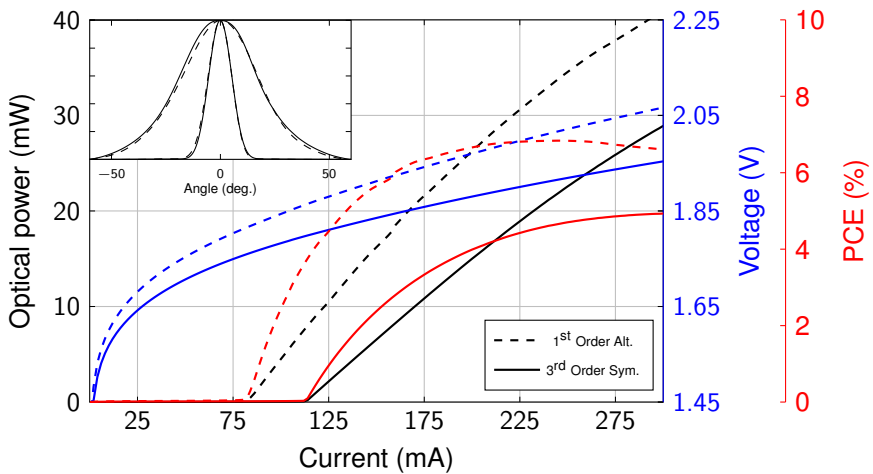
Figure 3.1 *Light-current-voltage (LIV), power conversion efficiency (PCE), and far-field (FF) characteristics of DFB LD with LC-RWG surface gratings having symmetrically placed and alternating lateral protrusions. Adapted from [I].*

The LIV characteristics of all the reported single contact LDs were measured by a standard procedure which includes a temperature stabilized base plate,

pulsed and continuous wave (CW) current sources, and voltage and power meters. FF measurements were also carried out and the spectral characteristics were measured by coupling the laser light into a single mode fiber leading to an optical spectrum analyzer.

An example of LIV and FF characteristics measured for 780 nm DFB LDs having LC-RWG surface gratings is given in Figure 3.1. The devices employed 3rd-order gratings with symmetrically placed lateral protrusions and 1st-order gratings with alternating lateral protrusions, described in section 2.2.3. Otherwise the device parameters were almost identical: they were fabricated from the same epiwafer, had the same length, had the same central ridge width and lateral extension of the protrusions, and had similar trench widths and coupling coefficients. From the figure it is clear that when comparing the two devices, the alternating grating scheme has no effect on the far field while its benefits include a lower threshold current, a higher slope efficiency, and a better PCE. In addition the mode-hop free tuning range is similar for the two grating variants [I]. We attribute the improvements in the characteristics of the DFB LDs with alternating LC-RWG surface gratings to the lower grating order and to the smaller overall area of the grating protrusions. The lower grating order reduces the radiative losses as discussed in section 2.2.2, while the smaller protrusion area reduces the lateral current leakage through the grating protrusions, without requiring additional processing steps.

Both gratings also show mode-hop-free tuning range over the whole lasing range with similar detuning between the Bragg resonance and maximum gain wavelengths, which means that the mode selection is almost identical for the two devices. The lasers were 2.4 mm long with low κ, targeting narrow linewidth emission. This resulted in over 50 dB side mode suppression ratio (SMSR) values over a wide bias range also for both devices [I], and the linewidths of the emitted mode in the normal devices was later determined to be below 15 kHz over a wide bias range [32] and the linewidth of the devices with alternating grating was determined to be below 10 kHz over a similar bias range [142]. The measured linewidths from these grating structures have been compared in Figure 3.2. The linewidth was extracted from the power spectral density (PSD) obtained from a delayed self-heterodyne
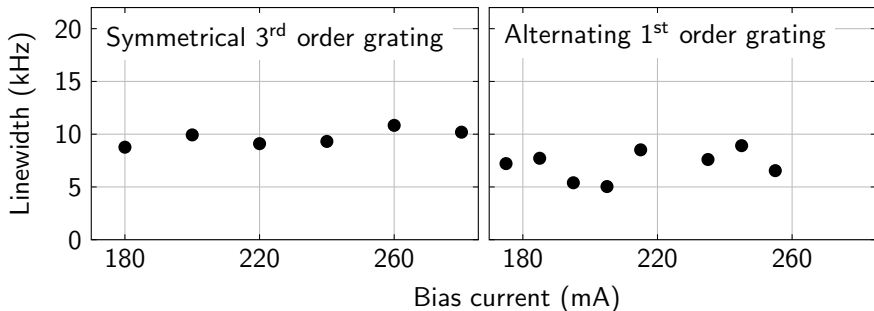
Figure 3.2 *Linewidth from 3rd order symmetrical and 1st order alternating grating LC-RWG DFB lasers emitting around 780 nm. The linewidth has been evaluated from a delayed sub-coherence self-heterodyne measurement [32]. Adapted from [32], [142]*

measurement with a delay length shorter than the coherence length of the lasing mode [143]. The measured linewidth is not decreasing consistently with increasing current and power and then increasing after reaching its minimum as would be the normal behavior [144]. This indicates that the linewidth broadening caused by noise from sources outside the laser (i.e. technical noise), such as the current driver, dominate in the experimentally-determined linewidth. Since the technical noise has a bigger contribution to the measured linewidth than the intrinsic laser linewidth (re-)broadening effects, *e.g.* caused by SHB [145], it can be inferred that the intrinsic laser linewidth is significantly narrower than the measured linewidth.

3.2 Dual frequency lasers

The characterization of DFLs requires three independent direct current (DC) current drivers, because the devices have been fabricated with three separate contacts on the (minimum number of) three grating sections separated by two phase-shifts. The separate current drivers enable independent biasing of the laser sections irrespective of each other. The current through the contact on the section closest to the output facet was also modulated by a RF signal, which was added to the DC component with a bias-T. A high speed photodiode (PD) was used to convert the beating of the two emitted

modes into a RF signal, which was then measured with an electrical spectrum analyzer (ESA) or an oscilloscope. A high frequency electrical local oscillator (LO) was used to down-shift the RF signal in frequency to ranges suitable for the available measurement instruments.

Each LD was first characterized optically by scanning the bias currents of each section and by determining the domains where the LDs emitted in dual mode. The optical measurements indicated what was the mode balance between the main modes, what was the SMSR with respect to the other modes, and what was the approximate frequency difference between the two emitted modes. It was also determined how much the mode frequencies changed with varying bias conditions. Consequently, the stability of the dual-mode operation was assessed and the achievable difference frequency was mapped across the dual-mode operation domains. It was observed that there is a significant variance of the characteristics between nominally similar devices. This is attributed to the incontrollable phase of the facet reflections and to the fabrication inaccuracies and resulting random defects in the grating. From measuring over the dual-mode operation domains for the same device with and without AR coatings on the facets it was determined that the magnitude of the facet reflectivities does not affect the stable dual frequency emission domain drastically. This indicates that the devices are resilient to the facet reflection phase variation. It should be specified that the stable dual mode domain does change when AR facet coating is applied, but the resulting behavior resembles that of the uncoated device.

Measured bias-induced difference frequency variations and main mode balance variations over the dual-mode operation domain are shown in Figure 3.3. The derivative of $\Delta\nu$ with respect to front section current variation and the difference frequency ($\Delta\nu$) tuning range increase when changing from unapodized gratings and AR-coated facets (panel A) to linearly apodized gratings and as-cleaved facets (panel B) and then to linearly apodized gratings and AR-coated facets (panel C). For the linearly apodized grating the derivative of the difference frequency with respect to the middle section current variation decreases when AR coatings are applied, making the difference frequency less sensitive to middle section bias variations. Panels D–F show the power difference between the two emitted modes in dB, indicating that,
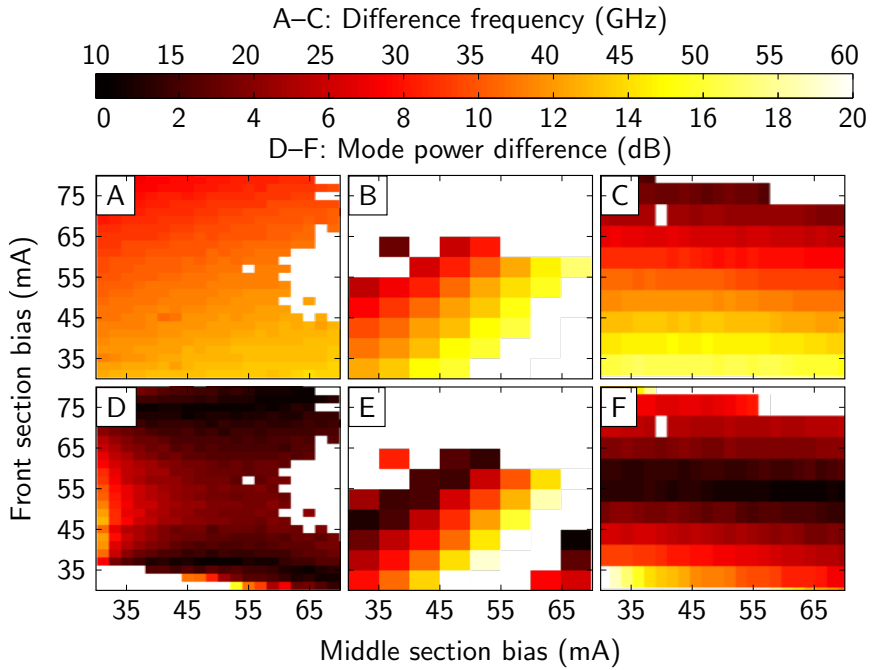
Figure 3.3 *Measured difference frequency (panels A–C) and mode power differ-ence between the two main emitted modes (panels D–F) as a function of front and middle section currents for a 3-section (P = 2) DFB LDs with LC-RWG surface gratings having $M = 818$ and $\kappa \approx 9.5\,\mathrm{cm}^{-1}$. Panels A and D correspond to a LD with AR-coated facets and an un-apodized grating, panels B and E correspond to a LD with as-cleaved facets and a linearly apodized grating, and panel C and F correspond to the LD with a linearly apodized grating after applying AR coatings to the facets. Adapted from [IV].*

additionally, the linearly apodized grating combined with AR facet coating induce a better power balance for a broader range of front section bias cur-rent variation. The sensitivity of mode power balance with respect to middle section current is also reduced by employing AR facet coatings to the devices with linearly apodized gratings.

An important aspect revealed by Figure 3.3 is that the difference frequency and mode balance behave similarly, so that the front section bias can be used to tune the difference frequency over a broad range while keeping a

relatively good mode balance. The fact that the mode balance varies in a logarithmic scale suggests that the power of the generated MMW signal is more sensitive to current and other operation variations than the difference frequency. However, the efficiency of the difference frequency generation is not only a function of the intensities of the two modes, as discussed in section 2.4.1, and the coherence of the two laser modes is also important for the efficiency. Although the applied AR coating deforms the operation domain of the apodized LD, the before and after AR coating operation still resemble each other. This indicates that the surface gratings work even in the presence of moderate feedback from the facets. It was determined that this results from the imaginary part of κ [100], and that the effect can be exploited for reducing the linewidth of the MMW signal generated by beating the two modes against each other [IV].

3.2.1   Modulation of dual frequency lasers

The direct modulation characteristics of the DFLs lasers were also studied. The existence of the two modes inside the laser cavity affects the direct amplitude modulation (AM) response by inducing a photon-photon resonance at the difference frequency between the modes. The bias modulation can also be used to modulate the difference frequency between the emitted modes and, accordingly, the frequency of the RF mode-beating signal. The results obtained studying these two effects are presented in the following.

Direct AM modulation

When the DFLs lase in dual-mode, it is possible to use the existence of the second mode as an internal modulator of the photon density integral over the laser cavity. Measured small signal modulation responses for different mode power balances in dual-mode emission are shown in the left panel of Figure 3.4. The modulation bandwidth can be increased substantially when the device is biased correctly, *i.e.* when the difference frequency properly places the PPR with respect to the CPR frequency and when the second mode does not cause too much photon density integral modulation in the cavity,

resulting in a relatively flat small-signal modulation response. In the extreme case when the two modes in the cavity are close to balance, they cause a large modulation to the photon density integral, resulting in a strong PPR peak, which affects the large-signal AM bandwidth, reducing the eye diagram opening at high frequencies beyond the CPR frequency. The large-signal AM is affected also when the CPR is damped or placed far away from the PPR peak or both, leading to big small-signal AM response variations with the modulation frequency and to reduced eye diagram openings. A similar effect
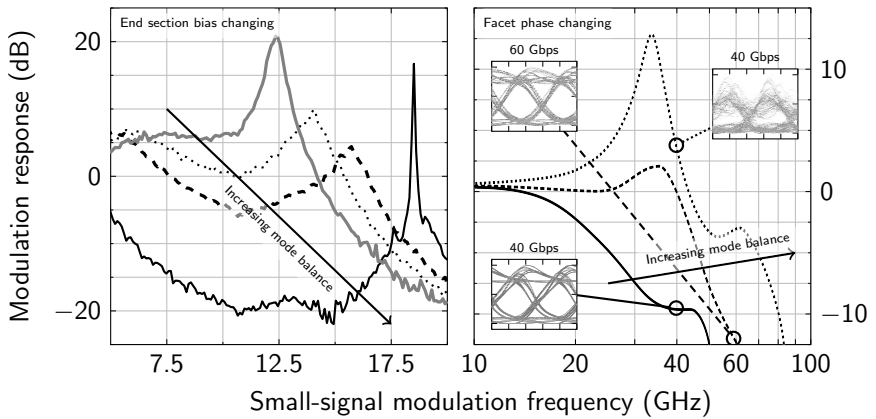
Figure 3.4 *Amplitude modulation (AM) responses for different mode balance conditions. The left panel shows measured small-signal AM responses when the DC bias current in the end section next to the output facet of a DFB laser with 3 grating sections is varied. The right panel shows simulated small-signal AM responses of a DFB laser with 3 grating sections when the phase of the reflection from the front facet is changed, which affects the strength of the PPR effect. The facet reflection phase change is largely equivalent with changing the front section bias. The insets in the right panel show the large-signal eye diagrams at the indicated modulation frequencies. Adapted from [III].*

was simulated with time domain travelling wave (TDTW) software [69] and the resulting variation of the small-signal AM response is shown in the right panel of Figure 3.4 for comparison. The large-signal AM response is affected by the flatness of the small-signal AM response, as illustrated in the insets of the right panel of Figure 3.4, which present the simulated large-signal eye diagrams corresponding to the small-signal AM responses shown in the panel [III].

Direct modulation of the difference frequency

In addition to AM, there is always some amount of chirp or frequency modulation associated with it in direct modulation [146]. The chirp effect can be exploited for difference frequency modulation in the DFLs. A variation applied to the bias of one of the LD sections induces chirp in the mode frequencies, but, because of the device structure, the two modes experience a different amount of chirp, which leads to a difference frequency variation. Therefore, when the bias of one of the LD sections is modulated, the difference frequency between the two modes is modulated accordingly. This is illustrated in Figure 3.5 by the spectrograms of the photodetected mode-beating signal obtained for different bias modulation frequencies when the modulation signal is a sinusoidal.
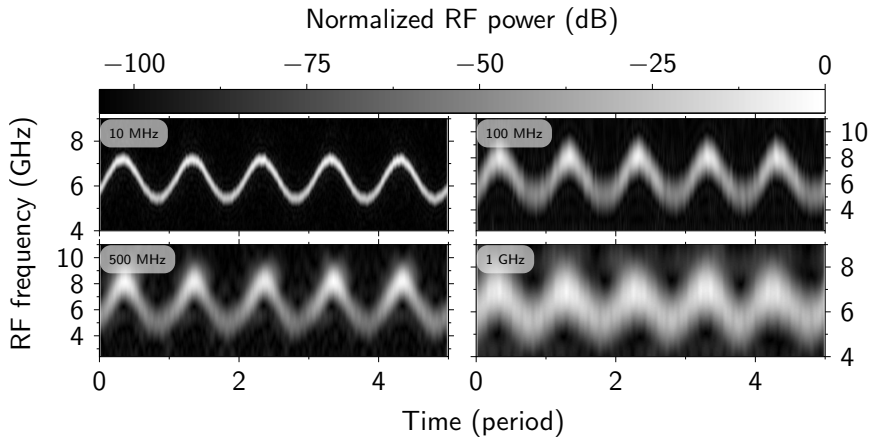
Figure 3.5 *Spectrograms of windowed Fourier transform for the difference frequency signal sinusoidally modulated with four different modulation frequencies. The frequency resolution suffers at higher modulation frequencies because there are less samples in the Fourier transform window due to the limited sampling rate of the oscilloscope. Adapted from [III].*

Even though the spectrograms give good indication of the spectral purity, modulation depth, and of how resolvable the beat signal is, it is difficult to generate them in real time and they require expensive high frequency oscilloscopes. Figure 3.6 shows the frequency domain spectra of the pho-

todetected beat signals, measured with an ESA. The modulation depth of the frequency modulation (FM) signal varies with the modulation frequency, which may be due to the unoptimized impedance matching of the bonded LD [119], [147] and to the large active area of the device [148].
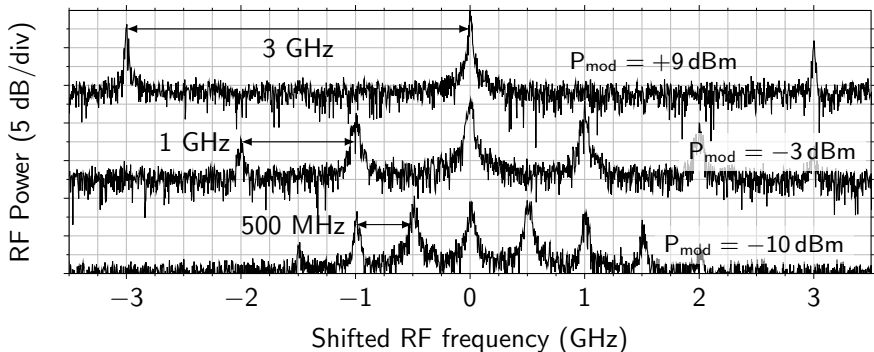

Figure 3.6 *RF spectra of the difference frequency beat signal generated by sinusoidally modulating the front section bias of the DFL at 0.5, 1 and 3 GHz. The side lobe spacing is the same as the modulation frequency, indicating that the signal is frequency modulated. Adapted from [III].*

Even though the time domain signal is difficult to obtain, it can be used to obtain the instantaneous frequency of the signal, which can be regarded as the demodulated FM signal. Numerically the demodulation procedure includes first applying a band pass filter to the measured signal to reduce the noise resulting from the frequency components far away from the carrier frequency, which is at the frequency of the down-converted MMW signal without modulation. The width of the band-pass filter is determined by the modulation frequency and modulation depth, *i.e.* how many side bands are desired in the demodulation. The second step is to make a Hilbert transform from which the instantaneous frequency (and amplitude) of the signal are obtained [149]. In principle this procedure corresponds to FM-AM demodulation. In Figure 3.7 the results of this demodulation step are shown as pseudo eye diagrams, AM in the left panels and FM in the right ones. From the shape of the eye it is clear that the modulating sinusoidal signal has been deformed, which is in accordance to the small signal modulation response shown in Figure 3.4 for a strong PPR. The behavior of $\Delta\nu$ is also not completely linear as was indicated by the bias maps in Figure 3.3,
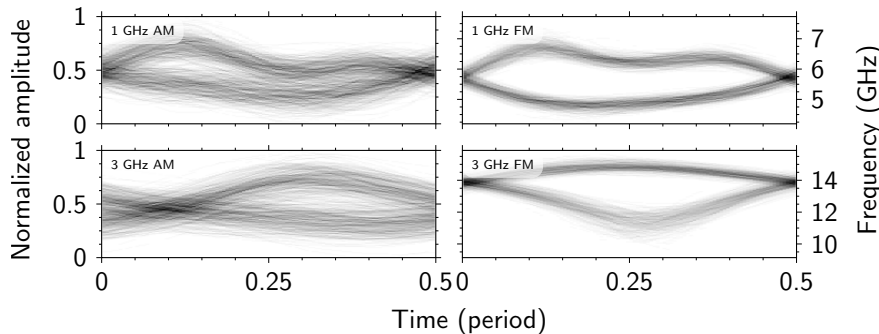
Figure   3.7 *Amplitude and frequency modulation eye diagrams generated from measured time series signals from DFL DFB lasers with 3 grating sections. The sinusoidal modulation signal was applied to the section closest to the laser output facet. Adapted from [III].*

which can result in the deformation of the demodulated signal. This effect was also confirmed by perturbed TMM simulations, which indicate how the eye shapes in Figure 3.7 are obtained [III]. On the bright side, the FM eye diagram suffers a lot less from jitter than the AM eye diagram. It should be noted that the measurements exclude the original amplitude modulation band, because the signals have been down-shifted in frequency in order to be able to record them with an oscilloscope, and the modulation signal that is demodulated is contained entirely in the generated MMW band. This means that the AM signal is in the difference frequency signal and related to the mode balance between the two emitted modes and their mutual coherence and correlation. The explanation for the higher AM jitter is evident from Figure 3.3: while the difference frequency changes are represented in a linear scale, the power balance, and the resulting generated MMW signal power, changes in a logarithmic scale.

When considering the practical implementation of a FM-AM demodulator, the available bandwidths are typically low. There are also photonic solutions for instantaneous frequency measurement with high bandwidths [150], but the error can increase with increasing bandwidth [151], which leads to problems in a practical demodulation. This is increasingly problematic when targeting higher frequency bands, *e.g.* 100 GHz and beyond.

3.2.2 Difference frequency linewidth

As discussed in section 2.3, the AM bandwidth and $\Delta\nu$ of SFL LDs are contradictory design targets. In the previous discussion the AM modulation response of the studied DFLs was demonstrated to be enhanced when the PPR effect is tuned appropriately. When the PPR effect was the strongest, the AM eye diagrams and the MMW signal FM eye diagrams were distorted.

The generated MMW signal could also be exploited as an RF LO, *e.g.* distributable over fiber for the next generation wireless communication methods. For this application the stability of the MMW signal is of interest, and, consequently, it was measured for the studied DFL lasers.
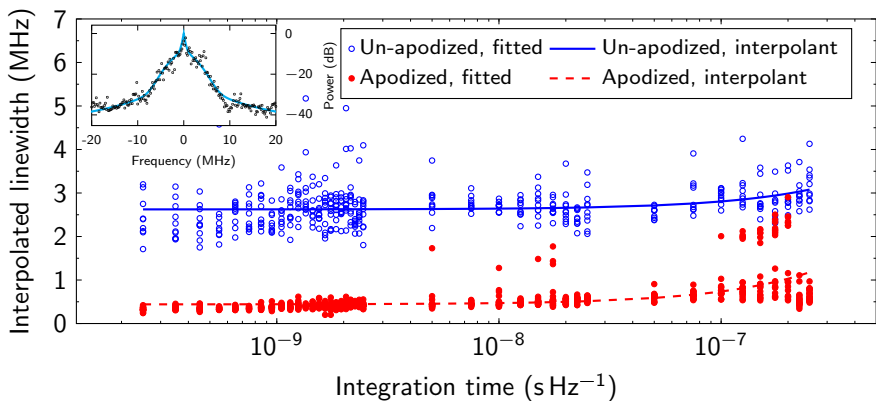
Figure 3.8 *FWHM linewidth of the Lorentzian component of the MMW signal as a function of ESA integration time, when fitted with an unconstrained Voigt lineshape, as illustrated in the inset. The measured un-apodized and apodized DFLs are the ones measured for the results given in the panels A/D and B/E of Figure 3.3, respectively. Adapted from [IV].*

The linewidth FWHM of the Lorentzian component of the MMW signal ($\Delta\nu_{\mathrm{FWHM}}$) was determined with varying integration times for the devices measured for the results given in panels A/D and B/E of Figure 3.3, respectively, and the FWHM values of the linewidth were in the MHz range and below, as shown in Figure 3.8. The inset of the figure shows the lineshape fitted to an unconstrained Voigt profile, for which the ratio between the Lorentzian and Gaussian components is not fixed. The unconstrained

Voigt profile lineshape was empirically determined to yield better fits than either Lorentzian or normal Voigt profiles. The reason for this uncommon lineshape was that the variation of the peak frequency of the MMW signal is resulting from the frequency variations of both the emitted modes, and not from the variation of a single frequency with respect to a stable LO as in the case of a typical heterodyne measurement. The variance of the difference frequency during the integration time can contribute significantly to the measured lineshape, deforming it to be dissimilar from the typical Lorentzian or Voigt lineshapes. When the integration times were short, the DFL with linearly apodized grating and as-cleaved facets achieved linewidths in the below MHz range, narrower than the linewidths achieved by DFL with un-apodized gratings and AR coated facets, whose linewidth FWHM values were below 3 MHz. When the integration time increases, the difference between the evaluated linewidths reduces slightly, which was also related to the difference frequency variation and its effect on the lineshape. The long term variation in the difference frequency for a similar device as the ones presented here under similar measurement conditions has been measured as approximately 0.2 % of the difference frequency. This corresponds to 60 MHz for a 30 GHz difference frequency, which is much larger than the measured linewidths. In principle, longer integration times could increase the noise contribution to the power spectral density, leading to broader linewidths. However, as long as the intrinsic short time scale linewidth of the DFLs can be made narrow, it can also be kept narrow for a longer time period when the difference frequency variation is locked.

The calculated κL for the linearly apodized grating (using an averaged κ) was approximately 1.44, smaller than the 1.71 κL values for the un-apodized grating. Due to this, the narrower linewidth in the apodized DFL with as-cleaved facets is attributable to the higher facet reflectivities. The narrower linewidth is derived mainly from the longer photon lifetime inside the laser cavity. The linewidth of the apodized DFL was also measured after applying AR coatings to its facets, and the measured linewidth increased to above 10 MHz. Thus it can be said that the facet reflectivity played a major role in increasing the photon lifetime in the cavity, which was evaluated from the variation of the measured linewidth. The surface gratings are a suitable choice in narrowing the intrinsic linewidth by higher facet feedback, since

they maintain grating-determined operation even for a relatively high facet reflectivity that may not be phase-matched with the grating.

The presented results point out possible ways for exploiting the DFLs in demanding next generation optical and RF communication systems.

4.   CONCLUSIONS

The work in this thesis combines theoretical studies of LC-RWG DFB and ET-RWG surface gratings, transverse and longitudinal structure modeling, simulation and design, and characterization of fabricated structures targeting single or dual-frequency operation characteristics required by the envisioned applications.

The design procedures developed and applied to achieve the results reported in the thesis enable fast sweeps of large ranges of variations for different structural parameters, because the calculation procedures use many simplifications, but avoid generating high errors. The methods for establishing structural parameters for STM operation and for calculating the grating coupling coefficient for LC-RWG and ET-RWG surface gratings were compared against experimental results and against the results from a rigorous semi-analytical method [107], and the errors were found to be small. The described methodology was successfully applied to device design and the fabricated devices showed characteristics that corresponded to the design targets, further confirming the model validity. A numerical method and an analytical approximate method were also applied in the design of the longitudinal DFB grating for dual frequency generation. Both methods were simple to use and computationally inexpensive, and proved successful in predicting the output characteristics of the fabricated DFLs, even though facet effects had been neglected in the design procedure. The lightweight nature of the used methods proved invaluable, because large parametric sweeps with self consistent methods [87] are computationally taxing and all the obtained information may not be required to make the correct design decisions.

The novel 1$^{\text{st}}$ order alternating LC-RWG grating scheme circumvented the

etching aspect ratio limitation and enabled the fabrication of low order short wavelength surface gratings using NIL. These fabricated SFL LDs were compared against conventional 3rd order LC-RWG gratings with symmetrically place teeth, and the threshold current densities were decreased from an average of $1900\,\mathrm{A\,cm^{-2}}$ to an average of $1300\,\mathrm{A\,cm^{-2}}$, the maximum output power from one facet was increased from approximately 30 to 40 mW, the maximum PCE per facet increased from 4.9 to 6.8 %, and the maximum slope efficiency per facet increased from 3×10^{-3} to $5 \times 10^{-3}\,\mathrm{W\,A^{-1}}$. The achieved relatively high powers are similar to [152], but for example recessed surface gratings have been used to achieve better slope efficiencies [49] and high order surface grating broad area devices have been realized to achieve high conversion efficienices [108]. On the other hand, the SFLs of this thesis show extremely narrow spectral linewidths in the order of 10 kHz [32] and the power-linewidth product is much lower, in the range of $0.15–0.3\,\mathrm{mW \cdot MHz}$, than what has been reported for buried gratings at the same wavelength [118], [153], and other LC RWG DFB lasers show much broader linewidths, albeit their device lengths and coupling strengths are not reported [152]. This indicates that the LC-RWG DFB LDs of this work are a promising candidate for atomic clock and spectroscopy applications.

Modeling and simulation studies were carried out for DFLs and easy to use design guidelines have been derived for controlling the difference frequency range, the balance of the main two modes, and the SMSR with respect to the other modes. It was demonstrated that DFLs employing surface gratings and apodized gratings are more tolerant against facet reflections, with narrower short time scale linewidth and higher yield. Yield improvements with higher facet reflectivities are typical in single mode LDs with gain coupling [100], but the effect was demonstrated for the first time for dual frequency LC-RWG DFB grating based LDs within this work. The imaginary coupling of surface gratings has been reported earlier [105].

The modulation properties of the studied DFLs were also studied, with varying presence of the second frequency. It was confirmed that the high frequency direct AM bandwidth can be increased when compared to the situation where only one frequency is emitted. AM bandwidth increase from 9 to 16 GHz was demonstrated between devices with the grating supporting

only one mode and two modes, respectively. The effect was demonstrated also in other simulations [69], [154] and experimental studies [155], where usually the feedback phase was the main tuning mechanism of the PPR strength. Because the studied DFLs had relatively low relaxation frequency, the modulation bandwidth extension was partly limited by that and a flat modulation response was not achieved. Direct difference frequency modulation of the DFLs in the strong mode-beat domain was also studied. FM signals resulting from that direct modulation were measured and analyzed up to 3 GHz modulation frequency. The amplitude jitter of the modulated MMW band signal turned out to be much higher than the frequency jitter, but the detection was determined to be an issue with the MMW FM signals.

It was determined that the gratings whose coupling coefficient was linearly apodized yielded an increased tunability of the difference between the two emitted frequencies. The linearly apodized LC-RWG surface gratings increased the available emitted mode difference frequency tuning range from 19 to 40 GHz in the frequency ranges around 28 GHz. This leads to the possibility of using the developed DFL design procedure for realizing DFLs that cover the frequency ranges of multiple bands in 5G or other upcoming wireless communication technologies, opening a way to reduce the device inventory and thus the total system cost. There are also other approaches that can generate tunable frequency spacing in dual mode emission with a broad frequency tuning range, but the schemes are usually more complex [78], [156]–[162]. An important benefit for DFLs identified in this thesis was the capability to decrease the intrinsic linewidth of the generated MMW signal, without affecting the device yield, by having higher facet reflectivities, which was enabled by using surface gratings and grating apodization.

The future development directions of the presented lasers include increasing the power levels of the narrow linewidth SFLs by implementing a MOPA structure and applying the higher power in spectroscopy or atomic clock experiments. The DFLs are suitable candidates for extremely high frequency signal generation for 5G (or other next generation wireless radio frequency communication) applications. Integrating the laser chips into silicon photonics designs could lead to simpler structures, lower power consumption, higher bandwidth and lower latencies for the next generation networks.

REFERENCES

[1] C. H. Townes, "Obituary: Theodore H. Maiman (1927–2007)", *Nature*, vol. 447, no. 7145, p. 654, Jun. 2007, ISSN: 1476-4687. DOI: `10.1038/447654a`.

[2] O. Svelto, *Principles of Lasers*, 5th ed. Springer, Dec. 2009, ISBN: 1-4419-1301-7.

[3] E. Akman, A. Demir, T. Canel, and T. Sınmazçelik, "Laser welding of ti6al4v titanium alloys", *Journal of Materials Processing Technology*, vol. 209, no. 8, pp. 3705–3713, Apr. 2009, ISSN: 0924-0136. DOI: `10.1016/j.jmatprotec.2008.08.026`.

[4] C. Gohle, B. Stein, A. Schliesser, T. Udem, and T. W. Hänsch, "Frequency comb vernier spectroscopy for broadband, high-resolution, high-sensitivity absorption and dispersion spectra", *Physical Review Letters*, vol. 99, no. 26, p. 263 902, Dec. 2007. DOI: `10.1103/PhysRevLett.99.263902`.

[5] S. Dimopoulos, P. W. Graham, J. M. Hogan, M. A. Kasevich, and S. Rajendran, "Atomic gravitational wave interferometric sensor", *Physical Review D*, vol. 78, no. 12, p. 122 002, Dec. 2008. DOI: `10.1103/PhysRevD.78.122002`.

[6] T. Kessler, C. Hagemann, C. Grebing, T. Legero, U. Sterr, F. Riehle, M. J. Martin, L. Chen, and J. Ye, "A sub-40-mhz-linewidth laser based on a silicon single-crystal optical cavity", *Nature Photonics*, vol. 6, no. 10, pp. 687–692, Oct. 2012, ISSN: 1749-4893. DOI: `10.1038/nphoton.2012.217`.

[7] D. F. McDonough, J. A. Taylor, A. D. Pillsbury, D. P. Verly, and E. S. Kintzer, "A space-qualified transmitter system for heterodyne optical communications", *Lincoln Laboratory Journal*, vol. 3, pp. 245–272, 1990, ISSN: 0896-4130.

[8] M. N. Ott, D. B. Coyle, J. S. Canham, and H. W. Leidecker, "Qualification and issues with space flight laser systems and components",

in *Solid State Lasers XV: Technology and Devices*. International Society for Optics and Photonics, Feb. 2006, vol. 6100, p. 61001V. DOI: `10.1117/12.674042`.

[9]   C. Doerr, J. Heanue, L. Chen, R. Aroca, S. Azemati, G. Ali, G. McBrien, L. Chen, B. Guan, H. Zhang, and et al., "Silicon photonics coherent transceiver in a ball-grid array package", in *2017 Optical Fiber Communications Conference and Exhibition (OFC)*. Mar. 2017, pp. 1–3.

[10]   D. J. Blumenthal, J. Barton, N. Beheshti, J. E. Bowers, E. Burmeister, L. A. Coldren, M. Dummer, G. Epps, A. Fang, Y. Ganjali, and et al., "Integrated photonics for low-power packet networking", *IEEE Journal of Selected Topics in Quantum Electronics*, vol. 17, no. 2, pp. 458–471, Mar. 2011, ISSN: 1077-260X. DOI: `10.1109/JSTQE.2010.2077673`.

[11]   J.-i. Nishizawa, "Extension of frequencies from maser to laser", *Proceedings of the Japan Academy. Series B, Physical and Biological Sciences*, vol. 85, no. 10, pp. 454–465, Dec. 2009, ISSN: 0386-2208. DOI: `10.2183/pjab.85.454`.

[12]   X. Liu, M. H. Hu, C. G. Caneau, R. Bhat, and C.-E. Zah, "Thermal management strategies for high power semiconductor pump lasers", *IEEE Transactions on Components and Packaging Technologies*, vol. 29, no. 2, pp. 268–276, Jun. 2006, ISSN: 1521-3331. DOI: `10.1109/TCAPT.2006.875878`.

[13]   T. Lévèque, L. Antoni-Micollier, B. Faure, and J. Berthon, "A laser setup for rubidium cooling dedicated to space applications", *Applied Physics B*, vol. 116, no. 4, pp. 997–1004, Sep. 2014, ISSN: 0946-2171, 1432-0649. DOI: `10.1007/s00340-014-5788-z`.

[14]   L. Ricci, M. Weidemüller, T. Esslinger, A. Hemmerich, C. Zimmermann, V. Vuletic, W. König, and T. W. Hänsch, "A compact grating-stabilized diode laser system for atomic physics", *Optics Communications*, vol. 117, no. 5, pp. 541–549, Jun. 1995, ISSN: 0030-4018. DOI: `10.1016/0030-4018(95)00146-Y`.

[15] K. Utaka, S. Akiba, K. Sakai, and Y. Matsushima, "Room-temperature cw operation of distributed-feedback buried-heterostructure ingaasp/inp lasers emitting at 1.57 µm", *Electronics Letters*, vol. 17, no. 25, pp. 961–963, Dec. 1981, ISSN: 0013-5194. DOI: `10.1049/el:19810672`.

[16] P. J. A. Thijs, T. v. Dongen, L. F. Tiemeijer, and J. J. M. Binsma, "High-performance λ=1.3 µm InGaAsP-InP strained-layer quantum well lasers", *Journal of Lightwave Technology*, vol. 12, no. 1, pp. 28–37, Jan. 1994, ISSN: 0733-8724. DOI: `10.1109/50.265731`.

[17] T. Takeshita, T. Sato, M. Mitsuhara, R. Yoshimura, and H. Ishii, "Long-term degradation behavior of 2.3-µm wavelength highly strained inas/inp mqw-dfb lasers with a p-/n-inp buried heterostructure", *IEEE Transactions on Electron Devices*, vol. 59, no. 4, pp. 1056–1062, Apr. 2012, ISSN: 0018-9383. DOI: `10.1109/TED.2011.2181176`.

[18] L. Lu, B. Cao, L. Zhang, S. Tang, L. Li, S. Li, Y. Shi, and X. Chen, "Experimental demonstration of the three-phase-shifted dfb semiconductor laser with buried heterostructure using common holographic exposure", *Science China Technological Sciences*, vol. 57, no. 11, pp. 2231–2235, Nov. 2014, ISSN: 1674-7321, 1869-1900. DOI: `10.1007/s11431-014-5659-1`.

[19] J. Viheriälä, T. Niemi, J. Kontio, and M. Pessa, "Nanoimprint lithography - next generation nanopatterning methods for nanophotonics fabrication", *Recent Optical and Photonic Technologies*, 2010. DOI: `10.5772/6917`.

[20] J. Beas, G. Castanon, I. Aldaya, A. Aragon-Zavala, and G. Campuzano, "Millimeter-wave frequency radio over fiber systems: A survey", *IEEE Communications Surveys Tutorials*, vol. 15, no. 4, pp. 1593–1619, 2013, ISSN: 1553-877X. DOI: `10.1109/SURV.2013.013013.00135`.

[21] A. Davis, M. Pettitt, J. King, and S. Wright, "Phase diversity techniques for coherent optical receivers", *Journal of Lightwave Technology*, vol. 5, no. 4, pp. 561–572, Apr. 1987, ISSN: 0733-8724. DOI: `10.1109/JLT.1987.1075539`.

[22]   J. M. Tang and K. A. Shore, "30-Gb/s signal transmission over 40-km directly modulated dfb-laser-based single-mode-fiber links without optical amplification and dispersion compensation", *Journal of Lightwave Technology*, vol. 24, no. 6, pp. 2318–2327, Jun. 2006, ISSN: 0733-8724. DOI: 10.1109/JLT.2006.874557.

[23]   G. H. Smith, D. Novak, and Z. Ahmed, "Overcoming chromatic-dispersion effects in fiber-wireless systems incorporating external modulators", *IEEE Transactions on Microwave Theory and Techniques*, vol. 45, no. 8, pp. 1410–1415, Aug. 1997, ISSN: 0018-9480. DOI: 10.1109/22.618444.

[24]   J. Vanier and C. Mandache, "The passive optically pumped Rb frequency standard: The laser approach", *Applied Physics B*, vol. 87, no. 4, pp. 565–593, Jun. 2007, ISSN: 0946-2171, 1432-0649. DOI: 10.1007/s00340-007-2643-5.

[25]   M. Hashimoto and M. Ohtsu, "Experiments on a semiconductor laser pumped rubidium atomic clock", *IEEE Journal of Quantum Electronics*, vol. 23, no. 4, pp. 446–451, Apr. 1987, ISSN: 0018-9197. DOI: 10.1109/JQE.1987.1073368.

[26]   S. S. Sané, S. Bennetts, J. E. Debs, C. C. N. Kuhn, G. D. McDonald, P. A. Altin, J. D. Close, and N. P. Robins, "11 W narrow linewidth laser source at 780 nm for laser cooling and manipulation of rubidium", *Optics Express*, vol. 20, no. 8, pp. 8915–8919, Apr. 2012, ISSN: 1094-4087. DOI: 10.1364/OE.20.008915.

[27]   R. Farjad-Rad, W. Dally, H.-T. Ng, R. Senthinathan, M. J. E. Lee, R. Rathi, and J. Poulton, "A low-power multiplying DLL for low-jitter multigigahertz clock generation in highly integrated digital chips", *IEEE Journal of Solid-State Circuits*, vol. 37, no. 12, pp. 1804–1812, Dec. 2002, ISSN: 0018-9200. DOI: 10.1109/JSSC.2002.804340.

[28]   F. L. Walls and A. Demarchi, "RF spectrum of a signal after frequency multiplication; measurement and comparison with a simple calculation", *IEEE Transactions on Instrumentation and Measurement*, vol. 24, no. 3, pp. 210–217, Sep. 1975, ISSN: 0018-9456. DOI: 10.1109/TIM.1975.4314411.

[29] C. M. Armstrong, "The truth about terahertz", *IEEE Spectrum*, vol. 49, no. 9, pp. 36–41, Sep. 2012, ISSN: 0018-9235. DOI: `10.1109/MSPEC.2012.6281131`.

[30] S. E. Alavi, M. R. K. Soltanian, I. S. Amiri, M. Khalily, A. S. M. Supa'at, and H. Ahmad, "Towards 5g: A photonic based millimeter wave signal generation for applying in 5g access fronthaul", *Scientific Reports*, vol. 6, srep19891, Jan. 2016, ISSN: 2045-2322. DOI: `10.1038/srep19891`.

[31] L. A. Coldren, S. W. Corzine, and M. L. Mashanovitch, *Diode Lasers and Photonic Integrated Circuits*. John Wiley & Sons, Mar. 2012, Google-Books-ID: D6Ub126rtPoC, ISBN: 978-1-118-14817-4.

[32] H. Virtanen, T. Uusitalo, M. Karjalainen, S. Ranta, J. Viheriälä, and M. Dumitrescu, "Narrow-linewidth 780-nm DFB lasers fabricated using nanoimprint lithography", *IEEE Photonics Technology Letters*, vol. 30, no. 1, pp. 51–54, Jan. 2018, ISSN: 1041-1135. DOI: `10.1109/LPT.2017.2772337`.

[33] T. Mukaihara, H. Nasu, T. Kimoto, S. Tamura, T. Nomura, T. Shinagawa, A. Kasukawa, M. Oike, H. Matsuura, T. Shiba, and et al., "Highly reliable 40 mW, 25 GHz × 20 ch thermally tunable DFB laser module integrated with wavelength monitor", in *2002 28TH European Conference on Optical Communication*. Sep. 2002, vol. 3, pp. 1–2.

[34] M. Lackner, "Tunable diode laser absorption spectroscopy (TDLAS) in the process industries – a review", *Reviews in Chemical Engineering*, vol. 23, no. 2, pp. 65–147, 2011, ISSN: 2191-0235. DOI: `10.1515/REVCE.2007.23.2.65`.

[35] M. Oberg, S. Nilsson, T. Klinga, and P. Ojala, "A three-electrode distributed bragg reflector laser with 22 nm wavelength tuning range", *IEEE Photonics Technology Letters*, vol. 3, no. 4, pp. 299–301, Apr. 1991, ISSN: 1041-1135. DOI: `10.1109/68.82092`.

[36] W. Streifer, D. Scifres, and R. Burnham, "Coupling coefficients for distributed feedback single- and double-heterostructure diode lasers", *IEEE Journal of Quantum Electronics*, vol. 11, no. 11, pp. 867–873, Nov. 1975, ISSN: 0018-9197. DOI: `10.1109/JQE.1975.1068539`.

[37] S. Arahira, Y. Matsui, T. Kunii, S. Oshiba, and Y. Ogawa, "Transform-limited optical short-pulse generation at high repetition rate over 40 GHz from a monolithic passive mode-locked DBR laser diode", *IEEE Photonics Technology Letters*, vol. 5, no. 12, pp. 1362–1365, Dec. 1993, ISSN: 1041-1135. DOI: `10.1109/68.262541`.

[38] M. Vilera Suárez, M. Krakowski, Y. Robert, E. Vinet, P. Primiani, J. P. Le Goëc, O. Parillaud, F. van Dijk, M. Vilera, and A. Consoli Barone, "Monolithic master oscillator power amplifier at 1.58 μm for lidar measurements", in *International Conference on Space Optics (ICSO 2014)*. E.T.S.I. Telecomunicación (UPM), 2014, pp. 1–8.

[39] J. Piprek, *Handbook of Optoelectronic Device Modeling and Simulation: Fundamentals, Materials, Nanostructures, LEDs, and Amplifiers*. CRC Press, Oct. 2017, Google-Books-ID: LmpQDwAAQBAJ, ISBN: 978-1-4987-4947-3.

[40] L. Li, L. Lu, S. Li, R. Guo, Y. Shi, and X. Chen, "Phase-shifted distributed feedback laser with linearly chirped grating fabricated by reconstruction equivalent chirp technique", *Optics & Laser Technology*, vol. 61, pp. 57–61, 2014. DOI: `10.1016/j.optlastec.2014.02.008`.

[41] J. Zheng, N. Song, Y. Zhang, Y. Shi, S. Tang, L. Li, R. Guo, and X. Chen, "An equivalent-asymmetric coupling coefficient DFB laser with high output efficiency and stable single longitudinal mode operation", *IEEE Photonics Journal*, vol. 6, no. 6, pp. 1–9, 2014. DOI: `10.1109/JPHOT.2014.2368776`.

[42] X. Han, Q. Cheng, F. Liu, and Y. Yu, "Numerical analysis on thermal tuning efficiency and thermal stress of a thermally tunable SG-DBR laser", *IEEE Photonics Journal*, vol. 8, no. 3, pp. 1–12, 2016. DOI: `10.1109/JPHOT.2016.2558042`.

[43] M. Tawfieq, H. Wenzel, O. Brox, P. Della Casa, B. Sumpf, and G. Tränkle, "Concept and numerical simulations of a widely tunable GaAs-based sampled-grating diode laser emitting at 976 nm", *IET Optoelectronics*, vol. 11, no. 2, pp. 73–78, 2017. DOI: `10.1049/iet-opt.2016.0068`.

[44] K. Dridi, A. Benhsaien, J. Zhang, K. Hinzer, and T. J. Hall, "Narrow linewidth two-electrode 1560 nm laterally coupled distributed feedback lasers with third-order surface etched gratings", *Optics express*, vol. 22, no. 16, pp. 19 087–19 097, 2014. DOI: `10.1364/OE.22.019087`.

[45] R. Liang, T. Hosoda, L. Shterengas, A. Stein, M. Lu, G. Kipshidze, and G. Belenky, "Distributed feedback 3.27 µm diode lasers with continuous-wave output power above 15 mW at room temperature", *Electronics Letters*, vol. 50, no. 19, pp. 1378–1380, 2014. DOI: `10.1049/el.2014.2733`.

[46] S. Najda, T. Slight, P. Perlin, O. Odedina, T. Suski, L. Marona, S. Stanczyk, M. Leszczyński, P. Wisniewski, R. Czernecki, *et al.*, "Lateral grating DFB AlGaInN laser diodes for optical communications and atomic clocks.", in *Journal of Physics: Conference Series*, IOP Publishing, vol. 810, 2017, p. 012 053. DOI: `10.1088/1742-6596/810/1/012053`.

[47] K. Dridi, A. Benhsaien, J. Zhang, and T. J. Hall, "Narrow linewidth 1550 nm corrugated ridge waveguide DFB lasers", *IEEE Photonics Technology Letters*, vol. 26, no. 12, pp. 1192–1195, 2014. DOI: `10.1109/LPT.2014.2318593`.

[48] P. Zhang, Q. Lu, and W. Guo, "Low threshold single-mode 780 nm surface grating DFB lasers for atomic clocks", in *Asia Communications and Photonics Conference (2017), paper Su2A.111*. Optical Society of America, Nov. 2017, Su2A.111. DOI: `10.1364/ACPC.2017.Su2A.111`.

[49] R. D. Martin, S. Forouhar, S. Keo, R. J. Lang, R. G. Hunsperger, R. C. Tiberio, and P. F. Chapman, "CW performance of an InGaAs-GaAs-AlGaAs laterally-coupled distributed feedback (LC-DFB) ridge laser diode", *IEEE Photonics Technology Letters*, vol. 7, no. 3, pp. 244–246, Mar. 1995, ISSN: 1041-1135. DOI: `10.1109/68.372734`.

[50] C.-A. Yang, Y. Zhang, Y.-P. Liao, J.-L. Xing, S.-H. Wei, L.-C. Zhang, Y.-Q. Xu, H.-Q. Ni, and Z.-C. Niu, "2-µm single longitudinal mode GaSb-based laterally coupled distributed feedback laser with regrowth-free shallow-etched gratings by interference lithography", *Chinese Physics B*, vol. 25, no. 2, p. 024 204, 2016, ISSN: 1674-1056. DOI: `10.1088/1674-1056/25/2/024204`.

[51]   F. Gruet, A. Al-Samaneh, E. Kroemer, L. Bimboes, D. Miletic, C. Af-
       folderbach, D. Wahl, R. Boudot, G. Mileti, and R. Michalzik, "Metro-
       logical characterization of custom-designed 894.6 nm VCSELs for
       miniature atomic clocks", *Optics Express*, vol. 21, no. 5, pp. 5781–
       5792, Mar. 2013, ISSN: 1094-4087. DOI: 10.1364/OE.21.005781.

[52]   U. Eriksson, J.-O. Wesström, Y. Liu, S. Hammerfeldt, M. Hassler,
       B. Stoltz, N. Carlsson, S. Siraj, E. Goobar, and Y. Matsui, "High
       performance narrow linewidth thermally tuned semiconductor laser",
       in *Optical Communication (ECOC), 2015 European Conference on*,
       IEEE, 2015, pp. 1–3. DOI: 10.1109/ECOC.2015.7341968.

[53]   F. Bello, A. Abdullaev, M. Wallace, M. Nawrocka, Q. Lu, W. Guo,
       and J. F. Donegan, "Traveling wave analysis for a high-order grat-
       ing, partially slotted laser", *IEEE Journal of Quantum Electronics*,
       vol. 51, no. 11, pp. 1–5, 2015. DOI: 10.1109/JQE.2015.2485219.

[54]   W. Wong and H. Ghafouri-Shiraz, "Dynamic model of tapered semi-
       conductor lasers and amplifiers based on transmission-line laser mod-
       eling", *IEEE Journal of selected topics in quantum electronics*, vol. 6,
       no. 4, pp. 585–593, 2000. DOI: 10.1109/2944.883372.

[55]   L. Hou, M. Haji, J. Akbar, and J. H. Marsh, "Narrow linewidth later-
       ally coupled 1.55 μm AlGaInAs/InP distributed feedback lasers inte-
       grated with a curved tapered semiconductor optical amplifier", *Optics
       letters*, vol. 37, no. 21, pp. 4525–4527, 2012. DOI: 10.1364/OL.37.
       004525.

[56]   Y. Chiou and L. Wang, "Effect of optical amplifier noise on laser
       linewidth requirements in long haul optical fiber communication sys-
       tems with Costas PLL receivers", *Journal of Lightwave Technology*,
       vol. 14, no. 10, pp. 2126–2134, Oct. 1996, ISSN: 0733-8724. DOI: 10.
       1109/50.541199.

[57]   M. Seimetz, "Laser linewidth limitations for optical systems with
       high-order modulation employing feed forward digital carrier phase
       estimation", in *OFC/NFOEC 2008 - 2008 Conference on Optical
       Fiber Communication/National Fiber Optic Engineers Conference*.
       Feb. 2008, pp. 1–3. DOI: 10.1109/OFC.2008.4528637.

[58] T. Kan, K. Kasai, M. Yoshida, and M. Nakazawa, "42.3 Tbit/s, 18 Gbaud 64 QAM WDM coherent transmission over 160 km in the C-band using an injection-locked homodyne receiver with a spectral efficiency of 9 bit/s/Hz", *Optics Express*, vol. 25, no. 19, pp. 22 726– 22 737, Sep. 2017, ISSN: 1094-4087. DOI: 10.1364/OE.25.022726.

[59] W. Lewoczko-Adamczyk, C. Pyrlik, J. Häger, S. Schwertfeger, A. Wicht, A. Peters, G. Erbert, and G. Tränkle, "Ultra-narrow linewidth DFB-laser with optical feedback from a monolithic confocal Fabry-Pérot cavity", *Optics Express*, vol. 23, no. 8, pp. 9705–9709, Apr. 2015, ISSN: 1094-4087. DOI: 10.1364/OE.23.009705.

[60] V. Tronciu, H. Wenzel, and H. J. Wünsche, "Instabilities and bifurcations of a DFB laser frequency-stabilized by a high-finesse resonator", *IEEE Journal of Quantum Electronics*, vol. 53, no. 1, pp. 1–9, Feb. 2017, ISSN: 0018-9197. DOI: 10.1109/JQE.2016.2628160.

[61] M. Siltanen, M. Vainio, and L. Halonen, "Pump-tunable continuous-wave singly resonant optical parametric oscillator from 2.5 to 4.4 μm", *Optics Express*, vol. 18, no. 13, pp. 14 087–14 092, Jun. 2010, ISSN: 1094-4087. DOI: 10.1364/OE.18.014087.

[62] S. O'Brien, F. Smyth, K. Shi, J. O'Carroll, P. M. Anandarajah, D. Bitauld, S. Osborne, R. Phelan, B. Kelly, J. O'Gorman, and et al., "Design, characterization, and applications of index-patterned Fabry–Pérot lasers", *IEEE Journal of Selected Topics in Quantum Electronics*, vol. 17, no. 6, pp. 1621–1631, Nov. 2011, ISSN: 1077-260X. DOI: 10.1109/JSTQE.2011.2118192.

[63] K. L. Corwin, Z.-T. Lu, C. F. Hand, R. J. Epstein, and C. E. Wieman, "Frequency-stabilized diode laser with the Zeeman shift in an atomic vapor", *Applied Optics*, vol. 37, no. 15, pp. 3295–3298, May 1998, ISSN: 2155-3165. DOI: 10.1364/AO.37.003295.

[64] J. Li, T. Ning, L. Pei, C. Qi, Q. Zhou, X. Hu, and S. Gao, "60 GHz millimeter-wave generator based on a frequency-quadrupling feed-forward modulation technique", *Optics Letters*, vol. 35, no. 21, pp. 3619–3621, Nov. 2010. DOI: 10.1364/OL.35.003619.

[65] J. Li, T. Ning, L. Pei, and C. Qi, "A bidirectional 60 GHz RoF system based on FWM in a semiconductor optical amplifier", *Optics Communications*, vol. 283, no. 10, pp. 2238–2242, May 2010, ISSN: 0030-4018. DOI: `10.1016/j.optcom.2010.01.041`.

[66] C.-T. Tsai, C.-H. Lin, C.-T. Lin, Y.-C. Chi, and G.-R. Lin, "60-GHz Millimeter-wave Over Fiber with Directly Modulated Dual-mode Laser Diode", en, *Scientific Reports*, vol. 6, srep27919, Jun. 2016, ISSN: 2045-2322. DOI: `10.1038/srep27919`.

[67] R. Waterhouse and D. Novack, "Realizing 5G: Microwave Photonics for 5G Mobile Wireless Systems", *IEEE Microwave Magazine*, vol. 16, no. 8, pp. 84–92, Sep. 2015, ISSN: 1527-3342. DOI: `10.1109/MMM.2015.2441593`.

[68] J. S. Fandiño, P. Muñoz, D. Doménech, and J. Capmany, "A monolithic integrated photonic microwave filter", en, *Nature Photonics*, vol. 11, no. 2, pp. 124–129, Feb. 2017, ISSN: 1749-4885. DOI: `10.1038/nphoton.2016.233`.

[69] P. Bardella and I. Montrosset, "A new design procedure for DBR lasers exploiting the photon–photon resonance to achieve extended modulation bandwidth", *IEEE Journal of Selected Topics in Quantum Electronics*, vol. 19, no. 4, pp. 1 502 408–1 502 408, Jul. 2013, ISSN: 1077-260X. DOI: `10.1109/JSTQE.2013.2250260`.

[70] Y. Dai, X. Chen, J. Sun, Y. Yao, and S. Xie, "Dual-Wavelength DFB Fiber Laser Based on a Chirped Structure and the Equivalent Phase Shift Method", *IEEE Photonics Technology Letters*, vol. 18, no. 18, pp. 1964–1966, Sep. 2006, ISSN: 1041-1135. DOI: `10.1109/LPT.2006.882282`.

[71] J. Sun, Y. Dai, X. Chen, Y. Zhang, and S. Xie, "Stable Dual-Wavelength DFB Fiber Laser With Separate Resonant Cavities and Its Application in Tunable Microwave Generation", *IEEE Photonics Technology Letters*, vol. 18, no. 24, pp. 2587–2589, Dec. 2006, ISSN: 1041-1135. DOI: `10.1109/LPT.2006.887336`.

[72] G. Villanueva, P. Perez-Millan, J. Palaci, J. Cruz, M. Andres, and J. Marti, "Dual-Wavelength DFB Erbium-Doped Fiber Laser With Tunable Wavelength Spacing", *IEEE Photonics Technology Letters*,

vol. 22, no. 4, pp. 254–256, Feb. 2010, ISSN: 1041-1135. DOI: 10.1109/
LPT.2009.2038594.

[73] J. Sun, Y. Dai, Y. Zhang, X. Chen, and S. Xie, "Dual-Wavelength
DFB Fiber Laser Based on Unequalized Phase Shifts", *IEEE Photonics Technology Letters*, vol. 18, no. 23, pp. 2493–2495, Dec. 2006,
ISSN: 1041-1135. DOI: 10.1109/LPT.2006.887222.

[74] A. Hsu, S. L. Chuang, and T. Tanbun-Ek, "Tunable dual-mode operation in a chirped grating distributed-feedback laser", *IEEE Photonics Technology Letters*, vol. 12, no. 8, pp. 963–965, Aug. 2000, ISSN: 1041-
1135. DOI: 10.1109/68.867975.

[75] A. Klehr, J. Fricke, A. Knauer, G. Erbert, M. Walther, R. Wilk,
M. Mikulics, and M. Koch, "High-Power Monolithic Two-Mode DFB
Laser Diodes for the Generation of THz Radiation", English, *IEEE Journal of Selected Topics in Quantum Electronics*, vol. 14, no. 2,
pp. 289–294, Apr. 2008, ISSN: 1077-260X. DOI: 10.1109/JSTQE.2007.
913119.

[76] N. Kim, J. Shin, E. Sim, C. W. Lee, D.-S. Yee, M. Y. Jeon, Y. Jang,
and K. H. Park, "Monolithic dual-mode distributed feedback semiconductor laser for tunable continuous-wave terahertz generation",
Optics Express, vol. 17, no. 16, pp. 13 851–13 859, Aug. 2009. DOI:
10.1364/OE.17.013851.

[77] J. Hong, R. Finlay, R. Tong, C. Rogers, and D. Goodchild, "Simultaneous dual-wavelength operation in cascaded strongly gain-coupled
DFB lasers", *IEEE Photonics Technology Letters*, vol. 11, no. 11,
pp. 1354–1356, Nov. 1999, ISSN: 1041-1135. DOI: 10.1109/68.803043.

[78] S. D. Roh, T. S. Yeoh, R. B. Swint, A. E. Huber, C. Y. Woo, J. S.
Hughes, and J. J. Coleman, "Dual-wavelength InGaAs-GaAs ridge
waveguide distributed Bragg reflector lasers with tunable mode separation", *IEEE Photonics Technology Letters*, vol. 12, no. 10, pp. 1307–
1309, Oct. 2000, ISSN: 1041-1135. DOI: 10.1109/68.883812.

[79] L. A. Johansson, Z. Hu, D. J. Blumenthal, L. A. Coldren, Y. A.
Akulova, and G. A. Fish, "40-GHz dual-mode-locked widely tunable
sampled-grating DBR laser", English, *IEEE Photonics Technology*

Letters, vol. 17, no. 2, pp. 285–287, Feb. 2005, ISSN: 1041-1135. DOI: 10.1109/LPT.2004.840819.

[80]   D. W. Grund, G. A. Ejzak, G. J. Schneider, J. Murakowski, and D. W. Prather, "A Widely Tunable Narrow Linewidth RF Source Integrated in a Heterogeneous Photonic Module", *Journal of Lightwave Technology*, vol. 32, no. 7, pp. 1363–1369, Apr. 2014, ISSN: 0733-8724. DOI: 10.1109/JLT.2014.2302138.

[81]   T. N. Vu, A. Klehr, B. Sumpf, T. Hoffmann, A. Liero, and G. Tränkle, "Pulsed hybrid dual wavelength Y-branch-DFB laser-tapered amplifier system suitable for water vapor detection at 965 nm with 16 W peak power", in *Novel In-Plane Semiconductor Lasers XV*. International Society for Optics and Photonics, Mar. 2016, vol. 9767, 97670R. DOI: 10.1117/12.2208129.

[82]   M. Maiwald, B. Eppich, J. Fricke, A. Ginolas, F. Bugge, B. Sumpf, G. Erbert, and G. Tränkle, "Dual-Wavelength Y-Branch Distributed Bragg Reflector Diode Laser at 785 Nanometers for Shifted Excitation Raman Difference Spectroscopy", EN, *Applied Spectroscopy*, vol. 68, no. 8, pp. 838–843, Aug. 2014. DOI: 10.1366/13-07331.

[83]   B. Sumpf, J. Kabitzke, J. Fricke, P. Ressel, A. Müller, M. Maiwald, and G. Tränkle, "Dual-wavelength diode laser with electrically adjustable wavelength distance at 785 nm", *Optics Letters*, vol. 41, no. 16, pp. 3694–3697, Aug. 2016, ISSN: 1539-4794. DOI: 10.1364/OL.41.003694.

[84]   J. Piprek, *Semiconductor Optoelectronic Devices: Introduction to Physics and Simulation*. Elsevier, Oct. 2013, ISBN: 978-0-08-046978-2.

[85]   W. Li, J. Carrete, N. A. Katcho, and N. Mingo, "Shengbte: A solver of the boltzmann transport equation for phonons", *Computer Physics Communications*, vol. 185, no. 6, pp. 1747–1758, Jun. 2014, ISSN: 0010-4655. DOI: 10.1016/j.cpc.2014.02.015.

[86]   J. Carrete, B. Vermeersch, A. Katre, A. van Roekeghem, T. Wang, G. K. H. Madsen, and N. Mingo, "Almabte: A solver of the space–time dependent boltzmann transport equation for phonons in structured

materials", *Computer Physics Communications*, vol. 220, pp. 351–362, Nov. 2017, ISSN: 0010-4655. DOI: 10.1016/j.cpc.2017.06.023.

[87] Crosslight Software Inc., *PICS3D, Photonic Integrated Circuit Simulator in 3D*.

[88] N. K. Dutta, "Temperature dependence of threshold current of GaAs quantum well lasers", *Electronics Letters*, vol. 18, no. 11, pp. 451–453, May 1982, ISSN: 0013-5194. DOI: 10.1049/el:19820307.

[89] J. M. Luttinger and W. Kohn, "Motion of electrons and holes in perturbed periodic fields", *Physical Review*, vol. 97, no. 4, pp. 869–883, Feb. 1955. DOI: 10.1103/PhysRev.97.869.

[90] A. B. Ahmed, H. Saidi, S. Ridene, and H. Bouchriha, "Band structure, optical transition, and optical gain of type-II InAs(N)/GaSb quantum wells laser diodes modeled within 16-band and 14-band *kp* model", *IEEE Journal of Quantum Electronics*, vol. 51, no. 5, pp. 1–8, May 2015, ISSN: 0018-9197. DOI: 10.1109/JQE.2015.2412455.

[91] S. L. Chuang, "Optical gain of strained wurtzite GaN quantum-well lasers", *IEEE Journal of Quantum Electronics*, vol. 32, no. 10, pp. 1791–1800, Oct. 1996, ISSN: 0018-9197. DOI: 10.1109/3.538786.

[92] P. S. Zory, *Quantum Well Lasers*. Academic Press, 1993, ISBN: 978-0-12-781890-0.

[93] E. Yablonovitch and E. Kane, "Reduction of lasing threshold current density by the lowering of valence band effective mass", *Journal of Lightwave Technology*, vol. 4, no. 5, pp. 504–506, May 1986, ISSN: 0733-8724. DOI: 10.1109/JLT.1986.1074751.

[94] C.-S. Chang and S. L. Chuang, "Modeling of strained quantum-well lasers with spin-orbit coupling", *IEEE Journal of Selected Topics in Quantum Electronics*, vol. 1, no. 2, pp. 218–229, Jun. 1995, ISSN: 1077-260X. DOI: 10.1109/2944.401200.

[95] F. J. Dyson, "Feynman's proof of the maxwell equations", *American Journal of Physics*, vol. 58, pp. 209–211, Mar. 1990, ISSN: 0002-9505. DOI: 10.1119/1.16188.

[96] C. J. Reddy, M. D. Deshpande, C. R. Cockrell, and F. B. Beck, *Finite element method for eigenvalue problems in electromagnetics*, NASA-TP-3485. Dec. 1994.

[97] M. Stern *et al.*, "Finite difference analysis of planar optical wave-guides", *Progress In Electromagnetics Research*, vol. 10, pp. 123–186, 1995.

[98] D. F. Siriani, *Doping Optimization for High Efficiency in Semiconductor Diode Lasers and Amplifiers*. Mar. 2016.

[99] V. Shchukin, N. Ledentsov, K. Posilovic, V. Kalosha, T. Kettler, D. Seidlitz, M. Winterfeldt, D. Bimberg, N. Y. Gordeev, L. Y. Karachinsky, and et al., "Tilted wave lasers: A way to high brightness sources of light", *IEEE Journal of Quantum Electronics*, vol. 47, no. 7, pp. 1014–1027, Jul. 2011, ISSN: 0018-9197. DOI: 10.1109/JQE.2011.2132116.

[100] K. David, G. Morthier, P. Vankwikelberge, R. G. Baets, T. Wolf, and B. Borchert, "Gain-coupled DFB lasers versus index-coupled and phase shifted DFB lasers: A comparison based on spatial hole burning corrected yield", English, *IEEE Journal of Quantum Electronics*, vol. 27, no. 6, pp. 1714–1723, Jun. 1991, ISSN: 0018-9197. DOI: 10.1109/3.89938.

[101] W.-Y. Choi, J. C. Chen, and C. G. Fonstad, "Evaluation of coupling coefficients for laterally-coupled distributed feedback lasers", *Japanese Journal of Applied Physics*, vol. 35, no. 9R, p. 4654, Sep. 1996, ISSN: 1347-4065. DOI: 10.1143/JJAP.35.4654.

[102] C. Elachi, "Waves in active and passive periodic structures: A review", *Proceedings of the IEEE*, vol. 64, no. 12, pp. 1666–1698, Dec. 1976, ISSN: 0018-9219. DOI: 10.1109/PROC.1976.10409.

[103] M. Achtenhagen, A. Hardy, and C. S. Harder, "Lateral mode discrimination and self-stabilization in ridge waveguide laser diodes", *IEEE Photonics Technology Letters*, vol. 18, no. 3, pp. 526–528, Feb. 2006, ISSN: 1041-1135. DOI: 10.1109/LPT.2005.863992.

[104] A. Laakso, M. Dumitrescu, P. Pietilä, M. Suominen, and M. Pessa, "Optimization studies of single-transverse-mode 980 nm ridge-waveguide lasers", *Optical and Quantum Electronics*, vol. 40, no. 11–12, pp. 853–861, Sep. 2008, ISSN: 0306-8919, 1572-817X. DOI: 10.1007/s11082-009-9280-7.

[105]   R. Millett, K. Hinzer, A. Benhsaien, T. J. Hall, and H. Schriemer, "The impact of laterally coupled grating microstructure on effective coupling coefficients", *Nanotechnology*, vol. 21, no. 13, p. 134 015, 2010, ISSN: 0957-4484. DOI: 10.1088/0957-4484/21/13/134015.

[106]   H. Wenzel, R. Guther, A. M. Shams-Zadeh-Amiri, and P. Bienstman, "A comparative study of higher order bragg gratings: Coupled-mode theory versus mode expansion modeling", *IEEE Journal of Quantum Electronics*, vol. 42, no. 1, pp. 64–70, Jan. 2006, ISSN: 0018-9197. DOI: 10.1109/JQE.2005.859910.

[107]   P. Bienstman, "Rigorous and efficient modelling of wavelenght scale photonic components", PhD thesis, Ghent University, 2001.

[108]   H. Wenzel, J. Fricke, J. Decker, P. Crump, and G. Erbert, "High-power distributed feedback lasers with surface gratings: Theory and experiment", *IEEE Journal of Selected Topics in Quantum Electronics*, vol. 21, no. 6, pp. 352–358, Nov. 2015, ISSN: 1077-260X. DOI: 10.1109/JSTQE.2015.2429892.

[109]   R. Kazarinov and C. Henry, "Second-order distributed feedback lasers with mode selection provided by first-order radiation losses", *IEEE Journal of Quantum Electronics*, vol. 21, no. 2, pp. 144–150, Feb. 1985, ISSN: 0018-9197. DOI: 10.1109/JQE.1985.1072627.

[110]   L. M. Miller, J. T. Verdeyen, J. J. Coleman, R. P. Bryan, J. J. Alwan, K. J. Beernink, J. S. Hughes, and T. M. Cockerill, "A distributed feedback ridge waveguide quantum well heterostructure laser", *IEEE Photonics Technology Letters*, vol. 3, no. 1, pp. 6–8, Jan. 1991, ISSN: 1041-1135. DOI: 10.1109/68.68030.

[111]   P. Yeh, *Optical Waves in Layered Media*. John Wiley & Sons, Ltd, 1998.

[112]   H. Kogelnik and C. V. Shank, "Coupled-Wave Theory of Distributed Feedback Lasers", *Journal of Applied Physics*, vol. 43, no. 5, p. 2327, May 1972, ISSN: 00218979. DOI: doi:10.1063/1.1661499.

[113]   G. P. Agrawal and A. H. Bobeck, "Modeling of distributed feedback semiconductor lasers with axially-varying parameters", English, *IEEE Journal of Quantum Electronics*, vol. 24, no. 12, pp. 2407–2414, Dec. 1988, ISSN: 0018-9197. DOI: 10.1109/3.14370.

[114]   K. A. Winick, "Effective-index method and coupled-mode theory for almost-periodic waveguide gratings: A comparison", *Applied Optics*, vol. 31, no. 6, pp. 757–764, Feb. 1992. DOI: 10.1364/AO.31.000757.

[115]   H. Bissessur, "Effects of hole burning, carrier-induced losses and the carrier-dependent differential gain on the static characteristics of DFB lasers", English, *Journal of Lightwave Technology*, vol. 10, no. 11, pp. 1617–1630, Nov. 1992, ISSN: 0733-8724. DOI: 10.1109/50.184901.

[116]   K. O. Hill and A. Watanabe, "Envelope Gain Saturation in Distributed-Feedback Lasers", *Applied Optics*, vol. 14, no. 4, pp. 950–961, Apr. 1975. DOI: 10.1364/AO.14.000950.

[117]   A. A. Afanas'ev, V. K. Kononenko, and S. Y. Mikhnevich, "Influence of the gain saturation on the output performance of quantum-well heterostructures with modified distributed-feedback cavities", en, *Journal of Physics: Conference Series*, vol. 23, no. 1, p. 128, 2005, ISSN: 1742-6596. DOI: 10.1088/1742-6596/23/1/015.

[118]   T.-P. Nguyen, M. Schiemangk, S. Spießberger, H. Wenzel, A. Wicht, A. Peters, G. Erbert, and G. Tränkle, "Optimization of 780 nm DFB diode lasers for high-power narrow linewidth emission", en, *Applied Physics B*, vol. 108, no. 4, pp. 767–771, Sep. 2012, ISSN: 0946-2171, 1432-6649. DOI: 10.1007/s00340-012-5131-5.

[119]   W. Kobayashi, T. Ito, T. Yamanaka, T. Fujisawa, Y. Shibata, T. Kurosaki, M. Kohtoku, T. Tadokoro, and H. Sanjoh, "50-Gb/s direct modulation of a 1.3-µm InGaAlAs-based DFB laser with a ridge waveguide structure", *IEEE Journal of Selected Topics in Quantum Electronics*, vol. 19, no. 4, pp. 1 500 908–1 500 908, Jul. 2013, ISSN: 1077-260X. DOI: 10.1109/JSTQE.2013.2238509.

[120]   K. Petermann, "Calculated spontaneous emission factor for double-heterostructure injection lasers with gain-induced waveguiding", *IEEE Journal of Quantum Electronics*, vol. 15, no. 7, pp. 566–570, 1979. DOI: 10.1109/JQE.1979.1070064.

[121]   W. Hamel and J. Woerdman, "Nonorthogonality of the longitudinal eigenmodes of a laser", *Physical Review A*, vol. 40, no. 5, p. 2785, 1989.

[122] J. C. Pillay, Y. Natsume, A. D. Stone, and Y. D. Chong, "Generalized sub–Schawlow-Townes laser linewidths via material dispersion", *Physical Review A*, vol. 89, no. 3, p. 033 840, Mar. 2014. DOI: 10.1103/PhysRevA.89.033840.

[123] S. Ogita, Y. Kotaki, M. Matsuda, Y. Kuwahara, and H. Ishikawa, "Long-cavity multiple-phase-shift distributed feedback laser diode for linewidth narrowing", English, *Journal of Lightwave Technology*, vol. 8, no. 10, pp. 1596–1604, Oct. 1990, ISSN: 0733-8724. DOI: 10.1109/50.59202.

[124] W. Li and S. M. Sadeghi, "Spatial hole burning suppression for the distributed feedback laser diode with an asymmetric grating Gap structure", in *IEEE International Conference on Electro/Information Technology*, Jun. 2014, pp. 156–162. DOI: 10.1109/EIT.2014.6871754.

[125] G. Morthier and R. Baets, "Design of index-coupled DEB lasers with reduced longitudinal spatial hole burning", *Journal of Lightwave Technology*, vol. 9, no. 10, pp. 1305–1313, Oct. 1991, ISSN: 0733-8724. DOI: 10.1109/50.90928.

[126] M. Okai, T. Tsuchiya, K. Uomi, N. Chinone, and T. Harada, "Corrugation-pitch modulated MQW-DFB lasers with narrow spectral linewidth", *IEEE Journal of Quantum Electronics*, vol. 27, no. 6, pp. 1767–1772, Jun. 1991, ISSN: 0018-9197. DOI: 10.1109/3.90002.

[127] R. Bonello and I. Montrosset, "Analysis of multisection and multielectrode semiconductor lasers", *Journal of Lightwave Technology*, vol. 10, no. 12, pp. 1890–1900, Dec. 1992, ISSN: 0733-8724. DOI: 10.1109/50.202843.

[128] S. Hansmann, H. Hillmer, H. Walter, H. Burkhard, B. Hubner, and E. Kuphal, "Variation of coupling coefficients by sampled gratings in complex coupled distributed-feedback lasers", *IEEE Journal of Selected Topics in Quantum Electronics*, vol. 1, no. 2, pp. 341–345, Jun. 1995, ISSN: 1077-260X. DOI: 10.1109/2944.401213.

[129] K. A. Anselm, *Distributed feedback laser with improved optical field uniformity and mode stability*, US Patent 7,542,503, Jun. 2009.

[130] Y. Shi, R. Gu, and X. Chen, "A concave tapered DFB semiconductor laser based on reconstruction-equivalent-chirp technology", in *2010 Photonics Global Conference*, Dec. 2010, pp. 1–3. DOI: 10.1109/PGC.2010.5706027.

[131] Y. Shi, S. Li, R. Guo, R. Liu, Y. Zhou, and X. Chen, "A novel concavely apodized DFB semiconductor laser using common holographic exposure", EN, *Optics Express*, vol. 21, no. 13, pp. 16 022–16 028, Jul. 2013, ISSN: 1094-4087. DOI: 10.1364/OE.21.016022.

[132] J. Zheng, N. Song, Y. Zhang, Y. Shi, S. Tang, L. Li, R. Guo, and X. Chen, "An Equivalent-Asymmetric Coupling Coefficient DFB Laser With High Output Efficiency and Stable Single Longitudinal Mode Operation", *IEEE Photonics Journal*, vol. 6, no. 6, pp. 1–9, Dec. 2014, ISSN: 1943-0655. DOI: 10.1109/JPHOT.2014.2368776.

[133] C. Ke, C. Wang, J. Fu, Y. Zhou, and C. Li, "A horn ridge waveguide DFB laser with reduced spatial hole burning for high-speed modulation", en, *Optical Review*, vol. 24, no. 3, pp. 345–350, Jun. 2017, ISSN: 1340-6000, 1349-9432. DOI: 10.1007/s10043-017-0326-y.

[134] K. David, J. Buus, and R. G. Baets, "Basic analysis of AR-coated, partly gain-coupled DFB lasers: The standing wave effect", *IEEE Journal of Quantum Electronics*, vol. 28, no. 2, pp. 427–434, Feb. 1992, ISSN: 0018-9197. DOI: 10.1109/3.123269.

[135] H. H. Gatzen, V. Saile, and J. Leuthold, "Deposition technologies", in *Micro and Nano Fabrication*. Springer, Berlin, Heidelberg, 2015, pp. 65–203, ISBN: 978-3-662-44394-1. DOI: 10.1007/978-3-662-44395-8_3.

[136] D. Saeedkia, R. R. Mansour, and S. Safavi-Naeini, "The interaction of laser and photoconductor in a continuous-wave terahertz photomixer", *IEEE Journal of Quantum Electronics*, vol. 41, no. 9, pp. 1188–1196, Sep. 2005, ISSN: 0018-9197. DOI: 10.1109/JQE.2005.852804.

[137] N. H. Zhu, W. Li, J. H. Ke, H. G. Zhang, J. W. Man, and J. G. Liu, "Optical spectral structure and frequency coherence", in *Optoelectronic Devices and Properties*. InTech, 2011. DOI: 10.5772/15777.

[138] D. Wake, C. R. Lima, and P. A. Davies, "Optical generation of millimeter-wave signals for fiber-radio systems using a dual-mode DFB semiconductor laser", *IEEE Transactions on Microwave Theory and Techniques*, vol. 43, no. 9, pp. 2270–2276, Sep. 1995, ISSN: 0018-9480. DOI: `10.1109/22.414575`.

[139] U. Gliese, T. N. Nielsen, S. Norskov, and K. E. Stubkjaer, "Multifunctional fiber-optic microwave links based on remote heterodyne detection", *IEEE Transactions on Microwave Theory and Techniques*, vol. 46, no. 5, pp. 458–468, May 1998, ISSN: 0018-9480. DOI: `10.1109/22.668642`.

[140] K. Sato, "100 GHz optical pulse generation using Fabry-Pérot laser under continuous wave operation", *Electronics Letters*, vol. 37, no. 12, pp. 763–764, Jun. 2001, ISSN: 0013-5194. DOI: `10.1049/el:20010527`.

[141] L. Chusseau, F. Philippe, P. Viktorovitch, and X. Letartre, "Mode competition in a dual-mode quantum-dot semiconductor microlaser", *Physical Review A*, vol. 88, no. 1, p. 015803, Jul. 2013. DOI: `10.1103/PhysRevA.88.015803`.

[142] H. Virtanen, *Narrow-Linewidth DFB and DBR Lasers with Surface Gratings Fabricated Using UV-Nanoimprint Lithography*, English, ser. Tampere University of Technology. Publication. Tampere University of Technology, Nov. 2017, ISBN: 978-952-15-4048-6.

[143] H. Ludvigsen, M. Tossavainen, and M. Kaivola, "Laser linewidth measurements using self-homodyne detection with short delay", *Optics Communications*, vol. 155, no. 1, pp. 180–186, Oct. 1998, ISSN: 0030-4018. DOI: `10.1016/S0030-4018(98)00355-1`.

[144] H. Bissessur, "Effects of hole burning, carrier-induced losses and the carrier-dependent differential gain on the static characteristics of DFB lasers", *Journal of Lightwave Technology*, vol. 10, no. 11, pp. 1617–1630, Nov. 1992, ISSN: 0733-8724. DOI: `10.1109/50.184901`.

[145] D. J. Dougherty, R. C. Gutierrez, S. Dubovitsky, and S. Forouhar, "Semiconductor laser linewidth measurements for space interferometry applications", in *Testing, Packaging, Reliability, and Applications of Semiconductor Lasers IV*. International Society for Optics

and Photonics, Apr. 1999, vol. 3626, pp. 115–123. DOI: 10.1117/12.345421.

[146]   O. Boukari, L. Hassine, H. Bouchriha, and M. Ketata, "Study of dynamic chirp in direct modulated DFB laser for C-OFDR application", *Optics Communications*, vol. 283, no. 10, pp. 2214–2223, May 2010, ISSN: 0030-4018. DOI: 10.1016/j.optcom.2010.01.050.

[147]   K. Asaka, A. Kanda, A. Ohki, T. Kurosaki, R. Yoshimura, H. Sanjoh, T. Ito, M. Nakamura, and M. Yoneyama, "Low-cost and small BOSA employing impedance matching circuits for 10G-EPON", in *2012 17th Opto-Electronics and Communications Conference*. Jul. 2012, pp. 81–82. DOI: 10.1109/OECC.2012.6276381.

[148]   T. Yamamoto, "High-speed directly modulated lasers", in *OFC/N-FOEC*. Mar. 2012, pp. 1–39.

[149]   N. E. Huang, Z. Wu, S. R. Long, K. C. Arnold, X. Chen, and K. Blank, "On instantaneous frequency", *Advances in Adaptive Data Analysis*, vol. 01, no. 02, pp. 177–229, Apr. 2009, ISSN: 1793-5369. DOI: 10.1142/S1793536909000096.

[150]   Z. Xihua, L. Bing, P. Wei, Y. Lianshan, S. Andreas, and Y. Jianping, "Photonics for microwave measurements", *Laser & Photonics Reviews*, vol. 10, no. 5, pp. 711–734, Sep. 2016, ISSN: 1863-8880. DOI: 10.1002/lpor.201600019.

[151]   M. Pagani, B. Morrison, Y. Zhang, A. Casas-Bedoya, T. Aalto, M. Harjanne, M. Kapulainen, B. J. Eggleton, and D. Marpaung, "Low-error and broadband microwave frequency measurement in a silicon chip", *Optica*, vol. 2, no. 8, pp. 751–756, Aug. 2015, ISSN: 2334-2536. DOI: 10.1364/OPTICA.2.000751.

[152]   Y. Ding, G. Ternent, A. Saeed, C. J. Hamilton, C. J. Hamilton, N. Hempler, G. P. A. Malcolm, G. T. Maker, M. Sorel, and D. J. Paul, "GaAs-based distributed feedback laser at 780 nm for 87Rb cold atom quantum technology", in *2017 European Conference on Lasers and Electro-Optics and European Quantum Electronics Conference (2017), paper CB_7_2*. Optical Society of America, Jun. 2017, CB_7_2.

[153] O. Brox, F. Bugge, A. Mogilatenko, E. Luvsandamdin, A. Wicht, H. Wenzel, and G. Erbert, "Distributed feedback lasers in the 760 to 810 nm range and epitaxial grating design", *Semiconductor Science and Technology*, vol. 29, no. 9, p. 095 018, 2014, ISSN: 0268-1242. DOI: `10.1088/0268-1242/29/9/095018`.

[154] M. Radziunas, A. Glitzky, U. Bandelow, M. Wolfrum, U. Troppenz, J. Kreissl, and W. Rehbein, "Improving the Modulation Bandwidth in Semiconductor Lasers by Passive Feedback", English, *IEEE Journal of Selected Topics in Quantum Electronics*, vol. 13, no. 1, pp. 136–142, Feb. 2007, ISSN: 1077-260X. DOI: `10.1109/JSTQE.2006.885332`.

[155] F. Gerschütz, M. Fischer, J. Koeth, I. Krestnikov, A. Kovsh, C. Schilling, W. Kaiser, S. Höfling, and A. Forchel, "1.3 µm quantum dot laser in coupled-cavity-injection-grating design with bandwidth of 20 GHz under direct modulation", *Optics Express*, vol. 16, no. 8, pp. 5596–5601, Apr. 2008, ISSN: 1094-4087. DOI: `10.1364/OE.16.005596`.

[156] M. Mohrle, B. Sartorius, C. Bornholdt, S. Bauer, O. Brox, A. Sigmund, R. Steingruber, H. Radziunas, and H. J. Wunsche, "Detuned grating multisection-RW-DFB lasers for high-speed optical signal processing", *IEEE Journal of Selected Topics in Quantum Electronics*, vol. 7, no. 2, pp. 217–223, Mar. 2001, ISSN: 1077-260X. DOI: `10.1109/2944.954133`.

[157] M. Soldo, M. Zanola, M. J. Strain, M. Sorel, and G. Giuliani, "Integrated device with three mutually coupled DFB lasers for tunable, narrow linewidth, mm-wave signal generation", in *CLEO/QELS: 2010 Laser Science to Photonic Applications*. May 2010, pp. 1–2. DOI: `10.1364/CLEO.2010.CTuKK2`.

[158] F. v. Dijk, A. Accard, A. Enard, O. Drisse, D. Make, and F. Lelarge, "Monolithic dual wavelength DFB lasers for narrow linewidth heterodyne beat-note generation", in *2011 International Topical Meeting on Microwave Photonics jointly held with the 2011 Asia-Pacific Microwave Photonics Conference*. Oct. 2011, pp. 73–76. DOI: `10.1109/MWP.2011.6088672`.

[159]   C. Zhang, S. Liang, H. Zhu, and W. Wang, "Widely tunable dual-mode distributed feedback laser fabricated by selective area growth technology integrated with Ti heaters", *Optics Letters*, vol. 38, no. 16, pp. 3050–3053, Aug. 2013, ISSN: 1539-4794. DOI: `10.1364/OL.38.003050`.

[160]   K. Balakier, M. J. Fice, F. v. Dijk, G. Kervella, G. Carpintero, A. J. Seeds, and C. C. Renaud, "Optical injection locking of monolithically integrated photonic source for generation of high purity signals above 100 GHz", *Optics Express*, vol. 22, no. 24, pp. 29 404–29 412, Dec. 2014, ISSN: 1094-4087. DOI: `10.1364/OE.22.029404`.

[161]   L. Yu, D. Lu, Y. Sun, and L. Zhao, "Tunable photonic microwave generation by directly modulating a dual-wavelength amplified feedback laser", *Optics Communications*, vol. 345, no. Supplement C, pp. 57–61, Jun. 2015, ISSN: 0030-4018. DOI: `10.1016/j.optcom.2015.01.068`.

[162]   J. W. Wu, Q. Qiu, X. P. Zhang, and Y. H. Won, "Simultaneous generation of microwave, millimeter-wave, and terahertz photonic signal based on two-color semiconductor laser subject to single-beam optical injection", *IEEE Journal of Selected Topics in Quantum Electronics*, vol. 23, no. 4, pp. 1–8, Jul. 2017, ISSN: 1077-260X. DOI: `10.1109/JSTQE.2016.2646521`.

ORIGINAL PAPERS

I

DISTRIBUTED FEEDBACK LASERS WITH ALTERNATING LATERALLY-COUPLED RIDGE-WAVEGUIDE SURFACE GRATINGS

by
Uusitalo, T., Virtanen, H., Karjalainen, M., Ranta, S., Viheriälä, J., &
Dumitrescu, M. 2017

Distributed Feedback Lasers with Alternating Laterally-Coupled Ridge-Waveguide Surface Gratings

TOPI UUSITALO[1,*], HEIKKI VIRTANEN[1], MAIJA KARJALAINEN[1], SANNA RANTA[1], JUKKA VIHERIÄLÄ[1], AND MIHAIL DUMITRESCU[1]

[1]Optoelectronics Research Centre, Tampere University of Technology, Tampere, Finland
*Corresponding author: topi.uusitalo@tut.fi

Distributed feedback lasers with laterally-coupled ridge waveguide surface gratings having the protrusions placed alternately on the lateral sides of the ridge are demonstrated. This configuration enables easier-to-fabricate wider trenches than in the gratings with protrusions placed symmetrically on both sides of the ridge. The design strategy and coupling coefficient calculations are discussed. The output characteristics of fabricated lasers show lower threshold currents and higher slope efficiencies for devices with 1st-order alternating gratings than for those with 3rd-order symmetric gratings having comparable grating trench widths and similar coupling coefficients. © 2017 Optical Society of America

Distributed feedback (DFB) lasers have been conventionally fabricated by using buried gratings [1], which requires at least one re-growth step. Surface gratings eliminate the need for re-growth and allow device processing in a single step after the epitaxial growth, simplifying the fabrication process and reducing the fabrication cost. The surface gratings also limit the interaction between the injected carriers and the defect-prone processed interfaces, improving the laser performances and reliability. The DFB lasers with laterally-coupled ridge-waveguide (LC-RWG) surface gratings have been reported to suffer from higher threshold current densities and lower slope efficiencies in single mode operation than DFB lasers with buried gratings [2–6]. This is largely due to the fact that typically the surface gratings achieve smaller coupling coefficients than buried gratings. The diminished coupling coefficient is derived from the fact that the overlap between the grating area and the transverse optical field distribution (i.e. the grating optical confinement factor) is inherently smaller for surface gratings than for buried gratings. The reduction in the grating optical confinement factor can be compensated by the surface gratings' increased refractive index contrast along the grating area when the surface grating trenches are etched deep enough to bring the surface grating area close to the active region. Etching deep grating trenches is restricted by the technologically-achievable etching aspect ratio (the ratio between trench depth and trench width) [7]. Consequently, the possibility to achieve a high surface grating coupling coefficient through etching deeper trenches is technologically limited by the grating trench width.

A straightforward way to increase the trench width of the LC-RWG surface gratings, while keeping the grating order, is to remove the lateral protrusions alternately from one and from the other side of the ridge [8], as illustrated in Figure 1.
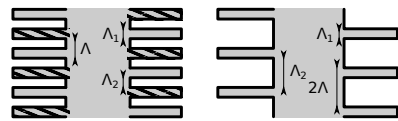
Fig. 1. Top view sketches of LC-RWG gratings with rectangular protrusions placed symmetrically on both sides of the ridge (left panel) and with the rectangular protrusions alternately placed on the sides of the ridge (right panel).

In this way the grating trench width is increased from:

$$\Lambda_2 = (1 - \gamma_{sym}) \cdot m \cdot \frac{\lambda_{\text{Bragg}}}{2 \cdot n_{\text{eff}}(\gamma_{sym})} \tag{1}$$

for the LC-RWG gratings with protrusions placed simultaneously/symmetrically on both sides of the ridge, to:

$$\Lambda_2 = (2 - \gamma_{sym}) \cdot m \cdot \frac{\lambda_{\text{Bragg}}}{2 \cdot n_{\text{eff}}(\gamma_{alt})} = (2 - 2 \cdot \gamma_{alt}) \cdot m \cdot \frac{\lambda_{\text{Bragg}}}{2 \cdot n_{\text{eff}}(\gamma_{alt})} \tag{2}$$

for the LC-RWG gratings with protrusions placed alternately on the sides of the ridge; where Λ_2 is the trench width, γ_{sym} is the filling factor of the symmetrical grating ($\gamma_{sym} = \Lambda_1 / \Lambda$, with Λ the period of the longitudinal variation of the effective refractive index and Λ_1 lateral protrusion width in the longitudinal direction), γ_{alt} is the filling factor of the corresponding alternating grating ($\gamma_{alt} = \Lambda_1 / (2 \cdot \Lambda) = \gamma_{sym}/2$), m is the grating order, λ_{Bragg} is the grating Bragg resonance wavelength and $n_{\text{eff}}(\gamma_{sym})$ and $n_{\text{eff}}(\gamma_{alt})$ are the effective refractive index values for the symmetrical and alternating gratings, respectively.

As illustrated in Figure 2, besides the alternating gratings filling factor range $\gamma_{alt} \in [0, 0.5]$ that corresponds to a symmetrical grating filling factor range of $\gamma_{sym} \in [0, 1]$ and leads to trenches wider than the protrusions; the alternating grating filling factor can also cover the range $\gamma_{alt} \in [0.5, 1]$, when alternately removing the trenches, which leads to protrusions wider than the trenches. The alternating grating filling factor range of $\gamma_{alt} \in [0, 0.5]$ was the target of our studies due to the fact that it mitigates the aspect ratio limitation of etching.
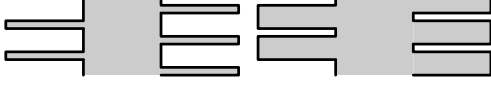
Fig. 2. Top-view sketches of alternating LC-RWG gratings with filling factor in the $[0, 0.5]$ range (left panel) and with filling factor in the $[0.5, 1]$ range (right panel).

The laterally alternating gratings reduce the contrast in the longitudinal variation of the effective refractive index, as compared with the corresponding symmetrical gratings, but keep the period and profile of this longitudinal variation (with the discontinuities at the same positions as for the symmetrical placement), thus having a similar Bragg resonance with the corresponding symmetrical gratings. Concomitantly, the laterally alternating gratings increase the refractive index contrast in the longitudinally-averaged transverse refractive index distribution, as compared with the corresponding symmetrical gratings, inducing better single transverse mode stability when properly designed [9, 10]. In the range $\gamma_{alt} \in [0, 0.5]$ the alternating removing of the protrusions reduces the lateral current spreading into the protrusions, improving the injection efficiency.

The possibility to increase the trench width with the alternating placement of the protrusions enabled us to compare DFB lasers having 3rd-order symmetrical gratings with DFB lasers having 1st-order alternating gratings. First order gratings can provide lower radiative losses [11], reduced sensitivity of the grating coupling coefficient to filling factor variations, and fewer mode hops than higher order gratings [12].

Two types of 780 nm DFB lasers were fabricated from the same epiwafer by soft-stamp ultra-violet nanoimprint lithography (UV-NIL) [3]: one with 1st-order alternating LC-RWG gratings and the other with 3rd-order symmetrical LC-RWG gratings. The growth of the epilayer structure was done by solid source molecular beam epitaxy (SS-MBE) on a (100) oriented n-GaAs-substrate. The epilayer structure comprised a 8 nm $Al_{0.09}Ga_{0.91}As$ quantum well, placed between 300 nm un-doped $Al_{0.35}Ga_{0.65}As$ waveguide layers, surrounded by low-optical-contrast 1000 nm p- and n-doped $Al_{0.50}Ga_{0.50}As$ cladding layers. 50 nm $Al_{0.20}Ga_{0.80}As$ layers were placed on the outside of the cladding layers to ease the carrier flow from the 200 nm n-GaAs buffer layer grown on the substrate and from the 200 nm p-GaAs top contact layer.

The etch mask for both grating types was defined by a bi-layer lift-off process on a 200 nm thick SiO_2 layer deposited on the top p-side of the epiwafer. In the lift-off process polydimethylglutarimide (PMGI) and mr-UVCur06 UV-NIL resist layers were successively deposited on top of the SiO_2 by spin coating. The pattern of the etch mask was transferred mechanically from a soft stamp [3] to the UV-NIL-resist by imprinting. After the mr-UVCur06 residual layer was removed by reactive ion etching (RIE), the PMGI layer was developed from the imprinted

areas. A 50 nm layer of Ti was evaporated on the wafer and the remaining PMGI layer was dissolved, which lifted off the Ti layer on top of it. While the Ti mask protected the ridge and the laterally-protruding grating regions, the unprotected areas were etched through the SiO_2 layer with CHF_3/Ar by RIE, followed by Cl_2/N_2 inductively coupled plasma (ICP) etching of the semiconductor layers to the interface between the p-cladding and waveguide. After ICP etching, the etching mask was removed by RIE and the structure was planarized with benzocyclobutene (BCB). A 250 nm thick layer of SiO_2 was deposited on the wafer and the contact openings were patterned in positive UV-resist by UV-lithography and etched by RIE. The protective positive UV-resist was then dissolved. Afterwards, the p-side contact was formed by evaporating a Ti/Pt/Au layer stack. The wafer was thinned to 130 μm, and the ohmic contact was formed on the n-side by evaporating Ni/Au/Ge/Au layers and annealing the sample under N_2 ambient at 370 °C for 60 s. The n-side contact was strengthened by evaporating 50 and 200 nm layers of Ni and Au, respectively. Finally, the devices were diced, anti-reflection (AR) coated by a quarter-wavelength thick layer of alumina, p-side up mounted on AlN submounts with electrically conductive silver-filled epoxy, and bonded with gold wires.

Scanning electron microscope (SEM) images of the fabricated two types of LC-RWG surface gratings are shown in Figure 3.
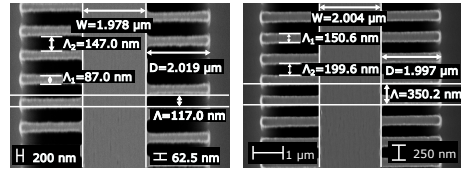

Fig. 3. Top view SEM pictures of 1st-order alternating LC-RWG gratings (left panel) and 3rd-order symmetrical LC-RWG gratings (right panel).

To compare the 1st-order alternating and 3rd-order symmetrical LC-RWG gratings from the possibility of fabrication point of view, one should compare their dependencies of the coupling coefficient on the grating trench width. The coupling coefficient formula for the LC-RWG gratings with rectangular protrusions symmetrically placed on both sides of the ridge [9, 13]:

$$\kappa_{sym} = \frac{k_0}{2 \cdot n_{eff}(\gamma_{sym})} \cdot (n_2^2 - n_1^2) \cdot \Gamma_g(\gamma_{sym}) \cdot \frac{\sin(\pi \cdot m \cdot \gamma_{sym})}{\pi \cdot m}, \tag{3}$$

must be adjusted for calculating the coupling coefficient for the LC-RWG gratings with rectangular protrusions placed alternately on the sides of the ridge:

$$\kappa_{alt} = \frac{k_0}{2 \cdot n_{eff}(\gamma_{alt})} \cdot (n_2^2 - n_1^2) \cdot \frac{\Gamma_g(\gamma_{alt})}{2} \cdot \frac{\sin(\pi \cdot m \cdot 2 \cdot \gamma_{alt})}{\pi \cdot m}, \tag{4}$$

where k_0 is the free space wave number; n_2 and n_1 are the refractive index values in the protrusion and trench regions, respectively; $\Gamma_g(\gamma_{sym})$ and $\Gamma_g(\gamma_{alt})$ are the optical confinement factors in the grating areas on both sides of the ridge for the symmetric and alternating gratings, respectively; and m is the grating order. It should be noted that the alternating grating filling factor is half of the filling factor of the corresponding symmetrical grating

(due to the removal of every second protrusion on both sides of the ridge) and that the division by 2 of the grating optical confinement factor in Equation (4) derives from the alternating grating interacting with the optical field just on one side of the ridge at a time.
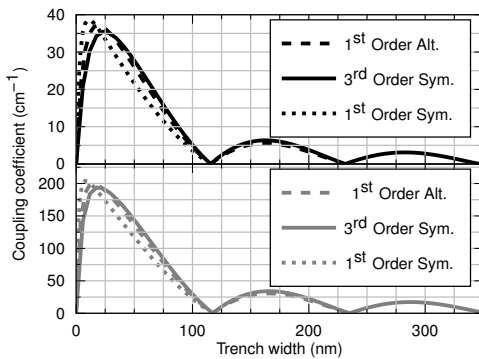

Fig. 4. Coupling coefficient (κ) variation with trench width for 1st-order alternating , 1st-order symmetrical and 3rd-order symmetrical LC-RWG gratings for the reported structure (top panel) and for a structure targeting a high κ (bottom panel).

The top panel of Figure 4 shows the coupling coefficients' dependencies on grating trench width calculated using Equation (3) and (4) for the fabricated 1st-order alternating and 3rd-order symmetrical LC-RWG gratings, as well as for the 1st-order symmetrical LC-RWG grating with the same structural parameters. The coupling coefficient dependencies on the LC-RWG grating trench width are similar for narrow trenches, irrespective of the grating order, due to the particular interaction of the LC-RWG gratings with the optical field. At the same trench width the filling factor for higher-order gratings is increased, leading to lower optical contrast between the transverse areas corresponding to compact semiconductor material and the grating regions. This raises the optical confinement factor in the grating regions, which compensates for the coupling coefficient reduction due to the increased grating order. Similarly, the alternating gratings have a higher filling factor and a higher optical confinement factor in the grating regions than the symmetrical gratings with the same grating trench width, which compensates for interacting with the optical field only on one side of the ridge at a time.

When compared with 1st-order symmetrical gratings, the 1st-order alternating LC-RWG gratings achieve slightly higher coupling coefficient values for narrow trench widths and extend the range of trench widths well beyond 100 nm, to more technologically-manageable values. As compared with 3rd-order symmetrical gratings, the 1st-order alternating gratings bring reduced radiative losses (due to the lower grating order) and reduced lateral current spreading through the protrusions.

In the fabricated 1st-order alternating LC-RWG gratings Λ_1 was designed to be 85 nm, while the trench width Λ_2 was varied from 143 to 150 nm for different devices. The corresponding 1st-order symmetrical gratings would have Λ_2 varying from 29 to 32.5 nm, well below the trench widths that could be etched to a 1250 nm depth. In the 3rd-order symmetrical LC-RWG gratings Λ_1 and Λ_2 were designed to vary from 147 to 150 nm and from

196 to 200 nm, respectively. The central ridge width (W) and the lateral extension of the protrusions (D) are $\sim$2 µm (see Figure 3).

The simulated coupling coefficient values were $\sim 5\,\mathrm{cm}^{-1}$ and $\sim 4.6\,\mathrm{cm}^{-1}$ for the fabricated 2.4 mm long 1st-order alternating and 3rd-order symmetrical gratings, corresponding to coupling strengths of $\kappa \cdot L$=1.2 and $\kappa \cdot L$=1.1, respectively. The bottom panel of Figure 4 shows that a much higher coupling coefficient could be obtained for structural parameters targeting high κ (i.e. for W=1 µm, D=2 µm and 100 nm waveguide layer thickness). However, the designs of the fabricated devices targeted narrow intrinsic laser linewidth [5], by low coupling coefficient (achieved with 300 nm large optical cavity low-optical-contrast waveguide layers and W=2 µm) and long laser cavity.

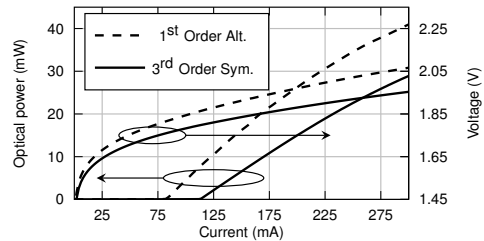**Fig. 5.** Continuous wave LIV-characteristics of 2.4 mm long DFB lasers with 1st-order alternating and with 3rd-order symmetrical LC-RWG gratings.

The continuous wave LIV-characteristics of 2.4 mm long DFB lasers fabricated from the same epiwafer with 1st-order alternating and with 3rd-order symmetrical LC-RWG gratings were measured at 20 °C. Figure 5 gives a comparison between typical LIV-characteristics for the two device types.

The average threshold currents determined from measuring several devices are shown in Table 1, where $\sigma(I_{\mathrm{th}})$ is the standard deviation of the threshold currents, $\bar{I}_{\mathrm{th}}$ is the average threshold current, and N is the number of measured devices.

Table 1. Threshold current statistics for DBF lasers with 1st-order alternating and 3rd-order symmetric LC-RWG gratings.

Grating order	1st Alt.	3rd Sym.
$\sigma(I_{\mathrm{th}})$ (mA)	10.6	11.0
$\bar{I}_{\mathrm{th}}$ (mA)	75.2	113.2
N	19	18

The results given in Table 1 and Figure 5 indicate that the devices with alternating gratings have improved slope efficiency and reduced threshold current, but increased series resistance. The increased series resistance, apparent from Figure 5, is associated with the fact that less current is diverted through the lateral protrusions, which is beneficial since this diverted current has limited contribution to the stimulated emission.

Figure 6 indicates that the near field mode profiles created by 1st-order alternating and 3rd-order symmetrical LC-RWG gratings are nearly the same. The field patterns also confirm that, when properly designed [9], the alternating gratings have
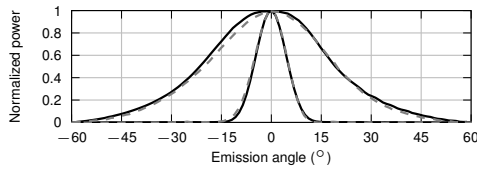
Fig. 6. Fast and slow axis far fields for the DFB lasers with 1st-order alternating (dashed line) and with 3rd-order symmetrical (solid line) LC-RWG gratings. The far-field full width at half maximum is ∼40° on the fast axis and ∼11° on the slow axis for both grating types.

no detrimental effect on the single transverse mode operation and on the emission profile of the laser.

Figure 7 presents a comparison of the optical spectra variation with bias current change from threshold to 300 mA. The side-mode suppression-ratio (SMSR) variation with bias current for the two types of DFB lasers is given in Figure 8.

The increased slope of the emission wavelength change with bias current for the 3rd-order symmetrical gratings indicates more heating, determined by a larger amount of current leakage through the protrusions. Figure 7 also shows that the emitted grating modes have a similar detuning factor (which is the difference between the gain maximum and the emission/grating mode wavelengths). The similarity between detuning factors in-
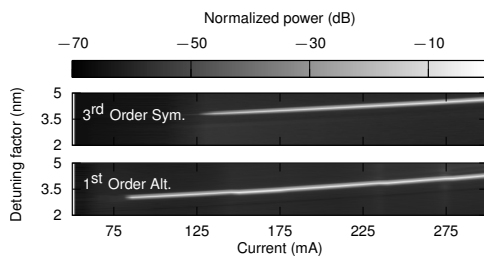
Fig. 7. Optical spectra variation for the 2.4 mm long DFB lasers with 3rd-order symmetrical and 1st-order alternating LC-RWG gratings as a function of bias current. The slopes of the emission peak wavelength variation with bias currents are 5.5 and 5.1 nm/A, respectively.
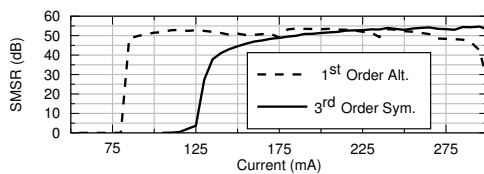
Fig. 8. Measured SMSR variation with bias current for 2.4 mm long DFB lasers with 3rd-order symmetrical and 1st-order alternating LC-RWG gratings.

dicates that the improved performance of the alternating grating is not due to better gain alignment.

Figure 7 and Figure 8 illustrate that, when properly designed [9], the 1st-order alternating LC-RWG gratings lead to a broad stable single mode operation range with high SMSR, providing improved stability to the DFB single-mode emission when compared with the 3rd-order symmetrical LC-RWG gratings.

The reported results reveal that LC-RWG surface gratings with alternating lateral protrusions can be implemented with wider grating trenches (N.B. possibly wider than the grating period), enabling the fabrication of low-order gratings within the limitations set by the technologically-achievable etching aspect ratio. This is particularly relevant for short-wavelength visible lasers, where etching aspect ratio limitations do not allow the fabrication of 1st-order LC-RWG surface gratings. It has also been shown that, when properly designed, the alternating LC-RWG surface gratings can achieve high coupling coefficients and provide stable single-mode operation with good mode profile. The reported results also point out that DFB lasers employing 1st-order alternating gratings have high spectral purity and improved threshold current and slope efficiency, as compared to DFB lasers with 3rd-order symmetrical gratings of comparable trench widths and similar coupling coefficients. The improvements are derived mainly from reduced radiation losses and from decreased leakage of the current through the lateral protrusions of the 1st-order alternating gratings.

ACKNOWLEDGMENT.

REFERENCES

1. S. Akiba, K. Utaka, K. Sakai, and Y. Matsushima, IEEE Journal of Quantum Electronics **19**, 1052 (1983).
2. K. Dridi, A. Benhsaien, J. Zhang, and T. J. Hall, IEEE Photonics Technology Letters **26**, 1192 (2014).
3. J. Viheriälä, J. Tommila, T. Leinonen, M. Dumitrescu, L. Toikkanen, T. Niemi, and M. Pessa, Microelectronic Engineering **86**, 321 (2009).
4. K. Takaki, T. Kise, K. Maruyama, K. Hiraiwa, N. Yamanaka, M. Funabashi, and A. Kasukawa, Furukawa review **23** (2003).
5. T.-P. Nguyen, M. Schiemangk, S. Spießberger, H. Wenzel, A. Wicht, A. Peters, G. Erbert, and G. Tränkle, Applied Physics B **108**, 767 (2012).
6. Y.-L. Cao, X.-N. Hu, X.-S. Luo, J.-F. Song, Y. Cheng, C.-M. Li, C.-Y. Liu, H. Wang, L. Tsung-Yang, G.-Q. Lo *et al.*, Optics express **23**, 8800 (2015).
7. J. Yeom, Y. Wu, J. C. Selby, and M. A. Shannon, Journal of Vacuum Science & Technology B: Microelectronics and Nanometer Structures Processing, Measurement, and Phenomena **23**, 2319 (2005).
8. M. Dumitrescu, T. Uusitalo, and H. Virtanen, Patent Cooperation Treaty application PCT/EP2016/064476 (2016).
9. T. Uusitalo, H. Virtanen, and M. Dumitrescu, Optical and Quantum Electronics **49**, 206 (2017).
10. H. Virtanen, T. Uusitalo, and M. Dumitrescu, Optical and Quantum Electronics **49**, 160 (2017).
11. W. Streifer, R. Burnham, and D. Scifres, IEEE Journal of Quantum Electronics **12**, 737 (1976).
12. R. R. Millett, K. Hinzer, T. J. Hall, and H. Schriemer, IEEE Journal of Quantum Electronics **44**, 1145 (2008).
13. W. Streifer, D. Scifres, and R. Burnham, IEEE Journal of Quantum Electronics **11**, 867 (1975).

II

TRANSVERSE STRUCTURE OPTIMIZATION OF DISTRIBUTED FEEDBACK AND DISTRIBUTED BRAGG REFLECTOR LASERS WITH SURFACE GRATINGS

CrossMark

Transverse structure optimization of distributed feedback and distributed Bragg reflector lasers with surface gratings

Topi Uusitalo[1] (ID) · **Heikki Virtanen**[1] · **Mihail Dumitrescu**[1]

© Springer Science+Business Media New York 2017

Abstract Two figures of merit for single transverse mode operation and an accurate procedure for calculating the coupling coefficient in distributed feedback lasers with laterally-coupled ridge-waveguide surface grating structures and in distributed Bragg reflector lasers with etched-through-ridge-waveguide surface gratings are introduced. Based on the difference in optical confinement between the pumped and un-pumped regions in the transverse plane, the single transverse mode operation figures of merit are effective and easy to calculate, while the improved coupling coefficient calculation procedure gives experimentally confirmed better results than the conventional calculation approaches, particularly for surface gratings with variable refractive index in the grating areas.

Keywords Surface gratings · Single transverse mode operation · Grating coupling coefficient

1 Introduction

Single transverse mode (STM) and single longitudinal mode (SLM) operation are essential laser characteristics for a broad range of applications ranging from optical communications to atomic clocks. The fabrication of conventional buried-grating distributed feedback

✉ Topi Uusitalo
  topi.uusitalo@tut.fi

1   ORC, Tampere University of Technology, P.O. Box 692, 33101, Tampere, Finland

⚛ Springer

(DFB) and distributed Bragg reflector (DBR) lasers requires two or more epitaxial growth steps. Removing the epiwafer from the molecular beam epitaxy reactor, processing the gratings, cleaning the processed surface and overgrowing the structure with the remaining top epilayer structure is a complicated fabrication process, which affects the device performance, decreases the fabrication yield and reduces device reliability, ultimately increasing the device cost. The reduction in reliability is mainly due to the fact that the defect-prone processed interfaces are placed in regions with high operating temperatures and they interact strongly both with the carrier flow and with a high-intensity optical field (the buried gratings must be placed in regions with high optical field intensity in order to achieve good grating coupling coefficient values because they have small refractive index contrast in the grating area).

Employing laterally-coupled ridge-waveguide (LC-RWG) surface gratings for DFB lasers and etched-through-ridge-waveguide (ET-RWG) surface gratings for DBR lasers avoids the problematic over-growth and enables the use of simple epilayer structures. The LC-RWG and ET-RWG surface gratings, illustrated in Fig. 1, are fabricated, without regrowth, on the complete/final epilayer structure, are applicable to different semiconductor materials and can be easily integrated in complex device structures without requiring a difficult epitaxial growth and fabrication process. The surface gratings can achieve a relatively high grating coupling coefficient without being placed in regions with high optical field intensity, due to the fact that they have a high optical contrast in the grating area. They are also placed somehow away from the laser regions with the highest temperature and imply a negligible interaction between the defect-prone processed grating
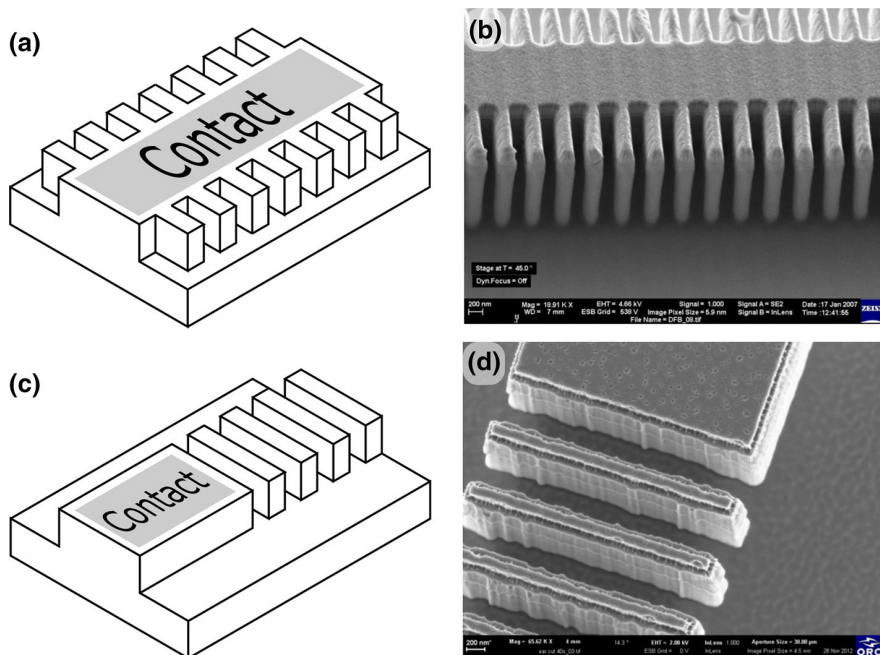
Fig. 1 Sketches (**a**, **c**) and SEM pictures (**b**, **d**) of a laterally-coupled ridge-waveguide DFB grating and of an etched-through-ridge-waveguide DBR grating, respectively

interfaces and the carriers. All these characteristics of LC-RWG and ET-RWG surface gratings lead to more stable devices with better performances and increased reliability.

The STM operation is determined by the transverse modal gain discrimination (Laakso et al. 2008) and by the difference between the grating coupling coefficients of the transverse modes. A high modal gain in ridge waveguide lasers is ensured by having a high under-the-ridge optical confinement factor (i.e. by having a high confinement of the transverse optical field distribution in the electrically pumped areas, which are under the ridge contact). Unfortunately, for LC-RWG (but less for ET-RWG) surface gratings a high under-the-ridge optical confinement factor implies reduced optical confinement factor in the grating areas and, hence, a reduced grating coupling coefficient (κ). Moreover, since the higher-order transverse modes are generally less confined transversely, they have a higher presence in the surface grating areas and thus have a higher grating coupling coefficient than the fundamental mode.

The proposed calculation procedures extend on previous work (Laakso et al. 2008), but neglect effects such as radiating waves, which have an effect on the effective coupling coefficient (Millett et al. 2008). However, simplifying the model enables a fast investigation over a large solution space in search of the range of transverse structure dimensions that lead to the highest modal gain advantage for the fundamental mode while also providing a high enough grating coupling coefficient κ between the forward and backward propagating waves. In other work the effect of grating depth on κ has been considered (Wang et al. 2005), but STM operation is usually neglected and only certain structural parameters are considered.

2 Calculation procedures

2.1 Transverse mode discrimination

The transverse mode gain discrimination is given by the modal gain difference between the fundamental mode and higher-order modes. The magnitude of the modal gain G_m for the mth transverse mode is determined by the convolution of the transverse distribution of the material gain $g(x, y)$ and the transverse optical field intensity distribution of the mth mode $\Psi_m^2(x, y)$ (Mroziewicz et al. 1991):

$$G_m = \frac{\iint \Psi_m^2(x, y) \cdot g(x, y) \, dx \, dy}{\iint \Psi_m^2(x, y) \, dx \, dy}. \tag{1}$$

Good approximate transverse optical field distributions for the guided modes can be obtained with a Mode Solver applied to the longitudinally-averaged transverse distribution of the refractive index. Using longitudinal averaging of the refractive index transverse distribution is based on the continuity conditions at the interfaces between grating slices and on the longitudinal periodicity of the optical field variation, and assumes that the length of the grating period is comparable with the wavelength. The longitudinal averaging is a valid approximation particularly when the perturbation induced by the grating to the effective refractive index of the propagating modes is small, which is generally true for surface gratings, due to the limited confineent of the optical field in the grating area. The weighted average has been used previously both in the transverse plane solutions (Alman et al. 1992) and in the longitudinal direction averaging (Choi et al. 1996; Chen et al. 1996). The longitudinal averaging approximation has been indirectly confirmed by the fitting

between the experimental emission wavelengths and the effective refractive index values calculated using the longitudinal averaging. The longitudinal averaging simplifies the calculations, contributing to faster scanning of a large structural parameter space. In a LC-RWG grating with rectangular lateral corrugations (like in Fig. 2) the longitudinally-averaged transverse refractive index distribution is obtained from the transverse refractive index distributions in the successive wide-ridge and narrow-ridge grating slices:

$$n_{avg}(x, y) = \sqrt{\gamma \cdot n_{wide}^2(x, y) + (1 - \gamma) \cdot n_{narrow}^2(x, y)} \qquad (2)$$

where γ is the grating filling factor ($\gamma = \Lambda_1/\Lambda$ from Fig. 2), n_{avg}, n_{wide} and n_{narrow} are the transverse distributions of the longitudinally-averaged refractive index and of the refractive index in the wide (W + 2D) ridge and narrow (W) ridge grating slices, respectively.

Since the local material gain distribution cannot be evaluated without significant computational effort, we have employed two different approximations for the material gain distribution that enable a fast evaluation of the transverse modal gain discrimination. The first approximation assumes that the local material gain is constant and positive [$g(x, y) = g$] in the pumped active region under-the-ridge and contact and zero elsewhere. This step gain approximation assumes a step lateral distribution of the current in the active region and non-absorbing high-bandgap material outside the pumped area in all regions where the optical field intensity is non-negligible. Under this step gain approximation the modal gain for the mth transverse mode is given by:

$$G_m = g \frac{\iint_{\text{active region, under-the-ridge}} \Psi_m^2(x, y) \, dx \, dy}{\iint_{-\infty}^{+\infty} \Psi_m^2(x, y) \, dx \, dy} = g\Gamma_m^+, \qquad (3)$$

where Γ_m^+ is the under-the-ridge active region confinement factor for the mth transverse mode.

The step gain approximation is suited for deeply etched LC-RWG structures since deep etching close to the active region implies a limited lateral current diffusion. Also, since the absorbing regions outside the pumped area affect the higher order modes more, this approximation is more likely to give a false negative than a false positive STM evaluation. Moreover, the lateral current diffusion can be taken into account by extending the pumped active region area laterally, beyond the region placed strictly under the ridge and contact.

According to the step gain approximation, a stable STM-operation is associated with the maximization of all the ratios of the following type:
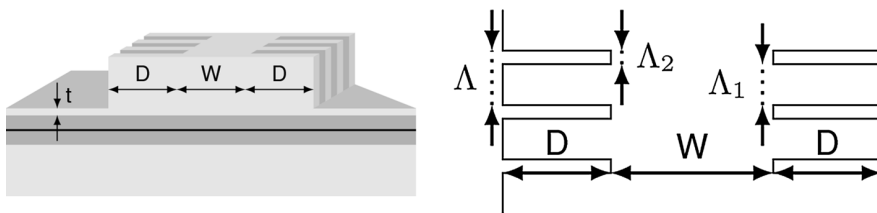

Fig. 2 Schematic 3D and top views of a LC-RWG grating. W ridge width; D flange lateral extension; t remaining un-etched cladding layer thickness; Λ grating period; Λ_1 flange width; Λ_2 trench width

$$\Gamma_{1m}^+ = \frac{g\Gamma_1^+ - g\Gamma_m^+}{g\Gamma_1^+} = \frac{\Gamma_1^+ - \Gamma_m^+}{\Gamma_1^+}. \tag{4}$$

Since Γ_2^+ is generally bigger than Γ_4^+, Γ_6^+, ... and Γ_3^+ is generally bigger than Γ_5^+, Γ_7^+, ..., a good STM-operation figure of merit under the step gain approximation can be derived just from ratios Γ_{12}^+ and Γ_{13}^+:

$$
\begin{aligned}
\Gamma_{123}^+ = \Gamma_{12}^+ \cdot \Gamma_{13}^+ &= \frac{\Gamma_1^+ - \Gamma_2^+}{\Gamma_1^+} \cdot \frac{\Gamma_1^+ - \Gamma_3^+}{\Gamma_1^+} \\
&= \frac{\left(\Gamma_1^+ - \Gamma_2^+\right) \cdot \left(\Gamma_1^+ - \Gamma_3^+\right)}{\left(\Gamma_1^+\right)^2}
\end{aligned}
\tag{5}
$$

Because in many instances the higher-order mode loss is an important factor, a STM operation figure of merit that also takes into account the loss discrimination could be more effective. Such a gain-loss STM figure of merit can be derived from the approximation that the constant gain in the under-the-ridge pumped area of the active region is equal with the constant absorption loss in the un-pumped area of the active region and zero elsewhere. The step gain-loss approximation can be refined by adjusting the switching point between gain and loss regions such that the approximated modal gain fits the modal gain calculated with an accurate method. With this step gain-loss approximation, the modal gain for the mth transverse mode (1) can be simplified to:

$$G_m = g\Gamma_m^\pm = g\Gamma_m^+ - g\Gamma_m^-, \tag{6}$$

where Γ_m^+ and Γ_m^- are the "under-the-ridge" and "not-under-the-ridge" optical confinement factors for the mth transverse mode in the pumped and un-pumped active region areas, respectively.

The modal gain-loss discrimination figure of merit for achieving STM operation is associated with a high gain-loss difference between the fundamental mode and any higher order mode:

$$
\begin{aligned}
G_1 - G_m &= g \cdot \left(\Gamma_1^+ - \Gamma_1^-\right) - g \cdot \left(\Gamma_m^+ - \Gamma_m^-\right) \\
&= g \cdot \left(\Gamma_1^+ - \Gamma_m^+\right) + g \cdot \left(\Gamma_m^- - \Gamma_1^-\right)
\end{aligned}
\tag{7}
$$

Because the fundamental mode is better confined in the active region under-the-ridge while higher order modes have higher confinement in the active region not under-the-ridge, the gain-loss discrimination figure of merit between the fundamental mode and the mth mode can be normalized according to:

$$
\begin{aligned}
\Gamma_{1m}^\pm &= \frac{g\Gamma_1^+ - g\Gamma_m^+}{g\Gamma_1^+} + \frac{g\Gamma_m^- - g\Gamma_1^-}{g\Gamma_m^-} \\
&= \frac{\Gamma_1^+ - \Gamma_m^+}{\Gamma_1^+} + \frac{\Gamma_m^- - \Gamma_1^-}{\Gamma_m^-}.
\end{aligned}
\tag{8}
$$

Moreover, since the second mode is generally better confined in the active region under-the-ridge and less confined in the active regions not under-the-ridge as compared with higher-order even modes, while a similar situation is encountered in the comparison between the third mode and higher-order odd modes, the gain-loss figure of merit for STM operation can be evaluated by studying the normalized product of $\Gamma_{12}^\pm$ and $\Gamma_{13}^\pm$:

$$\Gamma_{123}^{\pm} = \left(\Gamma_{12}^{\pm} \cdot \Gamma_{13}^{\pm} \right) \cdot \frac{1}{4}, \tag{9}$$

where division by 4 is used for normalization because each summand in Eq. (8) has a maximum value of 1 and thus each factor in Eq. (9) has a maximum value of 2. The normalization enables the comparison of the STM gain-loss figures of merit for different structures.

It should be noted that the two modal gain discrimination figures of merit, Γ_{123}^{+} and $\Gamma_{123}^{\pm}$, are not based on accurate calculations of the modal gains but rather on good enough evaluations of the modal gain ratios between the fundamental and higher order modes. The good evaluation of the modal gain ratios is based on the fact that the employed approximations affect all modal gains in a similar way.

2.2 Grating coupling coefficient evaluation

An accurate evaluation of the coupling coefficient (κ) is essential for designing DFB and DBR lasers. Generally the coupling coefficient for the mth transverse mode (κ_m) can be evaluated from the expression (Streifer et al. 1975):

$$\kappa_m = \frac{k_0^2}{2\beta_m} \frac{\iint \Delta\epsilon(x,y) \, \Psi_m(x,y)^2 \, dx \, dy}{\iint \Psi_m(x,y)^2 \, dx \, dy}, \tag{10}$$

where the integration is carried out over the whole (x, y)-plane, Ψ_m is the mth transverse mode optical field distribution for the longitudinally averaged transverse refractive index distribution, and $\Delta\epsilon$ is the perturbation in the dielectric constant. For the oth order rectangular gratings the perturbation term is (Agraval and Dutta 1993):

$$\Delta\epsilon_o(x,y) = \left(n_2(x,y)^2 - n_1(x,y)^2 \right) \cdot \frac{\sin(\pi o \gamma)}{\pi o}, \tag{11}$$

where $n_1(x, y)$ and $n_2(x, y)$ are the transverse refractive index distributions in the longitudinally alternating grating slices. It should be noted that the coupling coefficient formula is based on small-signal analysis, and the longitudinal perturbation of the effective dielectric constant (which is derived from the convolution of $\Delta\epsilon$ with the optical field intensity distribution) should always be much smaller than the average values of the effective dielectric constants in different longitudinal parts of the grating. Combining Eqs. 10 and 11 yields:

$$\kappa_m = \frac{k_0}{2n_{\text{eff,m}}} \frac{\iint \left(n_2(x,y)^2 - n_1(x,y)^2 \right) \Psi_m(x,y)^2 \, dx \, dy}{\iint \Psi_m(x,y)^2 \, dx \, dy} \cdot \frac{\sin(\pi o \gamma)}{\pi o}, \tag{12}$$

where $n_{\text{eff,m}}$ is the effective refractive index corresponding to the mth transverse mode, calculated for the longitudinally averaged transverse refractive index distribution.

Because outside the grating area $n_2(x,y)^2 - n_1(x,y)^2 = 0$ and under the assumption that the refractive index distributions are constant in the grating areas of the grating slices $[n_1(x,y) = n_1$ and $n_2(x,y) = n_2$ in the grating areas], the standard formula for the rectangular grating coupling coefficient results as:

$$\kappa_m = \frac{k_0}{2n_{\text{eff,m}}} \cdot (n_2^2 - n_1^2) \cdot \Gamma_{\text{g,m}} \cdot \frac{\sin(\pi o \gamma)}{\pi o} \tag{13}$$

where o is the grating order and $\Gamma_{\text{g,m}}$ is the optical confinement factor of the mth transverse mode in the grating area.

An approximation which assumes that $n_1 + n_2 \approx 2 \cdot n_{\text{eff,m}}$ is frequently used in combination with the standard formula:

$$\kappa_m \approx \frac{2 \cdot (n_2 - n_1)}{\lambda_0} \cdot \Gamma_{\text{g,m}} \cdot \frac{\sin(\pi o \gamma)}{o}. \tag{14}$$

This approximation is valid for conventional buried gratings, since for them the alternating grating materials are semiconductors with refractive index values close to $n_{\text{eff,m}}$. However, for the surface grating structures this approximation overestimates κ_m, because $n_1 + n_2 < 2 \cdot n_{\text{eff,m}}$ as one of the alternating grating materials is a dielectric with much lower refractive index but a small influence on $n_{\text{eff,m}}$. A better calculation approach for the grating coupling coefficient, which does not assume constant refractive index distributions in the grating areas of the grating slices and is valid for all types of gratings, employs the effective refractive index values for the two successive slices of the grating, $n_{\text{eff,m:2}}$ and $n_{\text{eff,m:1}}$:

$$\begin{aligned} \kappa_m &= \frac{k_0}{2n_{\text{eff,m}}} \left(\frac{\iint n_2(x,y)^2 \Psi_{\text{m}}(x,y)^2 \, dx \, dy}{\iint \Psi_{\text{m}}(x,y)^2 \, dx \, dy} \right. \\ &\left. - \frac{\iint n_1(x,y)^2 \Psi_{\text{m}}(x,y)^2 \, dx \, dy}{\iint \Psi_{\text{m}}(x,y)^2 \, dx \, dy} \right) \cdot \frac{\sin(\pi o \gamma)}{\pi o} \\ &= \frac{k_0}{2n_{\text{eff,m}}} \left(n_{\text{eff,m:2}}^2 - n_{\text{eff,m:1}}^2 \right) \cdot \frac{\sin(\pi o \gamma)}{\pi o}. \end{aligned} \tag{15}$$

The effective refractive index values corresponding to the grating slices ($n_{\text{eff,m:2}}$ and $n_{\text{eff,m:1}}$) cannot be calculated directly with a Mode Solver applied to the refractive distributions of the grating slices because this would imply boundary condition violations in the longitudinal direction. A good approximate effective refractive index calculation procedure for the grating slices is to use the convolution of the transverse optical field distribution [$\Psi_{\text{m}}(x,y)$], obtained for the longitudinally-averaged transverse refractive index distribution, with the transverse refractive index distributions in the grating slices, which leads to:
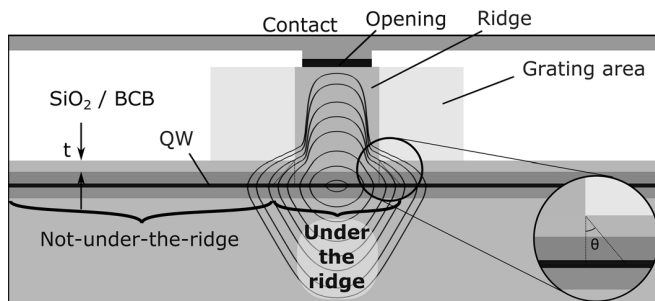
Fig. 3 Schematic cross-section of a LC-RWG grating with a field intensity distribution illustrated with log-spaced contour lines. *QW* quantum well

$$n_{\text{eff,m:slice}}^2 = \frac{\iint \Psi_{\text{m}}^2 \cdot n_{\text{slice}}^2 \, dx \, dy}{\iint \Psi_{\text{m}}^2 \, dx \, dy} - \frac{\iint (\nabla \Psi_{\text{m}})^2 \, dx \, dy}{k_0^2 \cdot \iint \Psi_{\text{m}}^2 \, dx \, dy}. \tag{16}$$

This corresponds also to the derivation of the κ formula from coupled mode theory (Streifer et al. 1975; Dutta and Agrawal 1993) because the second term on the right hand side of Eq. (16) is canceled in the effective refractive index contrast of Eq. (15).

3 Results and discussion

A comparison between the step gain approximation and the improved step gain-loss approximation STM figures of merit can be made by comparing Fig. 4 with Fig. 5, where both figures of merit are plotted as a function of un-etched cladding thickness (t) and ridge width (W) for different supplementary lateral extensions of the "under-the-ridge" gain active area beyond the region strictly under the ridge (as defined by the angle θ of lateral current divergence in the epilayer below the etching depth, shown in the inset of Fig. 3).

The structure for which the calculations have been done is a LC-RWG grating designed for 780 nm operation with D = 2.5 μm. From both Figs. 4 and 5 it can be seen that the supplementary lateral extension of the "under-the-ridge" active area does not influence significantly the figures of merit as long as the extension does not exceed a value corresponding to the epilayer thickness between the grating etching depth level and the active region depth level.
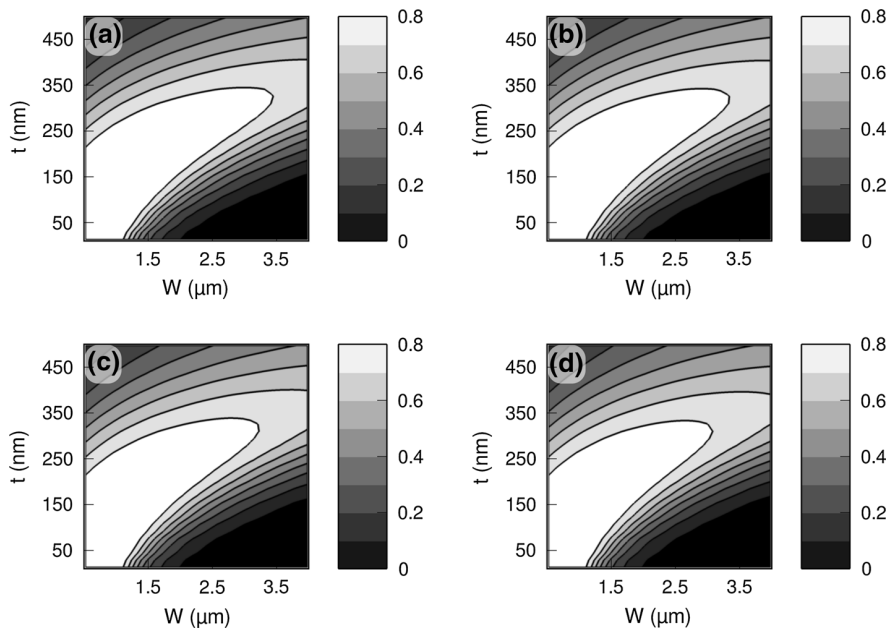
Fig. 4 Variation of the STM figure of merit Γ_{123}^+ as a function of ridge width (W) and un-etched cladding thickness (t) for different lateral current divergence angles below the etching depth level θ: **a** $\theta = 0°$, **b** $\theta = 15°$, **c** $\theta = 30°$, **d** $\theta = 45°$

Fig. 5 Variation of the STM figure of merit $\Gamma_{123}^{\pm}$ as a function of ridge width (W) and un-etched cladding thickness (t) for different lateral current divergence angles below the etching depth level θ: **a** $\theta = 0°$, **b** $\theta = 15°$, **c** $\theta = 30°$, **d** $\theta = 45°$

The comparison between Figs. 4 and 5 shows that the step gain-loss figure of merit gives a narrower range of transverse dimensions for the best STM operation. The parameter combinations that correspond to a good/stable STM operation are the ones that maximize the two figures of merit, but the absolute values of the two different figures of merit, Γ_{123}^{+} and $\Gamma_{123}^{\pm}$, are not directly comparable.

Figure 6 gives the variation of κ as a function of the grating filling factor γ and as a function of the grating trench width for three different grating structures. The buried grating κ changes symmetrically below and above 0.5 filling factor, because the filling factor doesn't change the transverse optical field profile considerably. However, the variation of κ with the filling factor is strongly asymmetrical for the surface gratings. This is due to the fact that a change in the filling factor of the surface gratings induces a significant change in the transverse optical field profile, which affects the confinement factor in the grating area and the effective refractive indexes of the alternating slices. The dependencies of the grating coupling coefficient on the grating trench width, given in right panels of Fig. 6, illustrate that, due to the particular interaction of the surface gratings with the optical field, a high surface grating coupling coefficient is obtained for narrow grating trenches irrespective of the grating order.

The coupling coefficient value dependencies on the un-etched cladding thickness calculated for a 1st-order LC-RWG grating with W = 2.0 μm, D = 2.5 μm and $\gamma = 0.5$, using Eq. (15), using the approximate Eq. (14) and using PICS3D are compared in Fig. 7. The difference between the experimentally confirmed values calculated with Eq. (15) and the values calculated with Eq. (14) are due to the approximation $n_1 + n_2 \approx 2 \cdot n_{eff}$, which leads to an over-estimation of κ by Eq. (14). PICS3D also uses the approximate Eq. (14),
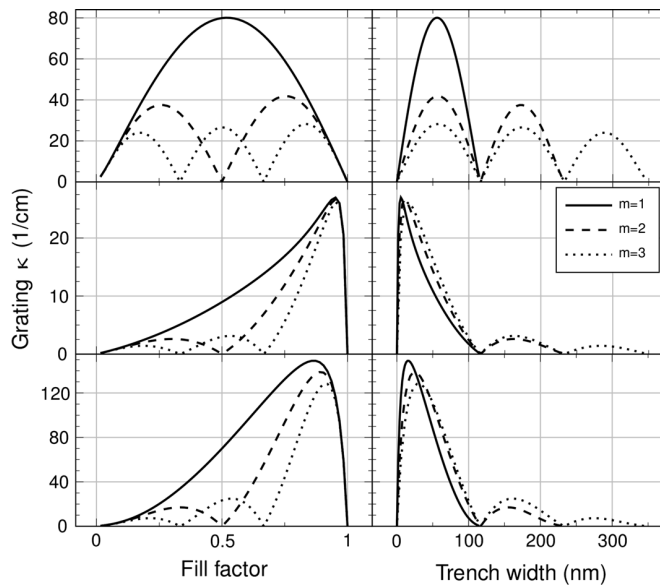
Fig. 6 Comparison of κ variation as a function of grating filling factor (*left panels*) and grating trench width (*right panels*) for three different structures. *Top panels* buried grating; *middle panels* LC-RWG surface grating with W = 2.0 μm, D = 2.5 μm and t = 150 nm; *bottom panels* ET-RWG surface grating with W = 2.0 μm and t = 150 nm. In each *panel* the *solid line* is for a first, the *dashed line* is for a second and the *dotted line* is for a third order grating
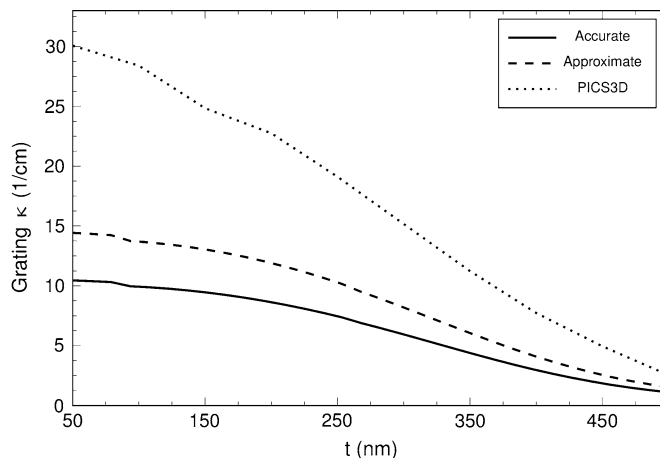

Fig. 7 Comparison of κ variation as a function of un-etched cladding thickness, calculated with different procedures for a 1st-order LC-RWG grating with W = 2.0 μm, D = 2.5 μm and γ = 0.5. The *solid line* has been obtained using Eq. (15), the *dashed line* has been obtained using the approximate Eq. (14), and the *dotted line* has been obtained by using PICS3D (Crosslight Software Inc 2005) (version 2006.11.01)

and the supplementary over-estimation is due to the fact that the values calculated by Eq. (14) are dependent on the very small value of the optical confinement factor in the grating region, which is very sensitive to mesh variations. The calculations performed with

Eq. ([15](#)) do not imply any approximations, are more robust with respect to mesh variations and provide the effective refractive index values for the grating slices, which can be used in longitudinal transfer matrix simulations.

4 Conclusions

Two figures of merit facilitating single transverse mode (STM) operation evaluation based on step gain and on step gain-loss distribution approximations have been introduced. The figures of merit are easy to calculate and enable a fast evaluation of STM operation over a broad range of transverse structural parameters. The figure of merit based on the step gain-loss distribution approximation gives narrower ranges for the transverse structural parameters that lead to STM operation and has been confirmed by numerous experiments with various RWG and LC-RWG structures operating at different wavelengths.

The proposed coupling coefficient calculation does not imply the approximations used in the standard formulas, is applicable to grating structures with variable refractive index across the grating area of the grating slices, is more accurate and more robust to mesh variations, particularly for surface gratings.

References

Agraval, G.P., Dutta, N.K.: Semiconductor Lasers. Springer, New York (1993)

Alman, G.M., Molter, L.A., Shen, H., Dutta, M.: Refractive index approximations from linear perturbation theory for planar MQW waveguides. IEEE J. Quantum Electron. **28**(3), 650–657 (1992)

Chen, C.H., Chen, L.H., Wang, Q.M.: Coupling coefficients of gain-coupled distributed feedback lasers with absorptive grating. Electron. Lett. **32**(14), 1288–1290 (1996)

Choi, W.Y., Chen, J.C., Fonstad, C.G.: Evaluation of coupling coefficients for laterally-coupled distributed feedback lasers. Jpn. J. Appl. Phys. **35**(9R), 4654–4659 (1996)

Crosslight Software Inc: Crosslight Software|PICS3D (2005)

Dutta, N.K., Agrawal, G.: Semiconductor Lasers. Kluwer Academic, Boston (1993)

Laakso, A., Dumitrescu, M., Pietilä, P., Suominen, M., Pessa, M.: Optimization studies of single-transverse-mode 980 nm ridge-waveguide lasers. Opt. Quantum Electron. **40**(11–12), 853–861 (2008)

Millett, R.R., Hinzer, K., Hall, T.J., Schriemer, H.: Simulation analysis of higher order laterally-coupled distributed feedback lasers. IEEE J. Quantum Electron. **44**(12), 1145–1151 (2008)

Mroziewicz, B., Bugajski, M., Nakwaski, W.: Physics of Semiconductor Lasers. Elsevier, Amsterdam (1991)

Streifer, W., Scifres, D.R., Burnham, R.D.: Coupling coefficients for distributed feedback single-and double-heterostructure diode lasers. IEEE J. Quantum Electron. **11**(11), 867–873 (1975)

Wang, J., Tian, J.B., Cai, P.F., Xiong, B., Sun, C.Z., Luo, Y.: 1.55-/spl mu/m algainas-inp laterally coupled distributed feedback laser. IEEE Photonics Technol. Lett. **17**(7), 1372–1374 (2005)

III

ANALYSIS OF THE PHOTON-PHOTON RESONANCE INFLUENCE ON THE DIRECT MODULATION BANDWIDTH OF DUAL-LONGITUDINAL-MODE DISTRIBUTED FEEDBACK LASERS

CrossMark

Analysis of the photon–photon resonance influence on the direct modulation bandwidth of dual-longitudinal-mode distributed feedback lasers

Topi Uusitalo[1] · **Heikki Virtanen**[1] · **Paolo Bardella**[2] · **Mihail Dumitrescu**[1]

Abstract The paper explores the possibilities to extend the direct modulation bandwidth in dual-longitudinal-mode distributed feedback lasers by exploiting the photon–photon resonance induced by the interaction of the two modes in the laser cavity. The effects on the direct amplitude modulation and on the direct modulation of the difference frequency between the two modes are analyzed using simulation and experimental results. When the photon–photon resonance, which occurs at the difference frequency between the two modes, is properly placed at a higher frequency than the carrier-photon resonance, the small-signal amplitude modulation (AM) bandwidth of the laser can be significantly increased. However, both simulations and experiments point out that a high small-signal AM bandwidth does not lead to a high large-signal AM bandwidth if the small-signal modulation response has significant variations across the modulation bandwidth. The paper shows that a high large-signal AM bandwidth is obtained when the two modes are significantly unbalanced, whereas a high-bandwidth difference frequency modulation can be best detected when the two modes are balanced and the DC bias is properly chosen.

Keywords Distributed feedback lasers · Dual-mode lasers · Surface gratings · Nanoimprint lithography · Photon–photon resonance · Amplitude modulation · Difference frequency modulation

1 Introduction

Despite the substantial efforts undertaken to increase the direct modulation bandwidth of lasers, no significant breakthrough has been made when the direct modulation bandwidth has been linked to the carrier-photon resonance (CPR) frequency, largely because the

✉ Topi Uusitalo
topi.uusitalo@tut.fi

[1] ORC, Tampere University of Technology, P.O. Box 692, 33101 Tampere, Finland

[2] Department of Electronics, Politecnico di Torino, Turin, Italy

⦻ Springer

CPR has inherent physical limitations. A higher CPR frequency is obtained by reducing carrier and photon lifetimes but shortening these lifetimes too much ultimately prevents lasing.

However, since the direct modulation bandwidth can be extended considerably by introducing a supplementary high-frequency resonance of the laser, we have analyzed the effects of a high-frequency photon–photon resonance (PPR) on the laser modulation characteristics. The PPR has been obtained by the interaction of two longitudinal modes in dual-mode multi-section distributed feedback (DFB) lasers. The paper analyzes the dynamic behavior of the dual-longitudinal-mode DFB (DLM-DFB) lasers and the effects of mode interaction and photon–photon resonance strength and spectral position on the direct amplitude modulation and on the direct modulation of the difference frequency between the two modes.

The paper is structured as follows: In Sect. 2 the theory behind PPR is introduced alongside descriptions of the simulation methods used. In Sect. 3 both the simulation and measurement results are presented and discussed. Section 4 summarizes the most important findings and draws some conclusions.

2 Photon–photon resonance

Several different device variants have been investigated to exploit the PPR effect (Montrosset and Bardella 2014). One example is a passive feedback DFB, which has extremely narrow operation domains where the dual-mode emission is stable enough to generate a PPR and the corresponding mode-beating signal (Radziunas et al. 2007). However, the authors show that by suppressing the CPR and PPR resonances the direct modulation bandwidth can be increased. Another method is to use a monolithic injection locking (Sung et al. 2003). The authors record a modulation bandwidth increase when the master and slave sections of the laser are locked to each other. Yet another method to generate dual-mode emission that has also been studied is a two-section DFB with independent drive currents and the same or slightly different Bragg frequencies in the two section (Wake 1996). However, this type of laser has not been studied for PPR effects and increased modulation bandwidth.

Our method for generating the PPR is to use a multi-section monolithic DFB laser that exhibits dual-mode emission over a wide operation regime (Dumitrescu et al. 2016). The dual-mode emission is achieved by having $\pi/2$ phase-shifts periodically placed along the grating. When two or more periodically-placed phase-shifts are used, the grating reflectivity exhibits two maxima separated by approximately $2 \times \lambda_{Bragg}/M$, where M is the number of grating periods between phase-shifts. When the two reflectivity maxima are placed at wavelengths around the peak gain wavelength the structure supports two modes placed next to the inner edges of the two reflectivity 'stopbands'. Therefore, the spectral spacing of the emitted modes can be roughly controlled by the number M of the grating periods between two phase-shifts and by the grating coupling coefficient and total grating length (which influence the width of the reflectivity 'stopbands'). Besides being structurally controlled, the mode spacing can be adjusted by the bias applied to the laser sections since carrier-density-induced refractive index changes shift the spectral positions of the reflectivity stopbands.

The exact dual-mode behavior also depends on several other factors besides the grating reflectivity, such as carrier and photon distributions and cavity dynamics, which influence

spatial (Otsuka et al. 1992) and spectral hole burning (Adams et al. 1983), and gain competition between the modes (Adams and Osihski 1982; Lamb 1964).

2.1 Improved rate equation model

When two (quasi-)phase-locked modes coexist in the laser cavity the optical confinement factor is dynamically dependent on the longitudinal position. A modified rate-equation model has been developed to take the PPR into account by treating the longitudinal confinement factor as a dynamic variable (Laakso and Dumitrescu 2011):

$$\frac{d}{dt}\begin{bmatrix} dN \\ dN_p \end{bmatrix} = \begin{bmatrix} -\gamma_{NN} & -\gamma_{NP} \\ \gamma_{PN} & -\gamma_{PP} \end{bmatrix} \begin{bmatrix} dN \\ dN_p \end{bmatrix} + \begin{bmatrix} \dfrac{\eta_i}{qV} dI \\ (N_p v_g g + R'_{sp}) d\Gamma \end{bmatrix}, \tag{1}$$

where γ_{NN}, γ_{NP}, γ_{PN} and γ_{PP} are rate coefficients, as defined in Coldren and Corzine (1995). The modified rate equation model has a supplementary term $(N_p \times v_g \times g + R'_{sp})d\Gamma$, resulted from the (space and) time variation of the dual-mode confinement factor. The amplitude modulation transfer function, including the influence of the extra term, is:

$$H(\omega) = \frac{\eta_i}{qV} \frac{\int_0^T \frac{\gamma_{PN}}{\Delta} dt}{T} + \frac{1}{I_1 \cdot T} \cdot \int_0^T \frac{(\gamma_{NN} + j\omega) \cdot (N_p v_g g + R'_{sp})}{\Delta \cdot e^{j\omega t}} \cdot \frac{d\Gamma}{dt} dt, \tag{2}$$

where T is the time interval for which the phase difference between the two dominant longitudinal modes is maintained. The first term in Eq. (2) resembles the traditional modulation transfer function, with γ_{PN} and Δ taken as time-dependent, while the second term results from considering the (space and) time dependence of the confinement factor. This second term introduces the supplementary PPR peak placed at a frequency equal with the frequency difference between the two dominant longitudinal modes. The model indicates that a primary condition for achieving the PPR is to have the dominant modes phase-locked for long enough (i.e. quasi-phase-locked). Therefore, besides the large frequency difference between modes, the main reason for not achieving significant PPR peaks in the amplitude modulation response of conventional multimode lasers is that they do not provide a mechanism to maintain the phase difference between modes for long enough. It should however be noted that the difficulty in extending the direct laser modulation bandwidth by exploiting the PPR is not so much related to placing the PPR at high frequencies as it is related to achieving a flat modulation response between the CPR and the PPR.

2.2 Travelling-wave model

The dynamic behavior of the laser has been simulated with a finite-difference traveling-wave based method (Bardella and Montrosset 2005). The total electric field in the cavity is expressed as

$$E(z,t) = \left(E^+(z,t)e^{-j\pi z/\Lambda} + E^-(z,t)e^{j\pi z/\Lambda} \right)e^{j2\pi tc/\lambda_B}, \tag{3}$$

where $E^\pm$ are the spatially-dependent slowly-varying forward and backward propagating field envelopes, normalized so that the photon density S is $|E^+|^2 + |E^-|^2$, Λ is the grating pitch and λ_B is the grating Bragg wavelength.

The equations for the propagating fields are coupled to the carrier rate equation, resulting a system of non linear differential equations, which are then discretized in time and space and integrated using the split-step algorithm (Kim et al. 2000):

$$\left(\frac{1}{v_g}\frac{\partial}{\partial t} \pm \frac{\partial}{\partial z}\right)E^{\pm}(z,t) = \delta E^{\pm}(z,t) + \mathrm{j}\kappa E^{\mp}(z,t) + S_{\mathrm{sp}}, \tag{4}$$

$$\frac{\partial}{\partial t}N(z,t) = \frac{\eta_i I}{qV} - \frac{N(z,t)}{\tau} - v_g \frac{\Gamma_{xy}g(z,t)}{1+\varepsilon S(z,t)}S(z,t), \tag{5}$$

with $\delta = \Gamma_{xy}g(z,t) - \alpha_l - \mathrm{j}\pi\left(\frac{2}{\lambda_B}n_{\mathrm{eff}}(z,t) - \frac{1}{\Lambda}\right)$, α_i material losses, κ grating coupling coefficient and S_{sp} spontaneous emission term. A linear dependence of the material gain g and of the refractive index n_{eff} on the carrier density is assumed.

This model is particularly suitable for the considered problem since the nonlinear interactions between the cavity modes (such as the ones generating the PPR) are automatically included in the calculation of $E^{\pm}$.

3 Results

Multi-section 1.3 and 1.55 μm DFB lasers with 3rd order laterally-coupled ridge-waveguide (LC-RWG) surface gratings (Laakso et al. 2008) have been fabricated, without regrowth and using cost-effective UV nanoimprint lithography, from InP-substrate legacy epiwafers (with epilayer structures designed for Fabry-Pérot lasers). Two quasi-phase-locked longitudinal modes with frequency differences ranging from 14 GHz to 1.3 THz have been obtained by adjusting the longitudinal structures of the lasers (mainly by changing the number of periods between phase-shifts). Figure 1a, b show measured and simulated dual-longitudinal-mode emission spectra with mode frequency differences of 47 GHz and 1 THz, respectively. The simulations were done with the commercial PICS3D package from Crosslight Software Inc. The red-shift of the measured spectra with respect to the simulations from Fig. 1 is due to a higher temperature in the measurements than in the simulations. This might be due to more heat generated by a lossy current injection and/ or by inferior heat sinking in the measured devices.

3.1 Amplitude modulation

Because the amplitude modulation (AM) responses of the dual-mode lasers with big frequency differences between the two quasi-phase-locked modes are hampered by the large and deep dips between the CPR and the PPR, we have targeted mainly PPR frequencies below and around 20 GHz.

In order to evaluate the effects of PPR on the laser AM, two types of DFB lasers have been fabricated from the same legacy epiwafer (with the epilayer structure intended for the fabrication of Fabry-Pérot lasers at 1.55 μm) and in the same fabrication run (with similar LC-RWG grating structures). The difference between the two types of DFB lasers was only related to their longitudinal structures: one type had a single $\lambda/4$ phase-shift in the middle of the cavity and a single longitudinal mode emission, whereas the second type had two $\lambda/4$ phase-shifts placed in order to obtain quasi-phase-locked dual-longitudinal-mode emission and a corresponding PPR at 14 GHz.
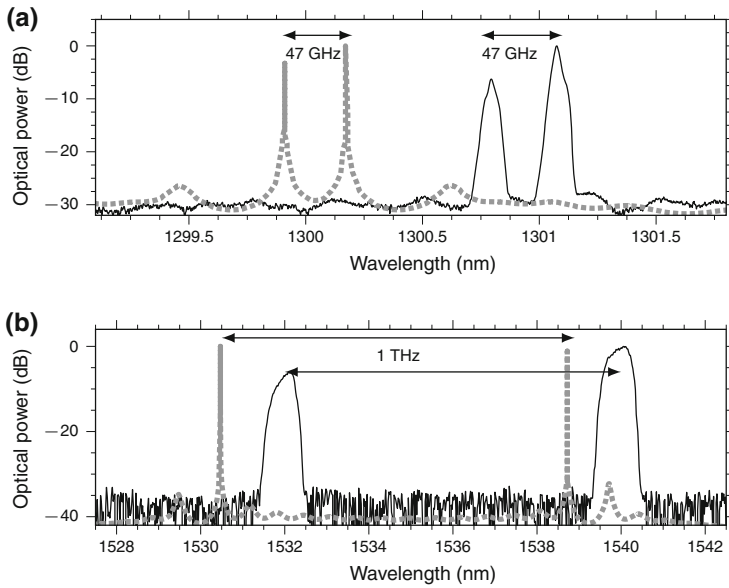
Fig. 1 Simulated (*dotted line*) and measured (*solid line*) dual-mode emission spectra with quasi-phase-locked longitudinal modes having **a** 47 GHz and **b** 1.0 THz frequency spacing

Figure 2 shows measured and simulated direct AM responses for both types of lasers, with and without PPR, illustrating the increase in small-signal AM bandwidth obtained by exploiting the PPR. The AM simulation for the laser with PPR was fitted to the measurement by assuming a side-mode-suppression-ratio (SMSR) of 23 dB between the two quasi-phase-locked modes. The sharper PPR peak in the simulation is due to the fact that noise and averaging are left out in the model.
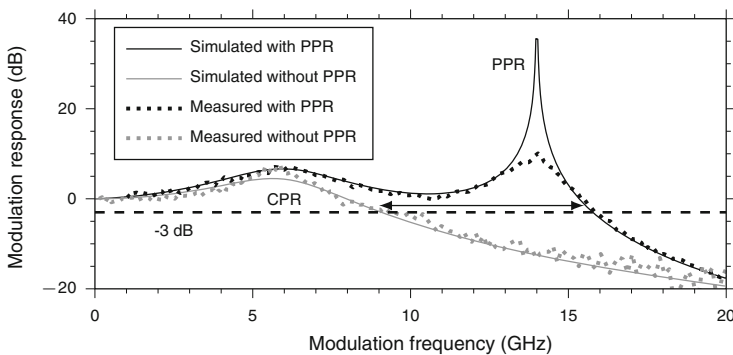
Fig. 2 Measured and simulated small-signal AM responses for two types of DFB lasers fabricated from the same epiwafer in the same fabrication run but with different longitudinal structures. The DFB laser with one $\lambda/4$ phase-shift emits a single-longitudinal mode, whereas the DFB laser with two $\lambda/4$ phase-shifts emits two quasi-phase-locked modes and exhibits a PPR peak at 14 GHz in the small-signal AM response. The attained small-signal AM bandwidth increase, shown with the *arrow*, is more than 5 GHz

Taking into account that the flatness of the small-signal AM response is important in extending the small-signal AM bandwidth, we have studied the possibility to adjust the PPR position and the flatness of the AM response between the CPR and PPR by adjusting the bias currents of the laser sections. Figure 3a illustrates the measured changes in the PPR and CPR frequencies with changing the bias in one sections of a 1.6 mm long multi-section dual-longitudinal-mode DFB (DLM-DFB) laser emitting at 1.55 μm. Because throughout the whole bias variation range the two longitudinal modes are in relatively good balance, the PPR peak dominates CPR and a flat AM response cannot be achieved. Figure 3b shows the measured tuning of the PPR frequency and the CPR changes induced by adjusting one of the bias currents for a 1.5 mm long multi-section DLM-DFB laser emitting at 1.3 μm. Here the CPR-PPR gap is filled when the PPR is brought closer to the CPR. Also the AM response is flatter between the CPR and PPR because the balance between the two longitudinal modes is reduced. The CPR peak changes in Fig. 3a, b because the carrier and photon distributions within the cavity also undergo changes when one of the laser bias currents is adjusted.

Since the −3 dB small-signal AM bandwidth may not be indicative of the large-signal modulation capability, particularly in case of a small-signal AM response with substantial variations across the bandwidth, we have also analyzed the small-signal AM response and the corresponding large-signal modulation capability using a Finite-Difference Travelling-Wave program (Bardella and Montrosset 2012). Figure 4a shows the small-signal AM response simulated for three different phases of the cleaved-facet reflection in a multi-section DLM-DFB laser. A similar effect can be obtained by changing the bias current in
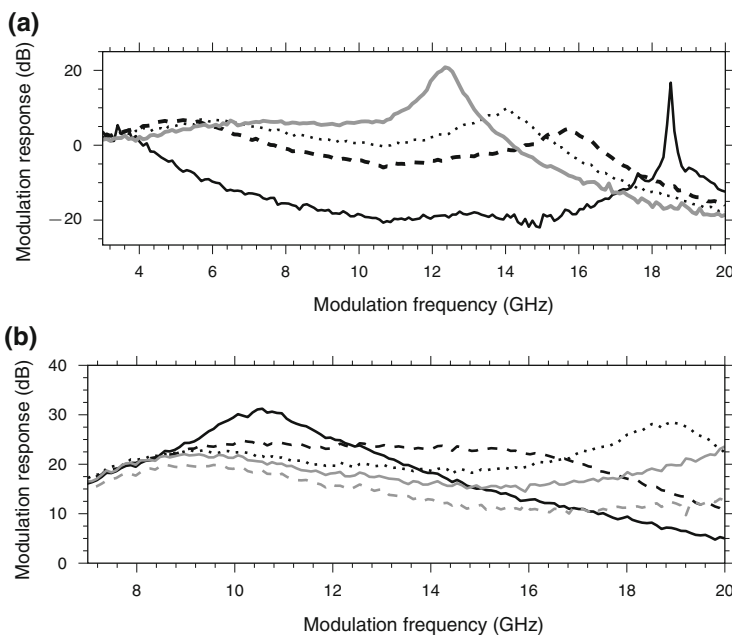
Fig. 3 Measured small-signal AM response for **a** 1.6 mm long multi-section DLM-DFB laser emitting at 1.55 μm and for **b** 1.5 mm long multi-section DLM-DFB laser emitting at 1.3 μm. The current of the section farthest from the lasing facet is increased for modulation responses progressing from *black solid lines* to *dashed lines* to *dotted lines* and to *gray solid lines*

the DLM-DFB laser section farthest from the lasing facet, like in the experiments illustrated in Fig. 3.

Large-signal eye diagrams were calculated for the three small-signal AM cases of Fig. 4a, using a non-return-to-zero pseudorandom bit sequence signal at different modulation bit rates. The cases were chosen to compare the situation when the PPR peak is small, under the −3 dB level and with minimal influence on the small-signal AM bandwidth (case 1, solid line in Fig. 4a); the situation when the PPR peak is moderate and the AM response is extended in a relatively flat way (case 2, dashed line in Fig. 4a); and the situation when the PPR peak is very pronounced (case 3, dotted line in Fig. 4a).

An eye diagram with a reasonably good extinction ratio (ER = 4.5 dB) could be obtained, beyond the −3 dB small-signal AM bandwidth, at 60 Gbit/s for case 2. The simulation for case 3 shows that a strong PPR peak is dramatically reducing the eye opening at 40 Gbit/s, although a good large-signal AM response should be achieved at this rate for a flat small-signal AM response. This result gives the indication that a strong presence of the second mode (i.e a good balance between the two dominant longitudinal modes and a strong PPR) does not bring an increase in the large-signal AM bandwidth.

Interestingly, a good 40 Gbit/s large-signal AM response, beyond the −3 dB small-signal AM bandwidth, could be obtained in the case 1, when the PPR peak is well below the −3 dB level and does not influence significantly the small-signal AM bandwidth. This result is consistent with the rate-equation simulations illustrated in Fig. 2, indicating that the two dominant longitudinal modes should be significantly unbalanced in order to increase the AM bandwidth.
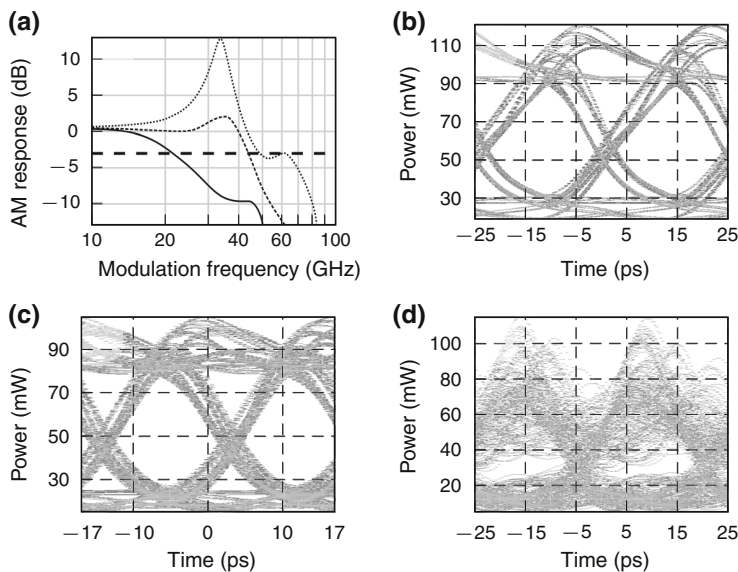
Fig. 4 **a** Simulated small-signal AM response for different phases of the cleaved facet reflection in a multi-section DLM-DFB laser with high-frequency PPR. Case 1: *solid line*, cleaved facet reflection phase $\phi_A = 40°$. Case 2: *dashed line*, $\phi_A = 80°$. Case 3: *dotted line*, $\phi_A = 140°$. **b** 40 Gbit/s eye diagram simulated for case 1, with an extinction ratio (ER) = 6 dB. **c** 60 Gbit/s eye diagram simulated for case 2, with ER = 4.5 dB. **d** 40 Gbit/s eye diagram simulated for case 3

3.2 Difference frequency modulation

Albeit it hampers the extension of the AM bandwidth, a well balanced dual-longitudinal-mode emission could be exploited in frequency-modulated (FM) data transmission schemes by imprinting the signal in the difference frequency between the two dominant longitudinal modes. The tunability of the difference frequency is a prerequisite for difference frequency modulation (DFM). As indicated by the bias-induced frequency shifts of the PPR shown in Fig. 3, the inter-mode difference frequency of the DLM-DFB lasers is tunable over a wide range simply by tuning the bias currents of the laser sections.

Some measurements illustrating the inter-mode difference frequency change with the bias applied to one of the DLM-DFB laser sections are presented in Fig. 5. Only after a large increase in the injected current density the side modes become comparable with the two dominant longitudinal modes (as shown in Fig. 5a) but even then the difference frequency signal can be detected due to the quasi-phase-locking of the two longitudinal modes promoted by the grating structure.

The bias map given in Fig. 5b shows that the change in the difference frequency is smooth and continuous with changing the bias currents in two different sections of the DLM-DFB laser. The stationary difference frequencies in the bias map have been obtained from the photodetected mode-beating signal recorded with an electric spectrum analyzer (ESA). This was done since the frequency resolution achieved with the ESA is at Hertz-level, whereas the available optical spectrum analyzer (OSA) provided only 2 GHz frequency resolution.

The dynamic behavior of the multi-section DLM-DFB lasers was studied in order to evaluate the possibility to exploit the difference frequency modulation in high-speed applications. In a first instance the bias of the first section of the DLM-DFB lasers was modulated with a sinusoidal signal of varying frequencies. The laser output was photodetected with a high bandwidth photodiode (PD) and the photodetected signal was amplified and down-shifted in frequency by mixing it with the signal from a microwave local oscillator (LO) in order to enable the measurement of the generated signal with a high bandwidth oscilloscope. A windowed fast Fourier transform (FFT) with a Gaussian window function (i.e. a Gabor transform) was applied to the time-domain difference frequency signal collected by the oscilloscope.
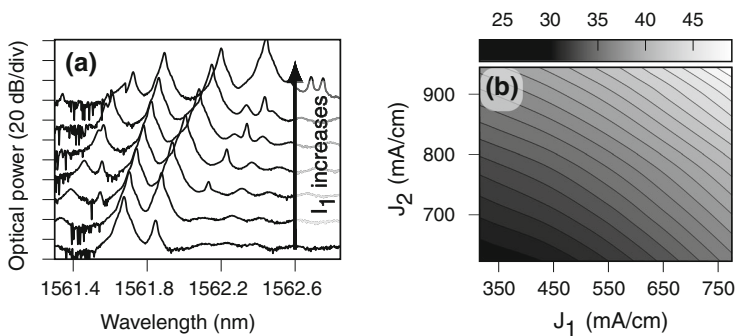

Fig. 5 **a** Dual-longitudinal-mode spectrum variation when the current density J_1 is increased by 653 mA/cm in the DLM-DFB laser section next to the output facet. **b** Difference frequency variation (in GHz) between the two dominant longitudinal modes, measured with an ESA from the photodetected mode-beating signal, as a function of the current densities in the first two DLM-DFB laser sections

Figure 6 shows spectrograms obtained by displaying the time-sequence of the window Fourier transforms for four different sinusoidal laser-bias modulation frequencies f_{mod}: 10, 100, 500 MHz and 1 GHz. The beat signal spectrum variation according to the difference frequency change induced by the sinusoidal modulating signal is clearly visible. Due to the limited oscilloscope bandwidth and sampling frequency (20 GHz, 50 GS/s), the frequency resolution of the spectrograms suffers when the modulation frequency increases since fewer spectral samples can be collected when more time-domain signal variations are recorded per unit time.

The sidebands of the frequency-modulated mode-beating signal spectra shown in Fig. 7 prove that the inter-mode difference frequency can be modulated by sinusoidal signals with frequencies up to 3 GHz. The modulation signal delivery to the DLM-DFB laser is critical at higher frequencies since impedance matching becomes important and the modulation signal strength has to be increased if an impedance-matched delivery circuit is not employed. In the DFM spectra presented in Fig. 7 the modulation signal is increased by 7 dB when the sinusoidal modulation frequency increases from 500 MHz to 1 GHz, and by another 12 dB when the sinusoidal modulation frequency is increased again from 1 to 3 GHz. In fact we have detected sidebands in the DFM spectra up to 10 GHz sinusoidal
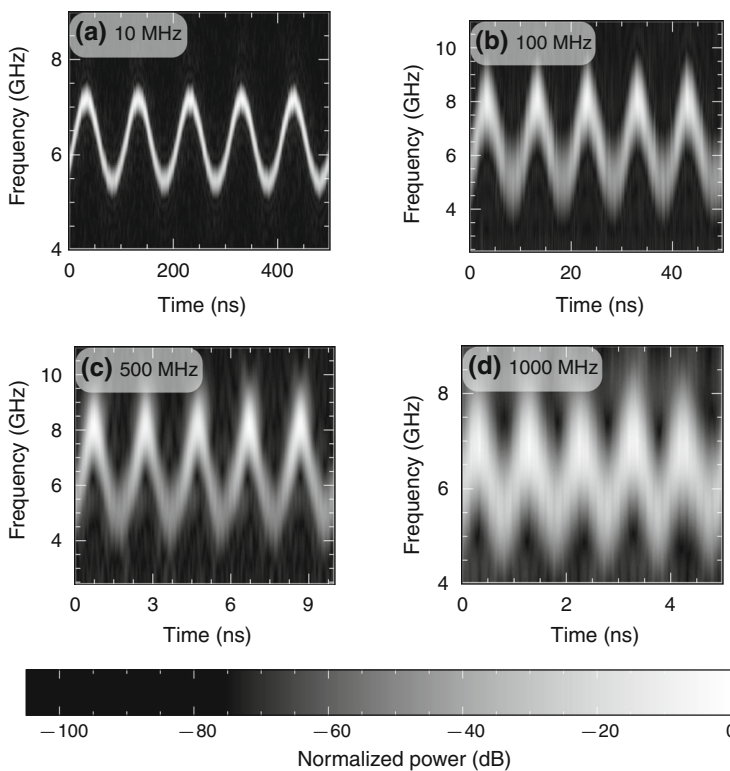
Fig. 6 Spectrograms showing the Gabor transforms of the mode-beat signals obtained from photodetecting the output of the directly modulated DLM-DFB laser. The frequency resolution suffers at higher modulation frequencies because there are less samples in the Fourier transform window due to the limited sampling rate of the oscilloscope
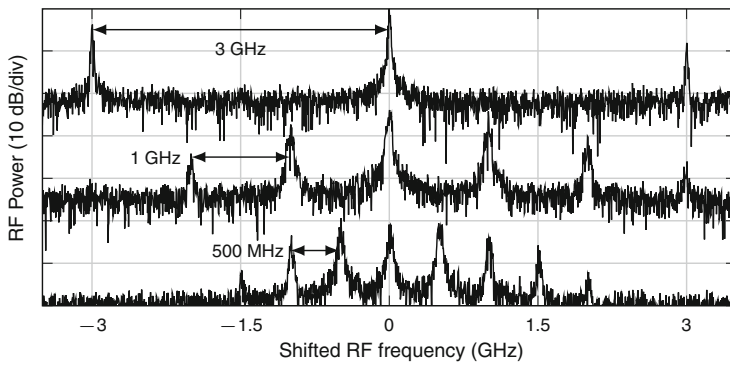
Fig. 7 Spectra of the photodetected mode-beat signal when the bias of one of the DLM-DFB laser sections is sinusoidally modulated at 500 MHz, 1 and 3 GHz. The distance between the FM side bands and the carrier is the same as the sinusoidal modulation frequency

modulation frequencies but they were close to the noise floor due to the poor delivery of the modulation signal to the laser.

Unfortunately, detecting the instantaneous difference frequency change induced by large-signal modulation is difficult. In order to prove that the large-signal difference-frequency modulation can be recovered from the photodetected mode-beating signal we have performed the signal recovery in post-processing. The post-processing procedure is summarized in Fig. 8. First, the photodetected mode-beating signal is frequency down-shifted by mixing with a local oscillator and the resulted FM signal is recorded with a high-speed oscilloscope (shown in Fig. 8a after the application of a Hilbert transform). Then the recorded time-domain signal is transferred to the frequency domain with FFT, and the center frequency of the resulting FM comb is saved. In order to reduce the noise in the signal, a band pass Chebyshev type II infinite impulse response (IIR) filter was used (because it has a relatively good slope at the pass band edges and it doesn't have ripples in the pass band) (Fig. 8b). The filtered time-domain signal is then Hilbert transformed in order to get the amplitude variation of the difference frequency signal as well as its instantaneous frequency (Boashash 1992) (Fig. 8c).

The signals extracted by post-processing can be used to generate eye diagrams, like the ones presented in Fig. 9. It should be noted that, due to the frequency down-shifting by mixing with the local oscillator, the extracted difference frequency is flipped in frequency (i.e. large difference frequencies are extracted as small mode-beat signal frequencies and vice-versa).

The comparison of the extracted AM and FM eye diagrams indicate that a parasitic AM accompanies the DFM, somehow similarly as a parasitic FM (i.e. chirp) accompanies the amplitude modulation of single-mode lasers.

The large-signal modulation results have been simulated in steady-state frequency domain with a transfer matrix method (TMM) program. In this approach the effect of the bias modulation has been modeled as carrier-density-induced refractive index changes. The transfer matrix model only considers the steady-state optical properties of the laser, and other effects, particularly dynamic effects, are omitted. The TMM-calculated bias-induced steady-state difference frequency changes corresponding to the post-process-extracted 1 GHz eye diagrams are given in Fig. 10. The difference frequencies obtained by the post-processing of the measured signal and the TMM-simulated difference frequencies differ in
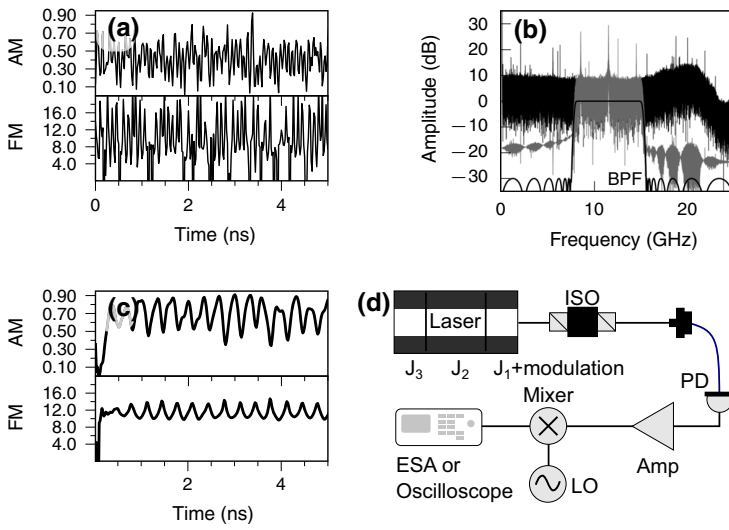
Fig. 8 Illustration of the post-processing procedure for difference frequency demodulation: **a** Hilbert transforms of the signal recorded after photodetection and mixing, showing the envelope (AM) and the instantaneous frequency (FM); **b** FFT of the signal with and without IIR filtering; **c** Hilbert transform of the IIR filtered signal; **d** the measurement setup employed for collecting the signals for post-processing (*ISO* optical isolator, *PD* photodiode, *Amp* RF amplifier, *LO* local oscillator)
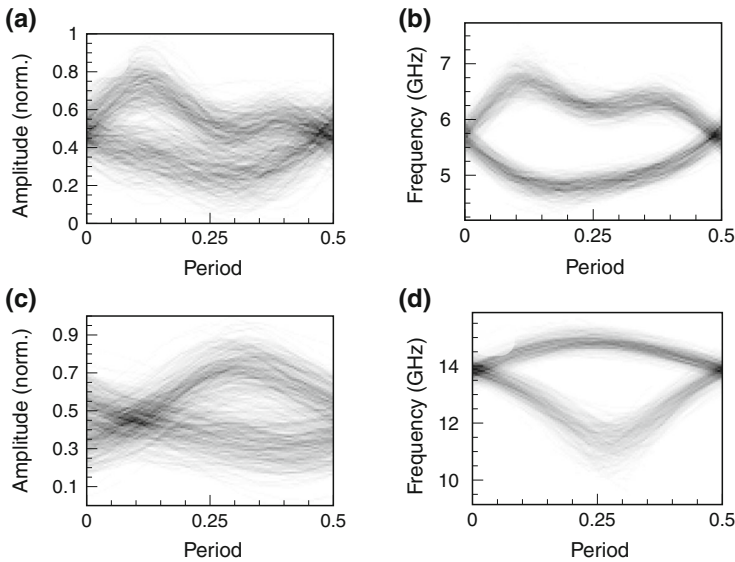
Fig. 9 Eye diagrams of the post-process-extracted difference frequency signal resulted from directly modulating the first section of the laser with a 1 GHz (**a**, **b**) and with a 3 GHz (**c**, **d**) signal. **a** and **c** Give the extracted amplitude modulation, whereas **b** and **d** Give the difference frequency modulation
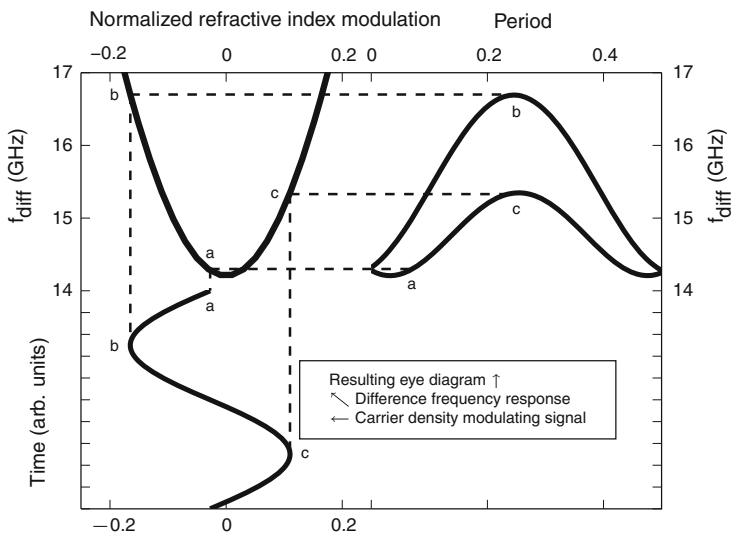
Fig. 10 TMM simulation of the 1 GHz difference frequency eye diagram of Fig. 9b obtained by post-processing
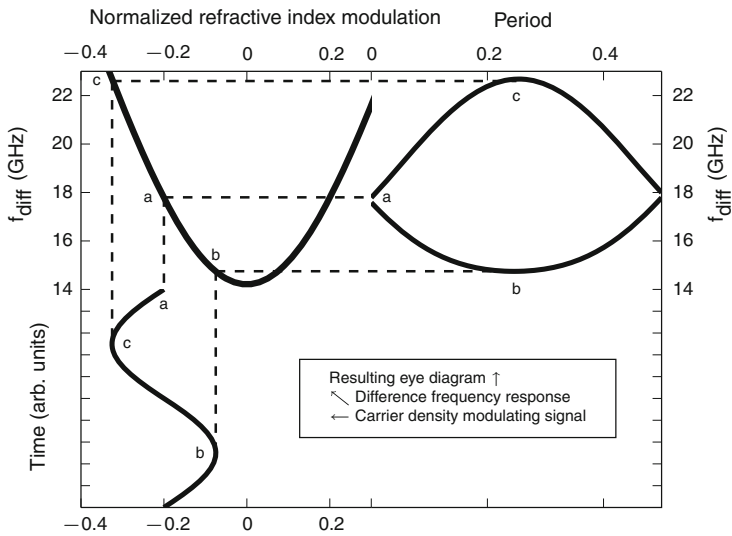
Fig. 11 TMM simulation of the 3 GHz difference frequency eye diagram of Fig. 9d obtained by post-processing

their absolute values for multiple reasons: because the measured values have been down-shifted in frequency, because the coupling coefficients might be different between simulation and measurement, and because the simulation doesn't take into account electrical and dynamic effects.

Despite its limited accuracy, the TMM results indicate that the main cause for the 1 GHz eye diagram asymmetry is the DC point where the bias modulation is applied. The TMM simulations of the large-signal modulation at 3 GHz (shown in Fig. 11) indicate that the superior eye diagram symmetry and the large eye diagram opening resulted from post-processing and shown in Fig. 9d are mainly induced by a better DC bias point.

4 Conclusions

The presented simulation and experimental results show that quasi-phase-locked dual-longitudinal-mode emission and the associated photon–photon resonance can be exploited for increasing the direct amplitude modulation (AM) bandwidth beyond the limitations set by the carrier-photon resonance. The extension of the AM bandwidth is obtained when the photon–photon resonance frequency is placed relatively close to the carrier-photon resonance frequency and one of the two grating-favored longitudinal modes is significantly weaker than the other one.

The presented simulation and experimental results also show that direct modulation of the difference frequency between the dominant modes of dual-longitudinal-mode (DLM) DFB lasers can be exploited for high-bandwidth frequency-modulation (FM) data transfer. The difference frequency modulation (DFM) analysis leads to several conclusions: (1) significant continuous difference frequency changes can be obtained by changing the bias in one of the DLM-DFB laser sections; (2) a good dual-longitudinal-mode balance favors difference frequency detection; (3) the difference frequency can be modulated with very high rates; (4) the DC bias point at which the modulation is applied has a significant influence on the possibility to transmit and extract accurately the signal imprinted in the difference frequency. Overall, the dual-longitudinal-mode difference frequency experiments and simulations indicate that the DFM can be effectively employed in high-bandwidth FM optical transmission if practical real-time demodulation schemes are developed.

References

Adams, M., Osihski, M.: Longitudinal mode competition in semiconductor lasers: rate equations revisited. IEE Proc. I-Solid-State Electron Dev. **129**(6), 271–274 (1982)

Adams, M., et al.: Influence of spectral hole-burning on quaternary laser transients. Electron. Lett. **16**(19), 627–628 (1983)

Bardella, P., Montrosset, I.: Analysis of self-pulsating three-section DBR lasers. IEEE J. Sel. Top. Quantum Electron. **11**(2), 361–366 (2005). doi:10.1109/JSTQE.2005.845608

Bardella, P., Montrosset, I.: Design and simulation of DBR lasers with extended modulation bandwidth exploiting photon–photon resonance effect. In: European Conference on Integrated Optics (ECIO'2012) Sitges, Spain (2012)

Boashash, B.: Estimating and interpreting the instantaneous frequency of a signal. I. fundamentals. Proc. IEEE **80**(4), 520–538 (1992)

Coldren, L., Corzine, S.: DIode Lasers and Photonic Integrated Circuits. Wiley, New York (1995)

Dumitrescu, M., Uusitalo, T., Virtanen, H.: Laser structure. Patent Cooperation Treaty application PCT/EP2016/064476 (2016)

Kim, B., Chung, Y., Lee, J.: An efficient split-step time-domain dynamic modeling of DFB/DBR laser diodes. IEEE J. Quantum Electron. **36**(7), 787–794 (2000). doi:10.1109/3.848349

Laakso, A., Dumitrescu, M.: Modified rate equation model including the photon–photon resonance. Opt. Quantum Electron. **42**(11–13), 785–791 (2011)

Laakso, A., Dumitrescu, M., Viheriälä, J., Karinen, J., Suominen, M., Pessa, M.: Optical modeling of laterally-corrugated ridge-waveguide gratings. Opt. Quantum Electron. **40**(11–12), 907–920 (2008)

Lamb Jr., W.E.: Theory of an optical maser. Phys. Rev. **134**(6A), A1429–A1450 (1964)

Montrosset, I., Bardella, P.: Laser dynamics providing enhanced-modulation bandwidth. In: Proceedings of SPIE–The International Society for Optical Engineering, vol. 9134 (2014)

Otsuka, K., Georgiou, M., Mandel, P.: Intensity fluctuations in multimode lasers with spatial hole burning. Jpn. J. Appl. Phys. **31**(9A Pt 2), L1250–L1252 (1992)

Radziunas, M., Glitzky, A., Bandelow, U., Wolfrum, M., Troppenz, U., Kreissl, J., Rehbein, W.: Improving the modulation bandwidth in semiconductor lasers by passive feedback. IEEE J. Sel. Top. Quantum Electron. **13**(1), 136–142 (2007)

Sung, H.K., Jung, T., Wu, M.C., Tishinin, D., Tanbun-Ek, T., Liou, K., Tsang, W.: Modulation bandwidth enhancement and nonlinear distortion suppression in directly modulated monolithic injection-locked DFB lasers. In: Proceedings of the International Topical Meeting on Microwave Photonics, 2003 (MWP 2003), pp 27–30. IEEE (2003)

Wake, D.: Optical devices for millimetre-wave transmission. In: 1996 International Topical Meeting on Microwave Photonics, 1996 (MWP'96), pp 145–148 (1996). Technical Digest. doi:10.1109/MWP.1996.662091

IV

DUAL-MODE DFB LASER DIODES WITH APODIZED SURFACE GRATINGS

by

Uusitalo, T., Virtanen, H., Viheriälä, J. & Dumitrescu, M. 2018

Dual-mode DFB laser diodes with apodized surface gratings

Topi Uusitalo,[1,*] Heikki Virtanen,[1] Jukka Viheriälä,[1] and Mihail Dumitrescu[1]

[1]*Tampere University of Technology, Optoelectronics Research Centre, Korkeakoulunkatu 3, 33720, Finland*
[*]*topi.uusitalo@tut.fi*

Abstract: Dual longitudinal mode distributed feedback lasers have been fabricated using surface gratings with and without apodization. Analytic formulas and simulations that have been used to derive design guidelines are presented. The fabricated device characteristics are in good agreement with the simulations. The grating apodization enables a lower threshold current density, a higher output power and a broader range of difference frequency tunability by bias, which can be extended beyond the measured 15–55 GHz by changing the device structure. The apodization and the complex coupling of the surface gratings reduce the effects of the uncontrollable phase of facet reflections, enabling the use of higher facet reflectivities, which leads to narrower intrinsic short time-scale linewidths.

OCIS codes: (140.3490) Lasers, distributed feedback; (140.3600) Lasers, tunable; (220.4241) Nanostructure fabrication.

References and links

1. X. Q. Qi and J. M. Liu, "Photonic microwave applications of the dynamics of semiconductor lasers," IEEE J. Sel. Top. Quantum Electron. **17**, 1198–1211 (2011).
2. B. Lin, B. Pan, Z. Zheng, M. Li, and S. C. Tjin, *A review of photonic microwave generation* (IEEE, 2016), p. 1–3.
3. R. Waterhouse and D. Novack, "Realizing 5G: Microwave photonics for 5G mobile wireless systems," IEEE Microw. Mag. **16**, 84–92 (2015).
4. A. Corradi, G. Carpintero, B. W. Tilma, M. K. Smit, and E. A. J. M. Bente, *Integrated dual-wavelength semiconductor laser systems for millimeter wave generation* (IEEE, 2012), p. 34–35.
5. Y. Yang, Y. Wang, L. Wang, S. Zhang, and J. J. He, *Single-mode narrow linewidth three-section coupled-cavity laser* (IEEE, 2012), p. 515–516.
6. F. v. Dijk, A. Accard, A. Enard, O. Drisse, D. Make, and F. Lelarge, *Monolithic dual wavelength DFB lasers for narrow linewidth heterodyne beat-note generation* (IEEE, 2011), p. 73–76.
7. L. Yu, D. Lu, Y. Sun, and L. Zhao, "Tunable photonic microwave generation by directly modulating a dual-wavelength amplified feedback laser," Opt. Commun. **345**, 57–61 (2015).
8. S.-C. Chan and J.-M. Liu, "Tunable narrow-linewidth photonic microwave generation using semiconductor laser dynamics," IEEE J. Sel. Top. Quantum Electron. **10**, 1025–1032 (2004).
9. J. Zheng, N. Song, Y. Zhang, Y. Shi, S. Tang, L. Li, R. Guo, and X. Chen, "An equivalent-asymmetric coupling coefficient DFB laser with high output efficiency and stable single longitudinal mode operation," IEEE Photonics J. **6**, 1–9 (2014).
10. J. Fricke, J. Decker, A. Maaßdorf, H. Wenzel, G. Erbert, A. Knigge, and P. Crump, "DFB lasers with apodized surface gratings for wavelength stabilization and high efficiency," Semicond. Sci. Technol. **32**, 075012 (2017).
11. Y. Shi, S. Li, R. Guo, R. Liu, Y. Zhou, and X. Chen, "A novel concavely apodized DFB semiconductor laser using common holographic exposure," Opt. Express **21**, 16022–16028 (2013).
12. T. Uusitalo, H. Virtanen, and M. Dumitrescu, "Transverse structure optimization of distributed feedback and distributed bragg reflector lasers with surface gratings," Opt. Quantum Electron. **49**, 206 (2017).
13. R. Millett, K. Hinzer, A. Benhsaien, T. J. Hall, and H. Schriemer, "The impact of laterally coupled grating microstructure on effective coupling coefficients," Nanotechnology. **21**, 134015 (2010).
14. K. David, G. Morthier, P. Vankwikelberge, R. G. Baets, T. Wolf, and B. Borchert, "Gain-coupled DFB lasers versus index-coupled and phase shifted DFB lasers: a comparison based on spatial hole burning corrected yield," IEEE J. Quantum Electron. **27**, 1714–1723 (1991).
15. M. Dumitrescu, T. Uusitalo, H. Virtanen, J. Viheriälä, and A. Laakso, "Semiconductor laser structure with a grating and multiple phase shifts therein," (2017). PCT Patent Application WO/2017/220144.
16. T. Uusitalo, H. Virtanen, M. Karjalainen, S. Ranta, J. Viheriälä, and M. Dumitrescu, "Distributed feedback lasers with alternating laterally coupled ridge-waveguide surface gratings," Opt. Lett. **42**, 3141–3144 (2017).

17. M. J. Strain and M. Sorel, "Integrated III–V bragg gratings for arbitrary control over chirp and coupling coefficient," IEEE Photonics Technol. Lett. **20**, 1863–1865 (2008).
18. P. S. J. Russell, J.-L. Archambault, and L. Reekie, "Fibre gratings," Phys. World **6**, 41–46 (1993).
19. H. Virtanen, T. Uusitalo, and M. Dumitrescu, "Simulation studies of DFB laser longitudinal structures for narrow linewidth emission," Opt. Quantum Electron. **49**, 160 (2017).
20. L. A. Coldren, S. W. Corzine, and M. L. Mashanovitch, *Diode lasers and photonic integrated circuits*, vol. 218 (John Wiley & Sons, 2012).
21. H. Wenzel, G. Erbert, and P. M. Enders, "Improved theory of the refractive-index change in quantum-well lasers," IEEE J. Sel. Top. Quantum Electron. **5**, 637–642 (1999).

1. Introduction

Stable, efficient and low cost photonic generation of high frequency RF signals has been under intense research [1, 2]. The photonic solutions for the next generation wireless systems require spectral purity, low latency, low cost, power efficiency, and scalability [3]. Dual-wavelength semiconductor lasers have been investigated for millimeter wave generation [4], but they suffer from large intrinsic phase noise [2]. Coupled-cavity structures [5], Y-branch lasers [6], monolithically integrated amplified feedback lasers with direct modulation [7], and varying feedback conditions [8] have been used to decrease the linewidth, but they are more complex to fabricate and control and are less efficient. Apodization has been used for making the output power extraction from facets asymmetric without the need for asymmetric facet coatings [9] and for increasing the efficiency of broad-area distributed feedback (DFB) lasers [10]. The apodization has also been used for reducing the spatial hole burning [11], but it is difficult to implement in the fabrication of semiconductor laser buried gratings.

Surface gratings eliminate the re-growth, simplifying the fabrication process, and can achieve a relatively high coupling coefficient without being placed in areas with high optical field intensity, because they have a high optical contrast in the grating region [12]. Being placed away from the areas with the highest temperature and optical field intensity and involving a negligible interaction between the defect-prone processed interfaces and the carriers, the surface gratings lead to more stable devices with better performances and increased reliability. Also, the gain coupling associated with surface gratings [13] increases the stability of the grating modes with respect to laser cavity facet feedback [14]. Supplementary, the apodization can easily be implemented for surface gratings [15].

The paper presents dual-longitudinal-mode distributed feedback (DM-DFB) lasers with periodic phase-shifts, gives guidelines for varying the difference frequency between the emitted modes, and discusses surface grating implementation including apodization and its effects. Linear apodization in DM-DFB lasers leads to reduced threshold current and a broader and more sensitive tunability of the difference frequency by bias variation. The apodization also enables balancing the output modes in bias configurations that give higher output power at the facet with the weaker grating strength.

2. Device structure and fabrication

The epilayer structure used in the fabrication of the DM-DFB lasers has four 7 nm $In_{0.689}Al_{0.055}Ga_{0.256}As$ quantum wells interleaved with $In_{0.456}Al_{0.174}Ga_{0.37}As$ barriers, embedded between 80 nm $In_{0.521}Al_{0.373}Ga_{0.106}As$ waveguide layers, and $In_{0.52}Al_{0.48}As$ barrier reduction layers between the waveguide layers and InP claddings. Cladding doping was increased, starting from waveguide layers, between 1×10^{17} and 1.5×10^{18} cm^{-3} on the p-side and between 8×10^{17} and 8×10^{18} cm^{-3} on the n-side. The effective index was solved by a finite differences mode solver [12].

The laterally-coupled ridge-waveguide (LC-RWG) surface gratings, illustrated in Fig. 1, have been processed using UV nanoimprint lithography [16]. The apodization, which can be easily achieved with any longitudinal profile by varying the ridge width (W) and/or the lateral extension
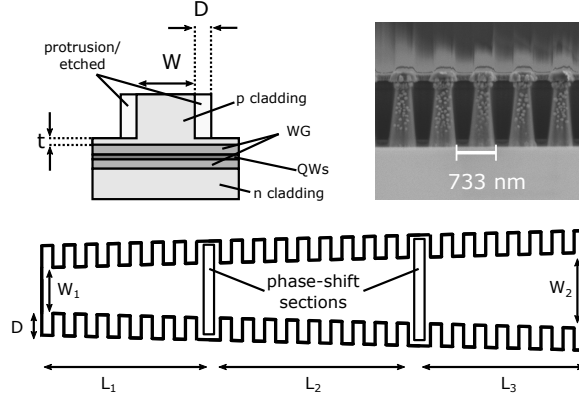
Fig. 1. Schematics of the transverse and longitudinal structure of the studied lasers. The scanning electron micrograph is from the side of the grating. W: ridge width (W_1=W_2 for un-apodized gratings); D: lateral extension of the protrusions; WG: waveguide; QW: quantum well; t: un-etched cladding thickness; L_i: length of ith section.

of the protrusions (D) along the device, was accomplished by linearly changing W between 1.4 and 2.0 μm along the longitudinal direction, while keeping D constant at 2.5 μm. The values for grating etching depth, ridge width (W) and lateral extension of the protrusions (D) have been chosen so that they ensure a stable single transverse mode operation [12]. Supplementary, the D value has been chosen such that it leads to a coupling coefficient close to the maximum achievable for the ridge width range, while having a minimal influence on the local effective refractive index [17] and on the target etching profile of the LC-RWG gratings. This is possible since the optical field decreases rapidly in the grating area away from the ridge, which, for the given structure, leads to a saturation in the increase of the coupling coefficient and of the local effective refractive index with increasing D beyond 2.5 μm. The change in W also induces a change in the local effective refractive index of the grating, corresponding to a calculated 0.6 nm Bragg resonance chirp between the wide-W and the narrow-W ends of the grating. Because the longitudinal structure of the laser has three sections with different contacts, the chirp effects can be controlled by asymmetrically biasing the three sections of the laser.

The dual-mode emission is derived from the superposition of two different gratings, which, in the simplified case of sinusoidal effective refractive index variation, is given by $n(x) = n_0 + \Delta n \cdot \sin a + \Delta n \cdot \sin b$, where a and b are related to the Bragg resonance frequencies ν_{1B} and ν_{2B} as $a = \frac{2\pi \cdot x}{\Lambda_1} = \frac{4\pi}{m \cdot c} \cdot \nu_{1B} \cdot n_{\text{eff}\_1}$ and $b = \frac{2\pi \cdot x}{\Lambda_2} = \frac{4\pi}{m \cdot c} \cdot \nu_{2B} \cdot n_{\text{eff}\_2}$, with Λ_i the periods, n_{eff_i} the effective refractive indexes and m the grating order of the two gratings. Under the assumption that $n_{\text{eff}\_0} = n_{\text{eff}\_1} \approx n_{\text{eff}\_2}$, which is a good approximation for gratings with the same profile, contrast, and filling factor, the resulting superposition $n(x) = n_0 + 2\Delta n \cdot \sin\left(\frac{a+b}{2}\right) \cdot \cos\left(\frac{a-b}{2}\right)$ corresponds to a grating with a period $\Lambda_{0B} = m \cdot \frac{c}{2 \cdot n_{\text{eff}\_0} \cdot (\nu_{1B} + \nu_{2B})/2} = m \cdot \frac{c}{2 \cdot n_{\text{eff}\_0} \cdot \nu_{0B}}$ modulated with a period $\Lambda_M = m \cdot \frac{c}{2 \cdot n_{\text{eff}\_0}(\nu_{2B} - \nu_{1B})/2} = m \cdot \frac{c}{2 \cdot n_{\text{eff}\_0} \cdot \nu_M}$. If a 1st-order modulation is implemented (in order to have the shortest modulation period) by introducing a corresponding phase shift after every M periods of the grating, i.e. $\Lambda_M = 2 \cdot M \cdot \Lambda_{0B}$, (which for gratings having a rectangular profile of the effective index variation and a 0.5 filling factor, corresponds to introducing $\lambda_{0B}/4$ phase-shifts

after every M periods), then two stopbands are created with their Bragg resonances spaced by:

$$\Delta \nu_{\text{Bragg}} = \nu_{0\text{B}}/(m \cdot M) \tag{1}$$

which, in the case of closely spaced Bragg resonances corresponds to $\Delta \lambda_{\text{Bragg}} \approx \lambda_{0\text{B}}/(m \cdot M)$. When the two stopbands are placed around the peak gain wavelength, the modulated grating supports two modes placed close to the reflectivity nodes next to the inner (i.e. between the stopbands) edges of the stopbands. In such a case, a good approximation for the frequency difference between the two emitted modes is obtained by subtracting the stopband frequency width between the encompassing nodes (which is approximately the same for the two stopbands) from the difference between the two Bragg resonance frequencies:

$$\Delta \nu_{\text{modes}} \approx \Delta \nu_{\text{Bragg}} - \Delta \nu_{sb} \approx \nu_{0\text{B}} \cdot \left[\frac{1}{m \cdot M} - S \cdot \sqrt{\left(\frac{2 \cdot \Delta n}{2 \cdot n_{\text{eff\_0}}} \right)^2 + \left(\frac{1}{M \cdot (P+1)} \right)^2} \right] \tag{2}$$

where $\Delta \nu_{sb}$ is the approximate frequency difference between the first reflectivity nodes encompassing the stopband, adapted from [18]; S is a factor related to the grating strength, which was fitted as $S \approx 1.8/m \cdot (1 - 0.1 \cdot \kappa \cdot L)$ for the studied structures; $2 \cdot \Delta n$ is the (effective) refractive index difference between two longitudinal grating slices; $n_{\text{eff\_0}}$ is the longitudinally averaged effective refractive index; and P is the number of discrete phase shifts. The carrier grating order m is included in the formula when the modulation is of 1$^{\text{st}}$-order. κ is the grating coupling coefficient and L the total grating length. The approximation works well when the grating filling factor is not close to the values leading to minima in the coupling coefficient variation with filling factor [12] and when $\kappa \cdot L$ is relatively high, both conditions being required for grating-induced mode selection. It should be noted that the lasing modes' frequencies can differ slightly from the frequencies of the inner nodes next to the reflectivity stopbands, depending on the complete resonance condition for the cavity.

A rectangular-step effective refractive index variation (e.g. with $n_{high} = 3.1977$ and $n_{low} = 3.1966$ in the alternating slices of the un-apodized gratings) was calculated for the studied gratings, and lasers having modulated gratings with varying M, κ, and P have been simulated. Lasers with two phase-shifts (P=2) separating three sections of M=818 3$^{\text{rd}}$-order grating periods ($\Lambda_{0\text{B}}$ =733 nm) (resulting in a total length L≈1.8 mm) with linearly-apodized and with un-apodized gratings have been fabricated and characterized. The structural parameters of the fabricated devices have been chosen to achieve difference frequencies measurable with the bandwidth of the available photodetectors as well as to have a $\kappa \cdot L$ product in the range of 1.5, in order to avoid spatial hole burning and the associated modal instability. The fabricated devices have three independent contacts over the three grating sections separated by the phase shifts. The measured difference frequencies included the 26–28 GHz range for bias combinations that compensated the uncontrollable phase of the facet reflections, in good agreement with the analytic approximation of Eq. (2) (which gives a difference frequency of 27.17 GHz for $S \approx 0.5$) and with the numeric simulations (giving 27.3 GHz), both of which do not take into account the effects of facet reflections. The measured difference frequency between the emitted modes is tunable (in a range up to 15–55 GHz for the lasers with apodized gratings, which are less sensitive to facet reflection phase variation) by changing the bias of these three sections.

2.1 Simulation

The variation of the real part of κ and of the effective refractive index with the width of the ridge (W), calculated as described in [12], are shown in Fig. 2.

Transfer matrix method (TMM) and time-domain traveling wave (TDTW) [19] simulations were used for the design of the apodized structures. TMM was used to determine the effects of
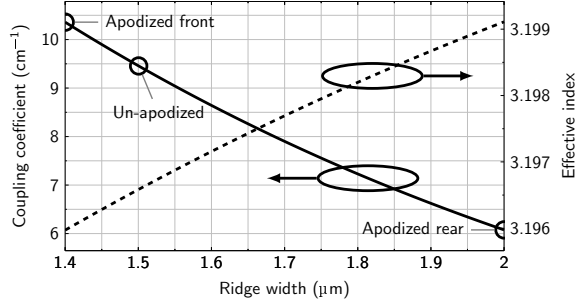
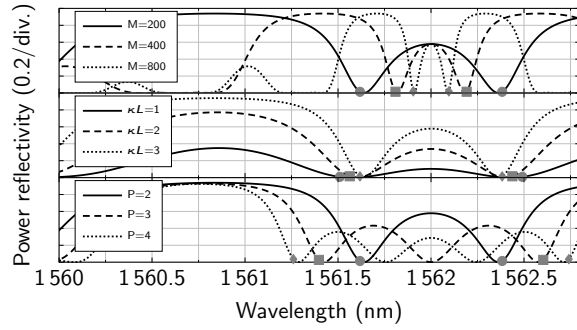Fig. 2. Calculated dependencies of the coupling coefficient and effective refractive index on the ridge width (W).

Fig. 3. Dual-stopband grating reflectivity for different values of M (top panel), κ (middle panel), and P (bottom panel). Mode positions on the stop band edges are illustrated with gray symbols. $\lambda_{\mathrm{Bragg}} = 1562\,\mathrm{nm}$, $\kappa = 20\,\mathrm{cm}^{-1}$, $P = 2$, and $M = 400$ (with corresponding $L \approx 0.88\,\mathrm{mm}$) when not varied.

different structural variations on the stop bands, mode positions and mirror losses, while TDTW was used to determine the time-dependent longitudinal photon and carrier densities initiated by spontaneous emission noise sources under different bias conditions. The effects of variations in M, κ, and P on the stop band and mode positions simulated with TMM are shown in Fig. 3. The top panel shows that the mode spacing reduces significantly with increasing M. It also indicates that the mode selection is weaker when the grating has a small number of sections (P+1) with a relatively small number of grating periods (M) and a low coupling coefficient (κ), leading to a small $\kappa \cdot L$. This can be mitigated by increasing the number of grating sections. The middle panel of Fig. 3 reveals that the variation of κ has a much smaller effect on mode spacing than the variation of M; while the bottom panel shows that mode spacing increases and $P - 1$ reflectivity lobes appear between the two stopbands with increasing P.

Figure 4 shows the calculated dependencies of the difference frequency between the emitted modes ($\Delta\nu_{\mathrm{modes}}$) on structural parameter variations. The top-left panel of Fig. 4 shows the variation of $\Delta\nu_{\mathrm{modes}}$ with κ and M when the 3$^{\mathrm{rd}}$-order grating has three equal sections (i.e. for

$P + 1 = 3$). Constant $\kappa \cdot L$ lines have been overlaid on top of the $\Delta\nu_{\text{modes}}$ variation map. The panel shows that $d\Delta\nu_{\text{modes}}/d\kappa$ decreases for higher M, which indicates that structures with a higher number of periods are more tolerant to etching profile variations. The horizontal solid lines from the top-right panel of Fig. 4, corresponding to Eq. (1) calculated at 1562 nm for $m = 3$ and different values of M, point out that larger frequency differences, entailing a smaller M value, would require an increased number of sections ($P + 1$) in order to achieve a reasonably high $\kappa \cdot L$ when κ is relatively low. The top-right panel of Fig. 4 also shows the simulated values of the difference frequency and of the side-mode suppression ratio (SMSR) for $m = 3$, $M = 150$ and different values of P, indicating that, by increasing the number of phase sections while keeping M constant, the difference frequency can be smoothly increased with only a moderate penalty to the SMSR. The circles showing simulated difference frequency values coincide well with the line calculated using the analytic approximation of Eq. (2). The bottom-left panel of Fig. 4 shows the effects of changing M in the end sections (between facets and the outermost phase shifts), while keeping $M = 150$ constant for the inner sections of the grating, illustrating the effect of the variable position of cleaving planes. The upper lines show the variation of the difference frequency for different values of P, while the lower lines show that for $P > 2$ the SMSR is reduced when the number of periods in the end sections is substantially reduced or increased with respect to the number of periods in the inner grating sections. The bottom-right panel of Fig. 4 shows the variation of $\Delta\nu_{\text{modes}}$ with the number of periods (M) in the grating sections for different P. The values obtained with the analytic approximation coincide with TMM numerical simulation results, validating Eq. (2).

Grating structures with two phase shifts were chosen for the experiments since they are the shortest that can achieve a given $\Delta\nu_{\text{modes}}$ with the best SMSR. A high SMSR is helpful when a high speed photodetector is employed for detecting the mode-beating difference frequency. The difference frequency tuning by bias variations is modeled in TMM by changing the effective indexes of the three sections independent of each other, with the magnitude of change derived from carrier density variations [21]. An example of carrier and photon density distributions along the laser cavity, simulated by the TDTW method, is shown in Fig. 5. The distributions have been plotted for the nonuniform bias conditions which lead to balanced powers of the two emitted modes from the output facet at 0 cavity position. The apodization can be used to direct the emission toward the lower κ end of the device at 0 cavity position, as illustrated in Fig. 5. Besides this, other goals of employing apodization, with respect to the dual-mode emission, were to decrease the mode-beating RF spectrum linewidth and to increase the sensitivity and range of difference frequency tuning by bias.

The DM-DFB lasers with apodized gratings were characterized before and after applying AlO_x anti-reflection (AR) coating with atomic layer deposition. The reflectivity achieved with single layer AR coating is between 2 and 3 %.

3. Device performance

The DM-DFB lasers were biased with three DC drivers, two Thorlabs ITC510s and one Thorlabs LDC340. The output beam was collimated and coupled to a single mode fiber after a Thorlabs IO-2.5-1550-VLP free space Faraday isolator. The spectrum of the fiber-coupled light was recorded with an optical spectrum analyzer (OSA). For the mode-beating linewidth measurements the light was transmitted to a Finisar XPDV2320R broadband photodiode, whose output was amplified with a Centellax UA0L65VM RF amplifier before being measured with a 26.5 GHz electrical spectrum analyzer (ESA).

The light-current (LI) characteristics of the three-contact lasers with apodized and un-apodized gratings were obtained by shining the collimated beam into an integrating sphere with an InGaAs photodiode. Both devices were similarly biased, using the three independent drivers to achieve uniform currents through all sections. The measured LI characteristics, given in Fig. 6, show that
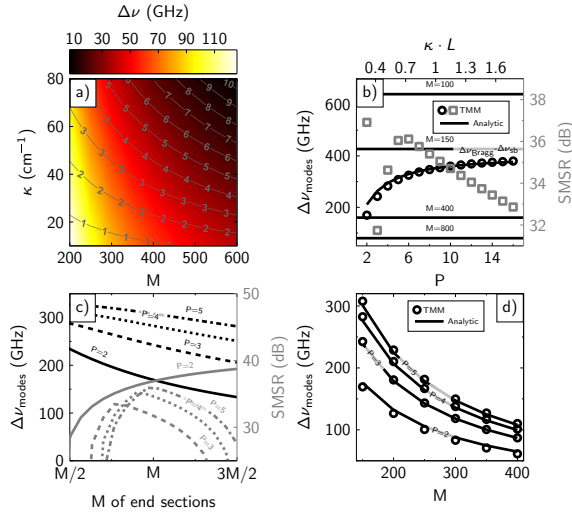
Fig. 4. Variations of the difference frequency ($\Delta\nu_{modes}$) for a 3rd order grating with a period of 733 nm: a) with the coupling coefficient (κ) and with the number of grating periods between phase shifts (M), for structures with three grating sections ($P + 1 = 3$); b) with the number of grating sections ($P + 1$), for $\kappa \approx 9.5\,cm^{-1}$ (corresponding to the value evaluated for the fabricated un-apodized devices) and $M = 150$; c) with the number of grating periods in the end sections, for $\kappa \approx 9.5\,cm^{-1}$ and M=150 in the inner grating sections; d) with M, for $\kappa \approx 9.5\,cm^{-1}$ and different P values. The corresponding side mode suppression ratio (SMSR) variations included in panels b and c have been evaluated from calculated mirror losses [20].
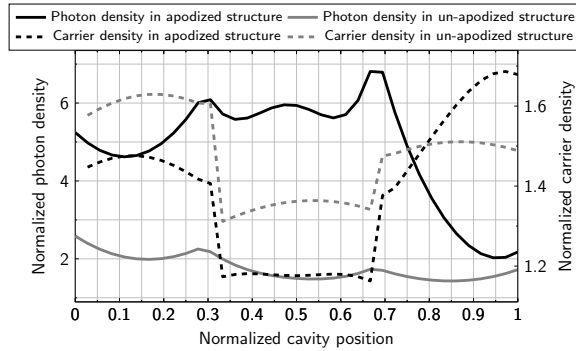
Fig. 5. TDTW simulation of the longitudinal distributions of the photon and carrier densities for lasers with apodized and un-apodized gratings when the powers of the two emitted modes at the output facet are in balance. The output facet is at 0 cavity position, next to the low κ side of the apodization.

the apodized DM-DFB lasers have a lower threshold current and a higher maximum power than the un-apodized DM-DFB lasers.
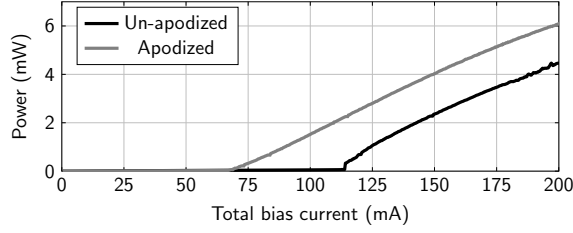

Fig. 6. Light-current characteristics of the DM-DFB lasers with apodized and un-apodized gratings. Both devices are AR coated.

3.1 Optical domain

Figure 7 shows measured optical spectra from an AR-coated un-apodized DM-DFB laser and from apodized DM-DFB lasers with cleaved facet and with AR-coated facets. The spectra, which have been overlaid in frequency for easier comparison, show that the apodization does not induce detrimental effects on the spectral characteristics, and that the AR coating suppresses the Fabry-Pérot modes well. The narrow side-modes present next to the main two modes before and after AR coating are attributed to four-wave mixing.
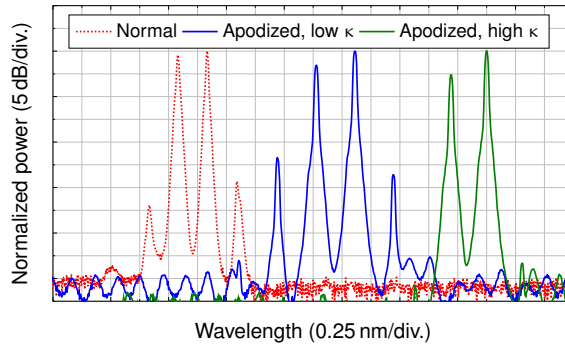

Fig. 7. Optical spectra of DM-DFB lasers with apodized and un-apodized gratings. The spectra have been shifted to make them overlap.

The measured difference frequency variations with grating sections' bias levels for the un-apodized and apodized DM-DFB lasers are shown in Fig. 8. The apodized structure shows a larger bias-dependent difference frequency variation, with a maximum range from 15 to 55 GHz while the difference frequency in the un-apodized lasers varies between 25 and 44 GHz. It should be noted that the range of difference frequency variation with bias depends on structural adjustments (e.g. varying M, P, n_{eff}, κ). The difference frequency derivative with respect to the front section bias current is also higher for the apodized structure although the average ridge width (1.5 µm)

and the current density variation are the same in the front sections of both structures. While the complex coupling coefficient of LC-RWG surface gratings enables grating-defined behavior with relatively high facet reflectivities irrespective of facet reflection phases [14], AR facet coating is still beneficial for achieving stable dual-mode operation with DM-DFB lasers under a broader range of variable bias. For the DM-DFB laser with apodized gratings the AR coating extends the range of balanced dual-mode operation, increases the difference frequency tuning range and reduces the influence of the middle section bias.
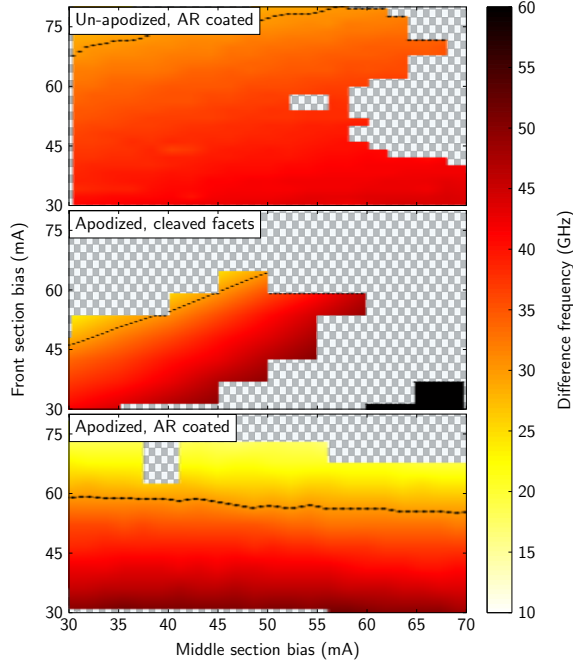

Fig. 8. Difference frequency as a function of front and middle section bias currents for DM-DFB lasers with un-apodized gratings and AR-coated facets and for DM-DFB lasers with apodized gratings and either as-cleaved or AR-coated facets. The difference frequency variation has been determined from optical spectra. The dotted lines indicate 30 GHz difference frequency level. Gray tiled areas correspond to the situations when the two strongest modes are not next to the inner nodes of the grating reflectivity stopbands.

3.2 RF domain

The mode-beat RF spectra from un-apodized and apodized DM-DFB lasers, measured around the mode separation frequency, are shown in Fig. 9. The measured lineshapes have been fitted in the least squares sense with unconstrained pseudo-Voigt line shapes, in which the widths of the Gaussian and Lorentzian components are not fixed. This has been done since the Gaussian linewidth induced by technical noise during the beat signal spectrum acquisition time varies and is much larger than the Lorentzian linewidth. The technical noise was mainly produced by thermal fluctuations and by fluctuations in the drive currents of the three independent sources. In

contrast to typical heterodyne linewidth measurement setup, where the beat signal frequency is derived using a stable RF oscillator, in our measurement scenario the frequencies of both modes vary, contributing to the beat signal width and shape. This is the main reason why the conventional Voigt profile does not fit well to the measured RF spectra.

A longer photon lifetime inside the laser cavity induces linewidth narrowing. The AR-coated un-apodized structure has a larger overall κL product and thus has a narrower linewidth than the AR-coated apodized device, because a higher κL leads to a longer photon lifetime in the cavity. However, a high κL has certain drawbacks, since it also leads to spatial hole burning, which affects the range and stability of grating-based operation [19]. The apodized structure has a lower overall κL product, but the complex-coupled apodized surface gratings allow higher facet reflectivities without affecting the dual-mode operation significantly. Thus the DM-DFB lasers with apodized LC-RWG gratings achieve a dual-mode operation range that is both broader and more sensitive to bias changes, and a narrower linewidth when higher reflectivity facets are employed to increase the photon lifetime in the laser cavity, as shown in Fig. 9.
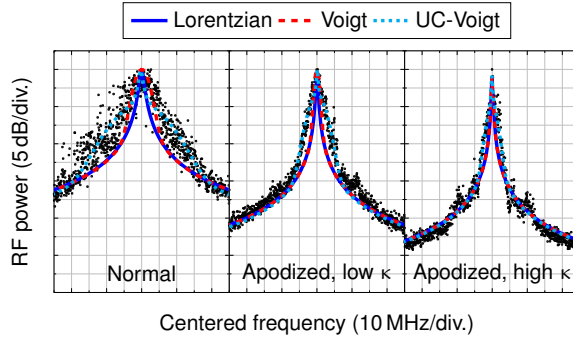

Fig. 9. Measured beat-mode RF spectra and unconstrained pseudo-Voigt fits for DM-DFB lasers having un-apodized gratings and AR-coated facets and for DM-DFB lasers having apodized gratings and as-cleaved or AR-coated facets. The radio and video bandwidth of the ESA was = 10 kHz.

In Fig. 10 the full-width-at-half-maximum (FWHM) of the Lorentzian component of the unconstrained pseudo-Voigt fit is shown as a function of integration time per bandwidth, for DM-DFB lasers with un-apodized gratings and AR-coated facets and for DM-DFB lasers with apodized gratings and as-cleaved facets. Figure 10 shows that the DM-DFB laser with apodized gratings has a narrower intrinsic Lorentzian linewidth and a smaller linewidth variance on the short time scale. The Lorentzian linewidth broadening with increasing integration times (1.82×10^{12} Hz^2 s^{-1} and 2.95×10^{12} Hz^2 s^{-1} for lasers with un-apodized and with apodized gratings, respectively) are derived from increased noise contribution to the power spectral density as the integration time increases. The higher slope in the linewidth broadening with increasing integration time for the lasers with apodized gratings is related to the higher sensitivity of the emitted mode frequencies and of the difference frequency to the fluctuations in the cavity, which are induced by spontaneous-emission events as well as by thermal and current variations. The difference frequency jitter contributes to the linewidth broadening with longer integration times, but it is not significantly influencing the linewidth for short integration times. The smaller linewidth variance indicates better dual-mode operation stability under random variations at those short integration times. These observations imply that if the difference frequency were

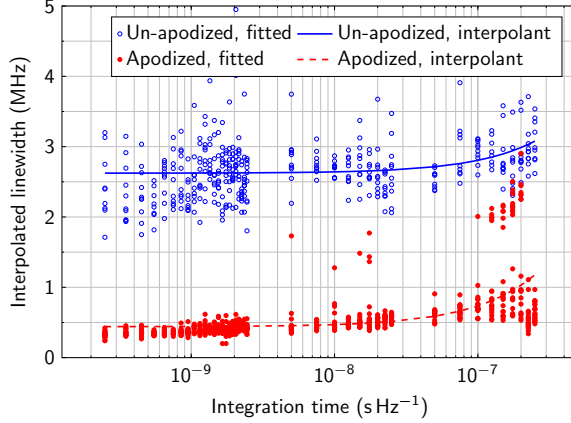locked, the long term linewidth would also stay in the range observed for short integration times.

Fig. 10. FWHM of the Lorentzian linewidth component from the unconstrained pseudo-Voigt fit as a function of integration time for the DM-DFB lasers with un-apodized gratings and AR-coated facets and for the DM-DFB lasers with apodized gratings and as-cleaved facets. The ESA bandwidth was set to 100 kHz to enable shorter integration times.

4. Conclusions

The theory and guidelines for designing dual-mode DFB lasers with LC-RWG surface gratings have been outlined. The surface gratings have been studied since they enable re-growth free fabrication and easy implementation of grating apodizations with arbitrary profiles. The effects of structural parameter variations on the difference frequency between the emitted modes have been analyzed and an analytic approximation formula for the difference frequency dependence on the main structural parameters was derived. The effects of linear grating apodization have been analyzed in simulation studies and have been experimentally investigated. DM-DFB lasers with linearly apodized LC-RWG surface gratings have a lower threshold current density and a higher maximum output power. They also have a more stable dual-mode operation, an increased sensitivity of the difference frequency on bias currents and a broader difference frequency tuning range by bias variations. The measured bias-controlled difference frequency tuning range was increased from 25–44 GHz for DM-DFB lasers with un-apodized LC-RWG gratings to 15–55 GHz by linear apodization of the gratings. The apodized surface gratings have reduced the influence of the un-controllable phase of the facet reflections, enabling the use of higher facet reflectivities, which, combined with the grating reflectivity, increase the photon lifetime in the cavity, narrowing the intrinsic Lorentzian linewidth of the emitted modes.

The improved characteristics of DM-DFB lasers with apodized gratings can be exploited for the generation of high-frequency RF signals in different frequency bands by using a reduced number of laser types (with tunable difference frequency) and a reduced number of photonic RF transceiver components. The exploitation of tunable DM-DFB lasers can thus reduce the complexity, footprint, power consumption, and cost of photonic RF transceivers as well as reduce the required laser inventory.

Acknowledgments